Early effects of neoadjuvant chemotherapy in breast cancer using metabolic MRI

Erwin Krikken

Early effects of neoadjuvant chemotherapy in breast cancer using metabolic MRI
PhD Thesis, Utrecht University, the Netherlands

Early effects of neoadjuvant chemotherapy in breast cancer using metabolic MRI

Vroegtijdige effecten van neoadjuvante chemotherapie in borstkanker gemeten met metabole MRI

(met een samenvatting het Nederlands)

Proefschrift

ter verkrijging van de graad van doctor aan de Universiteit Utrecht op gezag van de rector magnificus, prof.dr. H.R.B.M. Kummeling, ingevolge het besluit van het college voor promoties in het openbaar te verdedigen op woensdag 29 mei 2019 des middags te 4.15 uur

door

Erwin Krikken

geboren op 4 juli 1989 te Hardenberg

Contents

General introduction

1

General introduction

Breast cancer

Breast cancer is the most common cancer among women worldwide and is the second cause of cancer death in women. Approximately one in seven women in the Netherlands will develop breast cancer (1). Breast cancers can originate from different parts of the breast. Most breast cancers start in the ducts (ductal cancers). Some start in the glands that produce breast milk (lobular cancers). There are also other types of breast cancer that are less common.
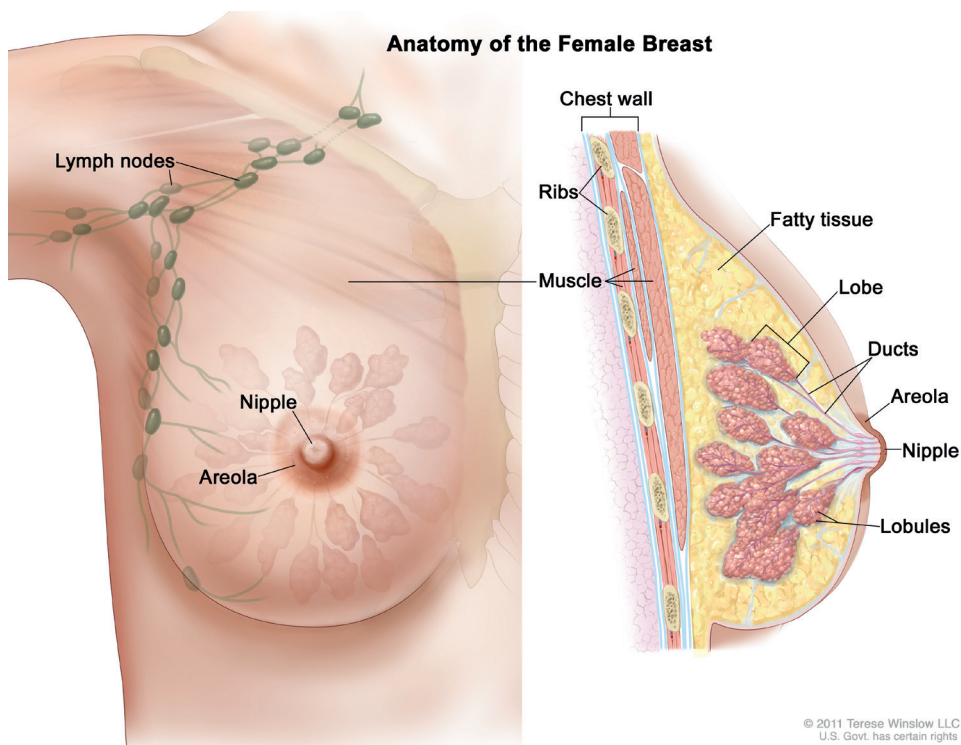
Figure 1 Anatomy of the female breast. The nipple and areola are shown on the outside of the right breast (figure on the left). The lymph nodes, lobes, lobules, ducts, and other parts of the inside of the breast are on the right.

Breast cancer can spread when the cancer cells get into the bloodstream or lymphatic system and are carried to other parts of the body. The lymphatic system is a network of lymphatic vessels that connects lymph nodes. In the case of breast cancer, cancer cells can enter those lymph vessels and could start to grow inside lymph nodes. From the

1

lymph nodes, breast cancer can metastasize to any location in the body but it primarily metastasizes to the bone, lungs, liver and brain (2). Staging of breast cancer helps to determine the optimal treatment plan for a patient and staging used to be based on the TNM system (tumor, nodes, metastasis):

- Tumor: size of the tumor and whether it is has grown into nearby areas.
- Nodes: whether the cancer is in the lymph nodes.
- Metastasis: whether the cancer has spread to distant organs in the body beyond the breast.

However, since 2018 the American Join Committee on Cancer (AJCC) added the following characteristics to the guidelines (3):

- Estrogen receptor (ER) and progesterone receptor (PR) status: whether these hormone receptors are present in the tumor.
- Human epidermal growth factor receptor 2 (Her2) status: whether the tumor produces too much Her2 protein.
- Tumor grade: measurement of how much the tumor cells differ from normal cells.

Staging of breast cancers ranges from stage 0 (carcinoma in situ) up till stage IV, were a higher number means that the tumor has spread more throughout the body (increased tumor load). Staging of breast cancer is used to predict the prognosis of the patient and to determine the most suitable treatment for the individual patient.

Treatment for breast cancer

In recent years, there has been a rapid development of live-saving treatments for breast cancer, which are continuously improving. The primary objective of therapy is always to clear as much of cancer cells from the body as possible and to prevent recurrence of the cancer. In clinical practice, a multidisciplinary team of clinicians will determine the optimal treatment plan for the individual patient based on the subtype of the tumor including hormonal status, the stage of the tumor, genomic markers, age, general health, menopausal status and the presence of known oncogenes for breast cancer. The most common treatments are (breast conserving) surgery, radiation therapy, chemotherapy, hormone therapy and targeted therapy, yet in many cases, the treatment plan will consist of a combination of these treatments. The research in this thesis however, focuses on treatment effects of chemotherapy, in particular neoadjuvant chemotherapy.

Neoadjuvant chemotherapy

Neoadjuvant chemotherapy (NAC) is increasingly used for pre-surgical treatment with the main purpose of downsizing locally advanced tumors to make them (better) suitable for surgical resection (4). Locally advanced tumors have one or more of the following features:

- Large size (> 5 cm)
- Spread to several lymph nodes in the axilla
- Spread to other tissues such as the skin, muscle or ribs.

The recent St. Gallen consensus (5) favors a preference for NAC treatment in HER2+ subtypes and triple negative breast cancer, stage II and III. This preference is extended to women who are eligible for breast conserving surgery at diagnosis.

Chemotherapy drugs target cells that grow and divide rapidly, such as cancer cells. However, some normal cells also divide quickly, like cells in hair follicles, nails, the mouth, digestive tract, and bone marrow. Chemotherapy will unintentionally affect these fast-growing healthy cells, causing chemotherapy side effects. Most chemotherapy regimens are anthracycline- and taxane-based therapies. Anthracyclines damage DNA of cancer cells and interfere with their reproduction (6). Taxanes are a class of anticancer agents that bind to and stabilize microtubules causing cell-cycle arrest and apoptosis (7).

For HER2+ breast tumors, neoadjuvant therapy usually includes a combination of the targeted therapy drugs trastuzumab and pertuzumab (5). In general, chemotherapy treatment consists of multiple repeating cycles. The total length of the therapy depends on the type of cancer, the extent of cancer and the type of drugs that are given but it usually lasts between 3-6 months, although it can be more or less than that.

A downside of NAC treatment is that the desired tumor size reduction is not accomplished in up to 31% of patients who will have stable or even progressive disease (8). The problem is identifying those patients before the start of treatment, as these patients experience the side effects of NAC treatment without any benefit for their treatment. In order to predict which patients will have stable or progressive disease, it is important to find biomarkers that can early assess the response to NAC in the individual patient. This could enable the adjustment of systemic therapy during course and avoid unnecessary toxicity and related costs of ineffective treatment.

Currently, the effect of NAC during treatment is mainly assessed based on size changes of the tumor as measured with clinical examination, on ultrasonography or magnetic resonance imaging (MRI). Since underlying metabolic tumor changes in response to treatment usually precede the relatively slow process of change in tumor size (9–12), monitoring of tumor metabolism may offer a faster and better window to assess therapy response.

Pathological response

The pathological response to NAC treatment is determined by the pathologist on the resected tissue after surgery. The response is defined according to the Miller-Payne system (13); complete response is classified as grade 5 and non-response as grade 1. Pathological non-response indicates no change or some alteration to individual malignant cells, but no reduction in overall cellularity compared to pre-therapy core biopsy.

Aim

The overall aim of this thesis is to evaluate early effects of chemotherapy after the first cycle of NAC treatment in breast cancer patients using metabolic MRI.

Metabolic MRI of breast cancer

MRI of the breast is a technique that uses amongst others a powerful magnetic field, and radio frequency pulses transmitted by coils to produce detailed images of the structures within the breast. Inside the strong magnetic field, the nuclei of different isotopes in the body (^1H and ^{31}P are used in this thesis) will behave like small spinning dipoles which will align (parallel or anti-parallel) with the direction of the main magnetic field. The alignment of the spinning dipoles can be disturbed by applying a radiofrequency (RF) pulse equal to the spinning frequency of these dipoles. The dipoles return to their resting alignment through various relaxation processes and in this manner emit RF energy which can be measured.

MR spectroscopy (MRS) exploits the fact that due to electronic shielding inside the molecule, the nucleus will resonate at a slightly different frequency depending on its position within the molecule. This provides each molecule with a nuclear magnetic resonance specific 'fingerprint'. In MRS, this way, signals originating from different molecules (or different positions in molecules) can be recognized and measured.

In MRI usually only the resonance frequency of water is considered. By using additional field gradients, the signal can be made location dependent and transferred into an image. MRI is mainly used to investigate the anatomy and physiology of the human body and is primarily used as a supplemental tool during diagnostic work-up of breast cancer patients, in combination with mammography and ultrasound. Clinical MR scanners typically have a field strength of 1.5 T or 3 T. The advantages of using higher field strength MR systems include higher signal-to-noise ratio (SNR), and higher spatial and temporal resolution. To obtain information about metabolism in vivo, the even higher field strength of 7 T is preferred due to the significantly higher SNR and contrast-to-noise ratio (CNR). Especially MRS benefits from the increased spectral resolution enabling detecting of individual metabolites.

Metabolic MRI is a collective name for non-invasive MRI techniques which can give new insights in understanding tissue metabolism in vivo. Among these techniques are phosphorous MRS (^{31}P-MRS) and chemical exchange saturation transfer (CEST) MRI which are described in more detail below.

^{31}P-MRS

The cell membrane is primarily composed of phospholipids and proteins (phospholipid bilayers). The most important backbone of these lipid chains is phosphatidylserine which is anabolized through the Kennedy pathway (14) in which choline containing metabolites play an important role (Figure 2).

Since the introduction of MRS in clinical studies, proton MRS (^{1}H-MRS) that has the highest MR-sensitivity to assess metabolites involved in choline metabolism. However, with ^{1}H-MRS, only one signal is observed, which for convenience is called total choline (tCho, total of the blue boxes in Figure 2). tCho concentrations have been related to cancer malignancy, with increasing choline levels relating to increased malignancy. Albeit at a low specificity due to the signal overlap from many individual metabolites (15). Moreover, the tCho signal in ^{1}H-MRS in breast cancer is often contaminated by large signals of lipids and water that are present in the normal breast tissue. With ^{31}P-MRS, the tCho signal can be specified into the signals of phosphomonoesters (PME) and phosphodiesters (PDE) which are known to be involved in anabolism and catabolism of the cell membrane (16,17). The PMEs are phosphocholine (PC) and phosphoethanolamine (PE), and the PDEs are glycerophosphocholine (GPC) and glycerophosphoethanolamine (GPE) (Figure 2). Elevated levels of PME over PDE
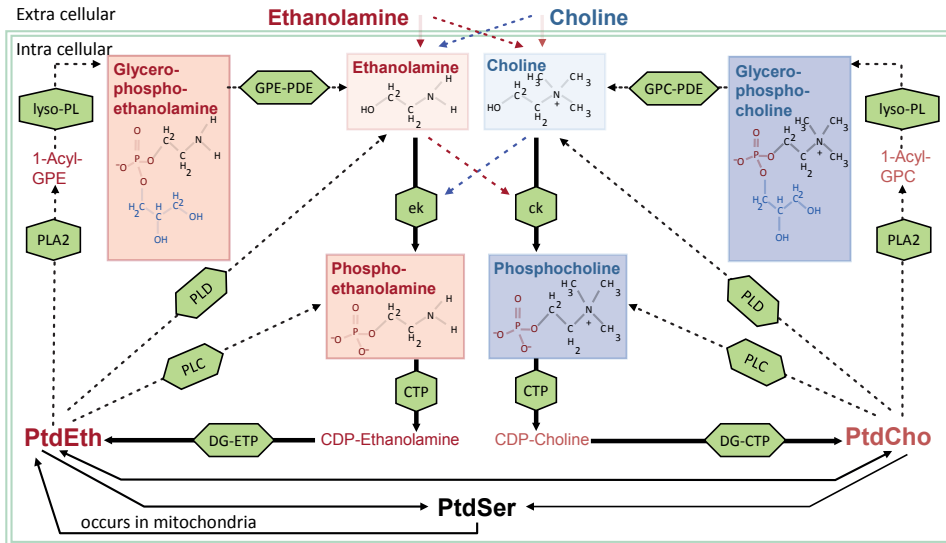
Figure 2 Network of ethanolamine and choline phospholipid metabolism. MRS-detectable metabolites are shown in red (ethanolamine) and blue (choline) boxes. Anabolic enzyme reaction are depicted by solid arrows and catabolic enzyme reactions by dotted arrows. Enzymes are shown in green boxes. Important note, the total signal of the blue boxes can be measured with ^{1}H-MRS, while with ^{31}P-MRS it is possible to measure different metabolites individually.
Wijnen JP et al. NMR Biomed. 2014;27(6):692–9.

(PME/PDE ratio) have been associated with the presence of cancer and mitotic count (18).

Also alterations in energy metabolism can be monitored with ^{31}P-MRS through levels of adenosine triphosphate (ATP) and inorganic phosphate (Pi) levels. Moreover, the chemical shift position of Pi is a direct marker of intracellular pH, which can be detected with high accuracy at 7 T with ^{31}P-MRS due to its high spectral resolution (19). ^{31}P-MRS in breast cancer patients at 7 T has been successfully performed within clinically feasible scanning time (20). The potential of using ^{31}P-MRS to detect changes in metabolism during NAC has been described (21). These changes were measured halfway (~3 months) and at the end of NAC treatment (~6 months). However, in this thesis, it is investigated if ^{31}P-MRS has the potential to detect changes in metabolism right after the first cycle (after two weeks) of NAC treatment.

CEST-MRI

Chemical exchange saturation transfer (CEST) MRI is a potentially more sensitive metabolic imaging technique than MRS, and has been of great interest the last few years (22). This MRI method is a powerful and sensitive technique in which low concentration solutes can be visualized through the water signal. The image contrast depends on the concentration and exchange rate of MR saturated mobile protons to the bulk water resonance. This enables indirect imaging of endogenous molecules containing these mobile protons (22). The most widely reported CEST effect is derived from the exchange of amide protons on the backbone of proteins and peptides which is called amide proton transfer (APT). It has been shown that APT-CEST can discriminate tumor from healthy tissue and, more recently, APT-CEST has been suggested as a biomarker for response to therapy in breast cancer patients (23). Moreover, the CEST effect is directly mediated with the acidity of the tissue, therefore indirectly also an indicator of pH. Consequently however, APT-CEST is less specific than ^{31}P-MRS, but in contrast to ^{31}P-MRS, more widely available on MRI systems, also at lower field strengths. As for ^{31}P-MRS, specific hardware (coils tuned to the phosphorous frequency) are necessary, which are not widely available.

Breast coil

Imaging at 7 T forces the use of local transmit coils due to the absence of a body coil. One of the challenges with these coils is the decaying RF field more distant from the coil (inhomogeneous transmit field). Despite the great potential, breast imaging at 7 T is not yet used routinely for clinical breast MRI examinations, mainly due to this challenge. A homogeneous transmit field is particularly important for MR sequences such as a turbo spin echo. (TSE), which can still not compete to the clinical standard at 3T (24). Clinical usability is also impeded by the limited penetration depth as it is important to image the axillary lymph nodes.

The use of dipole antennas (25) for imaging at 7 T has shown enhanced transmit field homogeneity and penetration depth compared to loop coils (26), which are often used in other breast coil designs. Since these antennas have to potential to address the main issues with breast imaging at 7 T, we developed a bilateral breast coil with dipole antennas in this thesis.

Outline of this thesis

This thesis explores the use of metabolic MRI at 7 T to detect early changes in breast cancer patients during NAC treatment. In particular ^{31}P-MRS and CEST-MRI were investigated to detect these changes.

In **Chapter 2**, ^{31}P-MRS was performed before and after the first cycle of NAC treatment in breast cancer patients. Metabolic ratios involved with membrane metabolism obtained from ^{31}P-MRS were subsequently related to the pathological response to NAC treatment. It is investigated whether different pathological responders (non-responders, partial responders and complete responders) can be distinguished based on the change of these metabolic ratios.

In **Chapter 3**, the same approach as chapter 2 was exploited, however this time with CEST-MRI. APT signal originating from amides attached to the backbone of proteins and peptides obtained with CEST-MRI was related to the pathological response to NAC treatment. CEST-MRI was acquired in a small group of breast cancer patients before and after the first cycle of NAC treatment. This feasibility study will investigate if CEST-MRI at 7 T can be used as a non-invasive biomarker to predict the effect of NAC in an early stage of treatment.

In **Chapter 4**, the observexd changes in APT signal with CEST-MRI in chapter 3 were in opposite direction as hypothesized. The hypothesis is that APT signals have a positive linear relation exchange rate (influenced by pH) and amide content. In non-responders, an increase of APT signal was observed while a previous study (21) showed a decrease in pH during NAC treatment, contradicting the intrinsic positive relation of APT signal to pH. In this chapter, APT CEST-MRI is investigated in more detail by relating it to pH measured with ^{31}P-MRS to improve comprehension of underlying mechanisms of APT CEST-MRI. This may reveal new insights of the main contributor of the APT signal in vivo in breast cancer.

In **Chapter 5**, the first steps are taken to merge metabolic imaging with ultra-high resolution MRI of the breast. A new bilateral breast coil setup is discussed to improve image quality for breast imaging at 7 T. The use of five meandering dipole antennas in a multi-transmit setup, combined with a high density receive array is explored. It is investigated whether the coil improves image quality and is able to image the axillary lymph nodes. Both are necessary for translating routinely used breast imaging protocols from 3 T to 7 T.

In **Chapter 6**, the success of evaluating early changes with ^{31}P-MRS and CEST-MRI in breast cancer after the first cycle of NAC treatment is summarized and the application of these techniques in breast cancer are discussed.

References

1.   Paap E, Broeders MJM, van Schoor G, Otten JDM, Verbeek ALM. Large increase in a Dutch woman's lifetime risk of developing breast cancer. Eur J Cancer. 2008;44(11):1485–7.
2.   Lee YN (Margaret. Breast carcinoma: Pattern of metastasis at autopsy. J Surg Oncol. 1983;23(3):175–80.
3.   American Joint Committee on Cancer (AJCC). AJCC Cancer Staging Manual, Eighth Edition: Breast. Vol. 39, Cancer Treatment Reviews. 2017. 1355-1359 p.
4.   Kümmel S, Holtschmidt J, Loibl S. Surgical treatment of primary breast cancer in the neoadjuvant setting. Br J Surg. 2014;101(8):912–24.
5.   Curigliano G, Burstein HJ, Winer EP, Gnant M, Dubsky P, Loibl S, et al. De-escalating and escalating treatments for early-stage breast cancer: The St. Gallen International Expert Consensus Conference on the Primary Therapy of Early Breast Cancer 2017. Ann Oncol. 2017;28(8):1700–12.
6.   Singal PK, Iliskovic N. Doxorubicin-Induced Cardiomyopathy. N Engl J Med. 1998;339(13):900–5.
7.   Nabholtz J-M, Gligorov J. The role of taxanes in the treatment of breast cancer. Expert Opin Pharmacother. 2005;6(7):1073–94.
8.   Early Breast Cancer Trialists' Collaborative Group (ECBTCG). Long-term outcomes for neoadjuvant versus adjuvant chemotherapy in early breast cancer: meta-analysis of individual patient data from ten randomised trials. Lancet Oncol. 2018;19(1):27–39.
9.   Tudorica A, Oh KY, Chui SYC, Roy N, Troxell ML, Naik A, et al. Early prediction and evaluation of breast cancer response to neoadjuvant chemotherapy using quantitative DCE-MRI. Transl Oncol. 2016;9(1):8–17.
10. Harry VN, Semple SI, Parkin DE, Gilbert FJ. Use of new imaging techniques to predict tumour response to therapy. Lancet Oncol. 2010;11(1):92–102.
11. Padhani AR, Miles KA. Multiparametric Imaging of Tumor Response to Therapy. Radiology. 2010;256(2):348–64.
12. Cortazar P, Zhang L, Untch M, Mehta K, Costantino JP, Wolmark N, et al. Pathological complete response and long-term clinical benefit in breast cancer: The CTNeoBC pooled analysis. Lancet. 2014;384(9938):164–72.
13. Ogston KN, Miller ID, Payne S, Hutcheon AW, Sarkar TK, Smith I, et al. A new histological grading system to assess response of breast cancers to primary chemotherapy : prognostic significance and survival. Breast. 2003;12:320–7.
14. Kennedy EP, Weiss SB. The function of cytidine coenzymes in the biosynthesis of phospholipides. J Biol Chem. 1956;222(1):193–214.
15. Bolan PJ, Meisamy S, Baker EH, Lin J, Emory T, Nelson M, et al. In Vivo Quantification of Choline Compounds in the Breast with 1H MR Spectroscopy. Magn Reson Med. 2003;50(6):1134–43.
16. Podo F. Tumour phospholipid metabolism. NMR Biomed. 1999;12(7):413–39.
17. Glunde K, Bhujwalla ZM, Ronen SM. Choline metabolism in malignant transformation. Nat Rev Cancer. 2011;11(12):835–48.
18. Schmitz AMT, Veldhuis WB, Menke-Pluijmers MBE, Van Der Kemp WJM, Van Der Velden TA,

1

Kock MCJM, et al. Multiparametric MRI with dynamic contrast enhancement, diffusion-weighted imaging, and 31-phosphorus spectroscopy at 7 T for characterization of breast cancer. Invest Radiol. 2015;50(11):766–71.

19.   Moon RB, Richards JH. Determination of Intracellular pH by 31P Magnetic Resonance. J Biol Chem. 1973;248(25):7276–8.

20.   Klomp DWJ, Bank BL Van De, Raaijmakers A, Korteweg MA, Possanzini C, Boer VO, et al. 31P MRSI and 1H MRS at 7T : initial results in human breast cancer. NMR Biomed. 2011;24:1337–42.

21.   Kemp WJM Van Der, Stehouwer BL, Luijten PR, Bosch MAAJ Van Den, Klomp DWJ, Den MAAJ Van, et al. Detection of alterations in membrane metabolism during neoadjuvant chemotherapy in patients with breast cancer using phosphorus magnetic resonance spectroscopy at 7 Tesla. Springerplus. 2014;3(1):634.

22.   van Zijl PCM, Yadav NN. Chemical Exchange Saturation Transfer (CEST): what is in a name and what isn't? Magn Reson Med. 2012;65(4):927–48.

23.   Dula AN, Arlinghaus LR, Dortch RD, Dewey E, Whisenant JG, Ayers GD, et al. Amide proton transfer imaging of the breast at 3 T: Establishing reproducibility and possible feasibility assessing chemotherapy response. Magn Reson Med. 2013;70:216–24.

24.   Laader A, Beiderwellen K, Kraff O, Maderwald S, Wrede K, Ladd ME, et al. 1 . 5 versus 3 versus 7 Tesla in abdominal MRI : A comparative study. 2017;1–18.

25.   Raaijmakers AJE, Ipek O, Klomp DWJ, Possanzini C, Harvey PR, Lagendijk JJW, et al. Design of a radiative surface coil array element at 7 T: The single-side adapted dipole antenna. Magn Reson Med. 2011;66(5):1488–97.

26.   Raaijmakers AJE, Luijten PR, van den Berg CAT. Dipole antennas for ultrahigh-field body imaging: a comparison with loop coils. NMR Biomed. 2016;29(9):1122–30.

Early detection of changes in phospholipid metabolism during neoadjuvant chemotherapy (NAC) in breast cancer patients using phosphorus magnetic resonance spectroscopy at 7 tesla.

Erwin Krikken
Wybe J.M. van der Kemp
Paul J. van Diest
Thijs van Dalen
Hanneke W.M. van Laarhoven
Peter R. Luijten
Dennis W.J. Klomp
Jannie P. Wijnen

2

Abstract

Purpose: The purpose of this work was to investigate whether non-invasive early detection (after the first cycle) of response to neoadjuvant chemotherapy (NAC) in breast cancer patients was possible. ^{31}P-MRSI at 7 tesla was used to determine different phosphor metabolites ratios and correlate this to pathological response.

Methods: ^{31}P-MRSI was performed in twelve breast cancer patients treated with NAC. [31]P spectra were fitted and aligned to the frequency of phosphoethanolamine (PE). Metabolic signal ratios for phosphomonoesters/phosphodiesters (PME/PDE), phosphocholine/glycerophosphatidylcholine (PC/GPtC), phosphoethanolamine/ glycerophosphoethanolamine (PE/GPE) and phosphomonoesters/in-organic phosphate (PME/Pi) were determined from spectral fitting of the individual spectra and the summed spectra before and after the first cycle of NAC. Metabolic ratios were subsequently related to pathological response. Additionally, the correlation between the measured metabolic ratios and Ki-67 levels was determined using linear regression.

Results: Four patients had a pathological complete response after treatment, five patients a partial pathological response and three patients did not respond to NAC. In the summed spectrum after the first cycle of NAC, PME/Pi and PME/PDE decreased with 18% and 13%, respectively. A subtle difference between the different response groups may be observed in PME/PDE, where the non-responders showed an increase and the partial and complete responders a decrease (p=0.32). No significant changes in metabolic ratios were found. However, a significant association between PE/Pi and Ki-67 index was found (p=0.03).

Conclusions: We demonstrated that it is possible to detect subtle changes in ^{31}P metabolites with a 7 T MR system after the first cycle of NAC treatment in breast cancer patients. Non-responders showed different changes in metabolic ratios compared to partial and complete responders, in particular for PME/PDE, yet more patients need to be included to investigate its clinical value.

Keywords: Breast imaging; 31P-MRSI; High field; 7 tesla

Introduction

Breast cancer is the most common cancer in women worldwide (1). Neoadjuvant chemotherapy (NAC) is increasingly used for pre-surgical treatment with the main purpose of downsizing locally advanced tumors to make them better candidates for resection (2). The recent St. Gallen consensus (3) suggested a preference for NAC treatment in human epidermal growth factor receptor 2 positive (HER2+) subtypes and triple negative breast cancer, stage II and III. This preference was extended to women who were eligible for breast conserving surgery at diagnosis. It has been shown that the desired tumor size reduction is not accomplished with NAC in up to 31% of patients who will have stable or even progressive disease (4). In order to identify patients who will have stable or progressive disease, it is important to identify biomarkers that can assess the response to NAC at an early stage in the individual patient. This could enable the adjustment of systemic therapy and avoid toxicity and the related costs of ineffective treatment.

Currently, the effect of NAC during treatment is mainly quantified based on changes in tumor size upon clinical examination, using ultrasonography or MRI. Since underlying metabolic changes in response to treatment usually precede the relatively slow changes in tumor size (5–8), monitoring of tumor metabolism may offer a earlier and better window to assess therapy response. Phosphorous magnetic resonance spectroscopic imaging (^{31}P-MRSI) of the breast, makes it possible to assess changes in tumor metabolism. Metabolites of interest such as the phosphomonoesters (PME) (phosphocholine (PC) and phosphoethanolamine (PE)), and phosphodiesters (PDE) (glycerophosphocholine (GPC) and glycerophosphoethanolamine (GPE)) are known to be involved in anabolism and catabolism of the cell membrane (9,10). Additionally, signals of mobile phospholipids glycerophosphatidylcholine (GPtC) and glycerophosphatidylethanolamine (GPtE), and metabolites involved in energy metabolism such as in-organic phosphate (Pi) and adenosinetriphosphate (ATP) can be measured with ^{31}P-MRS (11–13).

In the presence of cancer, elevated PME/PDE levels have been measured, where in most human tumors PE prevails over PC (14). In case of effective response to systemic therapy, a fall in PME to PDE levels is observed (15). In addition, it was shown that PME/PDE for triple negative tumors were low compared to estrogen/progesterone receptor positive (ER+/PR+) tumors (16,17). Other studies demonstrated that ER-breast cancer is associated with low PC and high GPC concentrations (18) and that

an overall reduction in PC and GPC concentration after the complete course of NAC treatment has been observed (19) and associated with long-term survival (20).

These previous studies were performed on tissue samples ex vivo with either proton MRS (^{1}H-MRS) or high resolution magic angle spinning MRS (HR MAS MRS) or in vivo with at lower field strengths (up to 3 tesla; 3 T). At 3 T however, neighboring peaks with similar frequency, for example the phosphodiesters are indistinguishable and therefore moving up to 7 T is necessary. Studies have shown that ^{31}P-MRS at 7 T enables *in vivo* detection and quantification of phospholipid metabolites (21,22) with acceptable acquisition times and sufficient spatial resolution, particularly when using multi-echo acquisitions (23).

In previous work, examining the feasibility of measuring *in vivo* changes in phospholipid metabolites during NAC using ^{31}P-MRSI (24), we reported a decreased PME/PDE and PME/Pi halfway NAC and after the end of NAC. Therefore, the aim of this current study, in a different cohort of patients, was to assess the possibility to detect these changes even earlier, directly after the first cycle of NAC using ^{31}P-MRS at 7 T, and to test the feasibility to differentiate pathological response levels to NAC.

Materials and Methods

Patients

This MRI study was performed in accordance with the guidelines of the UMC Utrecht ethics committee (trialregister.nl: NTR4980). Twelve breast cancer patients (mean age: 49 years; range: 36-64 years) gave informed consent to participate in this study. The patients were selected for treatment with NAC, and were examined with ^{31}P-MRSI before and after the first cycle of NAC (at ~3 week intervals). Table 1 summarizes the demographics and tumor characteristics of these patients.

Pathology

All patients underwent surgery after completing NAC treatment and the pathological responses to NAC were defined according to the Miller-Payne system (25); complete response is classified as grade 5 and non-response as grade 1. Pathological non-response indicates no change or some alteration to individual malignant cells, but no reduction in overall cellularity compared to pre-therapy core biopsy. Grades 1 and 2 were grouped together as non-responders, grades 3 and 4 as partial responders and grade 5 as complete

Table 1 Demographics, tumor characteristics and pathological response of breast cancer patients undergoing neoadjuvant chemotherapy.

Patient	Age (years)	Treatment regimes	ER	PR	HER2neu	TNM	PR*	Ki-67 (%)
1	56	6x taxotere - AC	-	-	-	T2N0M0	5	40
2	60	6x taxotere - AC	+	-	-	T2N0M0	4	10
3	64	6x taxotere - AC	+	+	-	T2N1M0	3	10
4	36	6x taxotere - AC	-	-	-	T2N0M0	2	40
5	62	4x AC – 4x taxotere with concomitant trastuzumab	+	-	+	T2N1M0	5	65
6	60	3x FEC – 3x docetaxel	+	+	-	T2N1M0	2	65
7	40	3x FEC – 3x docetaxel	+	-	-	T3N2M0	4	5
8	43	4x AC – 4x taxotere	-	-	-	T2N0M0	4	20
9	40	4x AC – 12x paclitaxel	-	-	-	T2N3M0	2	50
10	37	4x AC – 4x taxotere	+	+	-	T2N1M0	3	30
11	49	4x AC – 4x taxotere with concomitant trastuzumab	-	-	+	T2N0M0	5	35
12	44	4x AC – 4x taxotere with concomitant trastuzumab	-	-	+	T2N0M0	5	5

ER Estrogen Receptor; *PR* Progesterone Receptor; *HER2* Human Epidermal growth factor Receptor 2; *TNM stage* Classification of malignant tumors (Tumor, Nodes, Metastasis); *AC* Adriamycin and Cyclophosphamide; *FEC* 5-Fluorouracil, Epirubicin and Cyclophosphamide
*PR = pathological response according to the Miller-Payne system

2

responders. For investigating cell proliferation, immunohistochemistry for Ki-67 was carried out in the pre-therapy core biopsy, with a cut-off point of 20% (26–29).

Acquisition

All patients were scanned in prone position with a unilateral two channel ^{1}H/^{31}P dual-tuned breast coil (MR Coils, Zaltbommel, The Netherlands) on a 7 T MR system (Philips, Best, The Netherlands) without contrast agent. The scan session consisted of a fat suppressed T_1 weighted 3D MRI (TE = 2 ms; TR= 4 ms; flip angle = 10 °; FOV = 160 x 160 x 160 mm^3; isotropic resolution of 1.0 mm^3). Fat suppression was achieved by using a short 1-2-1 spectral-spatial RF pulse. Third-order B_0 shimming was performed with least square error optimization using a 3D B_0 with manual segmentation of the breast (30). ^{31}P-MRSI was obtained using the AMESING sequence (23), in which 1 FID and 5 full echoes were acquired within one TR, resulting in an FID at 0.45 ms and echoes at 45, 90, 135, 180 and 225 ms respectively. Additional parameters were TR = 6 s; FOV 160 x 160 x 160 mm^3; 8 x 8 x 8 voxels; 2 x 2 x 2 cm^3 nominal resolution; BW = 8200 Hz; sampling matrix size = 256; resulting in a total scan time of 25:36 min for the ^{31}P-MRSI, excluding the standard imaging and shimming.

Data analysis

All MRSI data were analyzed using IDL 6.3 (Research Systems, Boulder, CO, USA), jMRUI 4.0 (31) and Matlab 2017a (MathWorks, Natick, MA, USA). Selection of the voxel containing the breast tumor was performed using in-house Matlab scripts. All spectra were zero-filled to 8192 data points and apodized (15 Hz Lorentzian) in the time domain and spatially Hamming filtered. To maximize the signal-to-noise ratio (SNR), the FID and five echoes were corrected for the difference in T_2 relaxation of each metabolite for every individual patient. In a previous study, the T_2 relaxation times of the different metabolites (nine in total) were determined based on the average spectra of that patient group (32). A spline interpolation between the T_2 relaxation time and the chemical shift of the metabolites was used to calculate the weighted sum of the FID and five echoes.

After the T_2-weighting of the spectra, all spectra were frequency aligned to PE at 6.83 ppm. The individual metabolites were fitted in jMRUI using the AMARES algorithm (31). During the fitting, the overall phases were fixed to zero and the linewidth of PE had soft constraints with a minimum of 10 Hz and maximum of 40 Hz. The linewidths

of PC, Pi and the diesters were set as a fixed ratio of the linewidth of PE. The chemical shift of PE was kept in the range of 6.79 to 6.89 ppm, the chemical shift of GPE in the range of 3.3 to 3.6 ppm and the chemical shift of GPtC in the range of 2.25 to 2.35 ppm. Metabolic signal ratios for PME/PDE, PC/GPtC, PE/GPE and PME/Pi were calculated from the spectral fitting of the patients individually. To increase SNR even further and to observe general changes in the complete patient group, the spectra before and after the first cycle of NAC from all patients were summed separately. To investigate the differences between non-responders, partial responders and complete responders, the spectra of the patients in the three groups were summed up separately as well. The change in ratios (before NAC compared to after the first cycle of NAC) were determined and compared with the pathological response . Also, the mean PME/PDE ratio in triple negative tumors was compared to the mean PME/PDE ratio of the rest of the patients.

Statistical Analysis

Statistical analysis was performed using an unpaired Mann-Whitney test (GraphPad Prism, GraphPad Software, San Diego, CA, USA), with a two-tailed distribution to determine whether the metabolic ratios were significantly changed ($\alpha = 0.05$) after the first cycle of NAC. For the correlation between the measured metabolic ratios before NAC treatment (baseline) and Ki-67 levels, linear regression was performed and was considered statistically significant if $p < 0.05$.

A Kruskal Wallis test with a post-hoc Dunn's multiple comparison test was used to assess statistical difference in metabolite ratios between the patient groups with different pathological responses (non-responders, partial responders and complete responders).

Results

Three patients had a HER2+ tumor and the other patients had HER2- tumors. Six tumors were ER+, three of these were PR+, and four triple negative tumors were included in this study. All patients completed all cycles of NAC; four patients had a pathological complete response after treatment and five patients had a partial pathological response and three patients showed no response (Table 1). All three HER2+ subtypes had a complete response to NAC treatment.
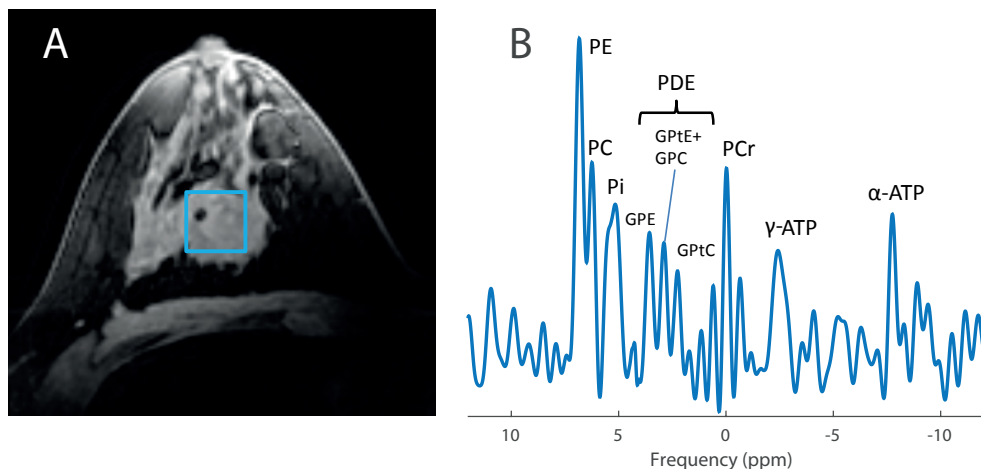
Figure 1 Example data of a patient with a ER+, PR+, HER2- tumor. T_1 weighted 3D FFE image (A) with a representation of the selected voxel (blue square) for ^{31}P analysis. The corresponding T_2 weighted spectrum (B) shows all 9 fitted metabolites.

After selecting the voxel location in the middle of the tumor (Figure 1), the spectrum clearly showed all 9 metabolites, including all three peaks of PDE. In the summed spectra for all patients (Figure 2), a broad Pi peak compared to the other metabolites was observed. After the first cycle of NAC, PME/Pi and PME/PDE decreased with 18% and 13%, respectively.
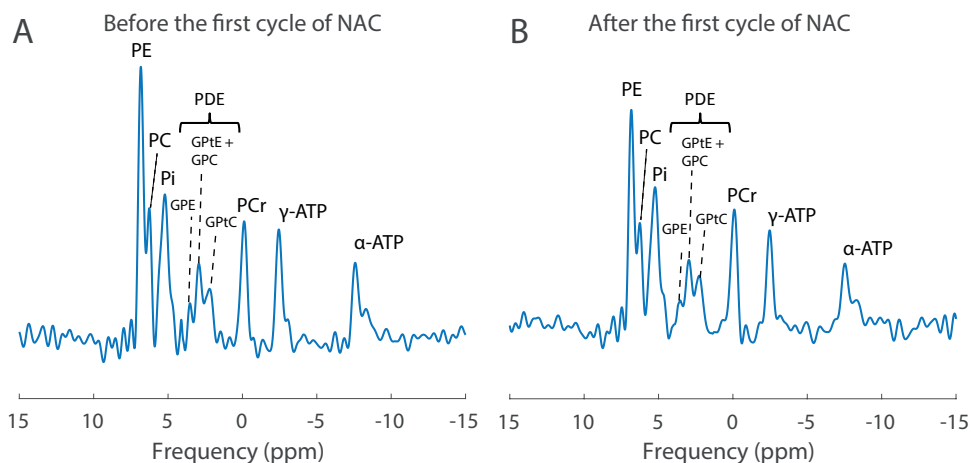

Figure 2 Summed spectrum of all patients before (A) and after the first cycle (B) of NAC with all fitted ^{31}P metabolites clearly visible.

Metabolic ratios involved in membrane and energy metabolism were calculated for all patients. No significant differences were found between the metabolic ratios measured before and after the first cycle of NAC. For all patients, PME/Pi before the start of NAC was higher than 1 and decreased after the first cycle of NAC (Figure 3).

When comparing metabolic ratios of the three pathological responses groups (Figure 4), the largest difference was observed in PME/PDE. The non-responders showed an increase and the partial and complete responders a decrease (p = 0.32). The change in PC/GPtC suggests that this ratio has a more linear distribution between the different pathological responses, showing the largest increase for the non-responders, no change to a small increase for the partial responders and a decrease of the ratio for the complete responders.

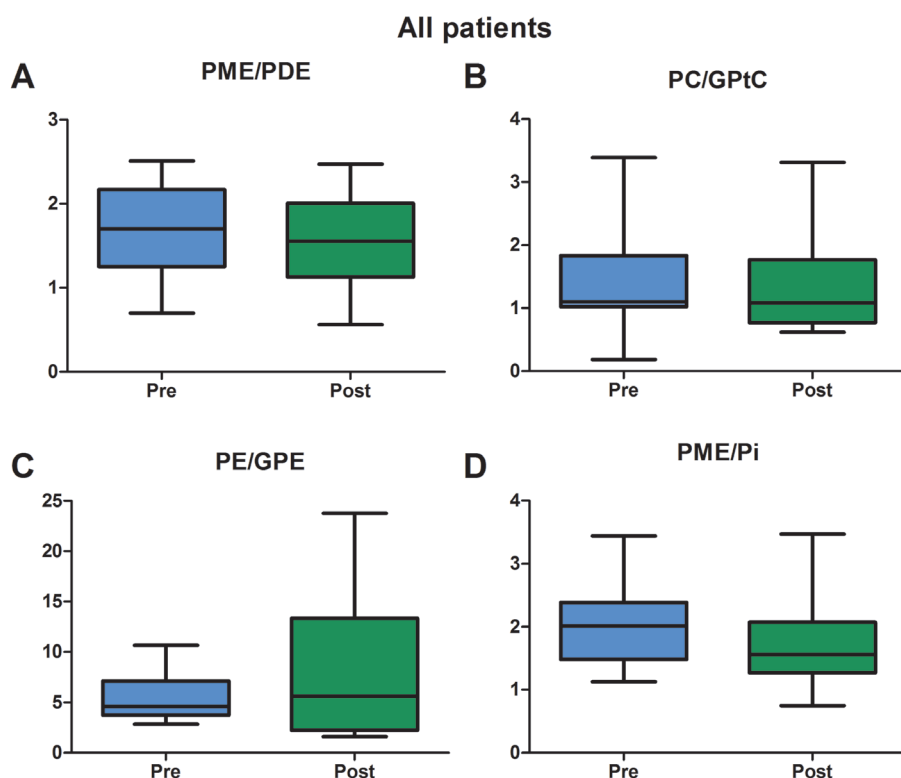**Figure 3** Whisker boxplot with 5-95 percentile of the mean metabolic ratios of different metabolites before (blue) and after the first cycle of neoadjuvant chemotherapy (green) in all patients (including all different kinds of response). All ratios show a decrease except for PE/GPE that shows an increase. However, note the high standard deviation of PE/GPE, indicating an outlier where a very large increase in this ratio was observed.

For PME/PDE we had a closer look (Figure 5) to see if the results still held for the individual fits instead of the summed spectra of the different response groups. Two of the three non-responders showed an increase in the ratio as the other non-responders showed only a small decrease. However, two of the five partial responders also showed an increase of PME/PDE. Three out of four complete responders showed a decreased PME/PDE, however no significant difference was found (p = 0.89).
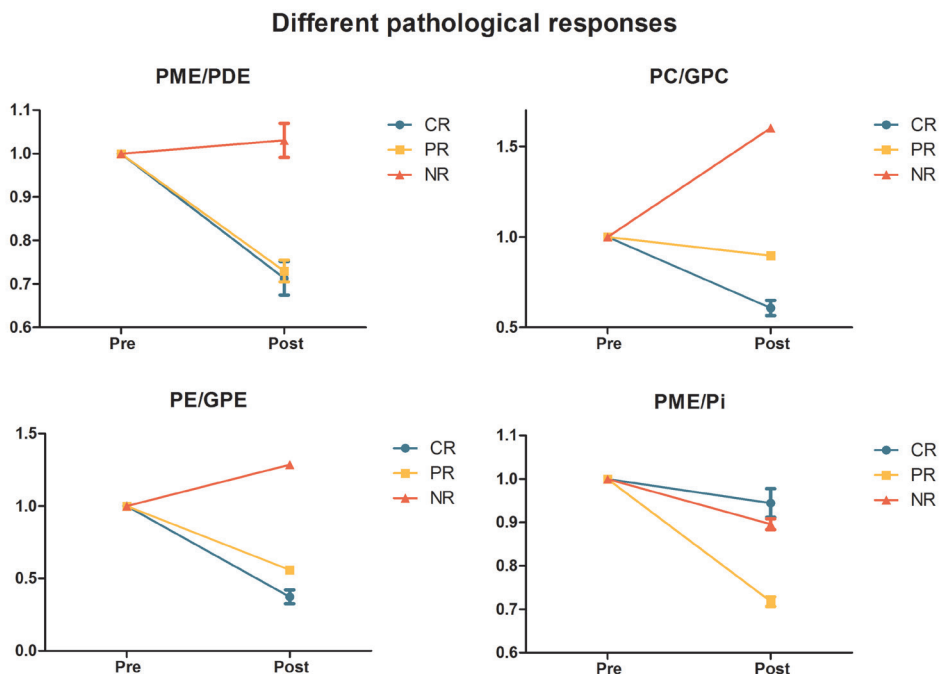
Figure 4 Changes in metabolic ratios with standard deviation before (pre) and after the first cycle of neoadjuvant chemotherapy (post) for the different pathological responses (CR=complete responders; PR=partial responders; NR=non responders) where the ratios before neoadjuvant chemotherapy are normalized to one. This data was obtained by spectral fitting of the summed spectra of the different pathological responses.. Note that the direction of the change in PME/PDE for the non-responders is in opposite direction compared to the complete and partial responders. The shown standard error is the fitting error and not the deviation between different patients.

All metabolic ratios were correlated with the Ki-67 index (Figure 6). A significant statistical association between PE/Pi and Ki-67 index was observed (p = 0.03), all other ratios were not significantly correlated with the Ki-67 index. The Kruskal-Wallis test with the post-hoc Dunn's multiple comparison test showed no significant differences between the three different pathological responses for the metabolic ratios after the first cycle of NAC.
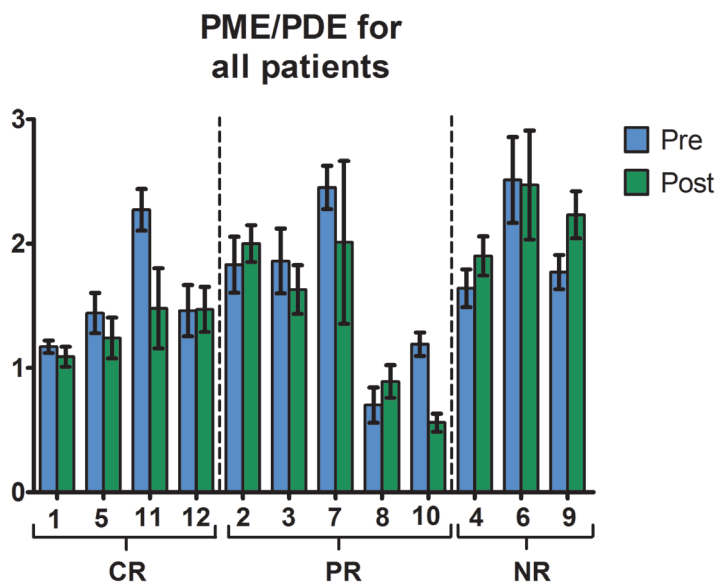
Figure 5 PME/PDE measured after spectral fitting of the individual ^{31}P spectra before (blue) and after the first cycle of NAC (red) arranged for the different pathological responses. The numbers below the graphs correspond to the patient numbers in Table 1 and the standard deviation is the standard error of the fit. In some cases (patient 1, 2, 3 and 11), GPE could not be fitted.
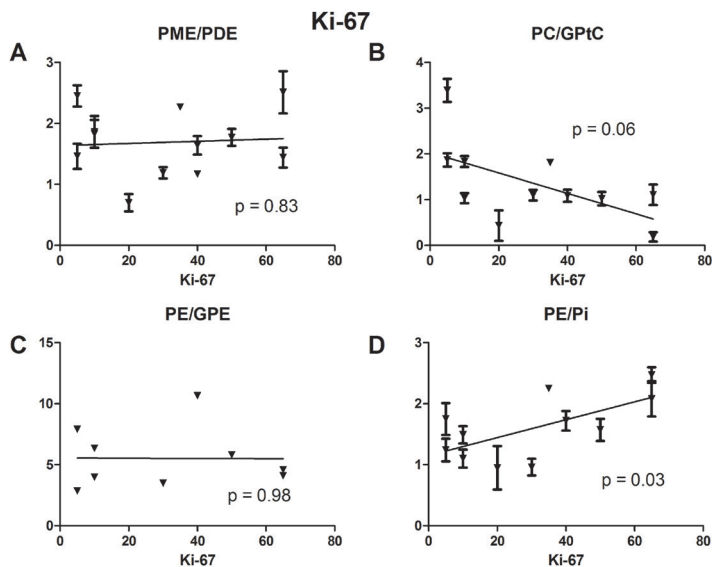
Figure 6 The different metabolic ratios of all patients before NAC treatment against Ki-67 index with the corresponding p-values.

Discussion

The potential of using ^{31}P-MRSI for treatment response assessment in tumors has been shown in previous studies (9,24,33–36). In this preliminary study, we demonstrated that changes in phospholipid metabolites can be detected after the first cycle of NAC and that these changes might be related to the different pathological responses. For PME/PDE, the group of non-responders showed an increased ratio after the first cycle of NAC treatment while the partial and complete responders showed a decrease of this ratio. However, when we looked at the individual fits of PME/PDE, two of the five partial responders showed an increase in this ratio. The main reason for this discrepancy is probably the lower SNR for the individual spectra compared to the summed spectra of the different groups. In some of the metabolic ratios (PME/PDE and PME/Pi) a large variation between patients was observed, which is probably due to physiological differences in the heterogeneous patient group of our study including different kinds of tumors and different kinds of NAC treatment. It has been shown in several studies that estrogen and progesterone can be involved in activation of choline-kinase (16,37). However, in this study no correlations were found between the metabolic ratios and ER status and PR status, which is probably due to the relatively low number of patients included. A larger patient population is required for a more comprehensive analysis of change in the different metabolic ratios in relation to the pathological response, which due to FDA clearance on 7T MRI is expected to become a reality in the near future. Additionally, no contrast agent was used during acquisition, theoretically enabling the possibility to restage the tumor several times during treatment, which is an advantage for the patient given the controversy in the use of gadolinium (38).

A linear relation was found in this study between PE/Pi before NAC and the Ki-67 index. This was expected, as PE is an important metabolite involved in the membrane metabolism and Ki-67 index is a marker for cell proliferation, which are closely related to each other. In the summed spectrum of all patients, however, no significant differences in the metabolite levels were found between the two measurements. A possible explanation could be that in the summed spectrum all pathological responses are included. The observed decreases in PME/PDE and PME/Pi after the first cycle of NAC correspond with findings in a previous study that measured these metabolite ratios after three cycles of NAC (24).

In line with another study (15), high PME/PDE in the tumor tissue were observed in our study with a mean ratio of 1.69, compared to healthy volunteers (mean ratio of 0.70

(32)). Preclinical work and animal models (16,17) have shown that PME/PDE for triple negative tumors are low compared to ER+/PR+ tumors. In the present study we showed that these findings still hold for measurement in breast cancer patients, with a mean PME/PDE for triple negative tumors of 1.32 ± 0.42 compared to a mean PME/PDE of 1.88 ± 0.46 for the other patients.

The PME/Pi is a tissue viability marker that may be used as an early marker for tumor cell apoptosis in radiation therapy (39). Also in hepatic lymphomas, increased levels of PME/Pi were observed which decreased after admission of chemotherapy. They concluded that the drugs reached the target cells and affected tumor cell metabolism or killed the tumor cells (40). In all patients in this study, PME/Pi was higher than 1 and decreased after the first cycle of NAC, supporting the findings in a previous study in breast cancer patients at 7 T (24), and in line with studies in other settings. However, caution is needed when drawing conclusions from this ratio in breast cancer patients. If the tumor is closely situated near the pectoral muscle, the PME/Pi can be contaminated with the Pi signal originating from the pectoral muscle.

The broadening of the Pi peak, as compared to the other metabolites, is possibly related to pH differences between tumors but also pH changes during chemotherapy. As the chemical shift of Pi is sensitive to pH changes, a broadening is expected when summing the patients spectra before and after NAC treatment. The spectra of the different pathological responses also showed broadening of the Pi peak, suggesting that the Pi shift is not dependent on the pathological response to the therapy.

We were able to perform analysis for every individual patient, however in some patients one of the metabolites could not be fitted (GPE in most cases). This was mainly due to low SNR, which makes the fit of overlapping peak unreliable, particularly for the phosphodiesters. This resulted in some outliers for example in PC/GPtC and PE/ GPE. To gain more SNR we decided to sum the spectra for every different pathological response resulting in good spectra where all nine metabolites were clearly visible. The SNR of the ^{31}P MR spectra is low even at 7 T, which indicates that translation of the technology to more widely available 3 T MRI systems may be out of reach. However, technologies like polarization transfer (41) and local ^{31}P receiver arrays (42) with uniform transmit (43) are expected to improve SNR that could be translated to reduce scan times or improve accuracy in the detection of the ^{31}P metabolites. A body coil will generate a more homogeneous transmit field, making adiabatic pulses unnecessary, enabling shorter TR and via Ernst angle excitations an improved SNR in the same scan

time. The use of local receive array coils could even speed up the acquisition by using parallel imaging techniques.

Conclusion

We demonstrated that changes in ^{31}P metabolites can be detected by 7 T MRI after the first cycle of NAC in breast cancer patients. Modest changes between patient groups with different pathological responses were detected after the first cycle of NAC based on the different metabolic ratios. PME/PDE showed the highest potential to discriminate non-responders from partial and complete responders, yet warrants inclusion of more patients to potentially reach significance.

References

1. Torre LA, Siegel RL, Ward EM, Jemal A. Global Cancer Incidence and Mortality Rates and Trends - An Update. Cancer Epidemiol Biomarkers Prev. 2016;25(1):16–27.
2. Kümmel S, Holtschmidt J, Loibl S. Surgical treatment of primary breast cancer in the neoadjuvant setting. Br J Surg. 2014;101(8):912–24.
3. Curigliano G, Burstein HJ, Winer EP, Gnant M, Dubsky P, Loibl S, et al. De-escalating and escalating treatments for early-stage breast cancer: The St. Gallen International Expert Consensus Conference on the Primary Therapy of Early Breast Cancer 2017. Ann Oncol. 2017;28(8):1700–12.
4. Early Breast Cancer Trialists' Collaborative Group (ECBTCG). Long-term outcomes for neoadjuvant versus adjuvant chemotherapy in early breast cancer: meta-analysis of individual patient data from ten randomised trials. Lancet Oncol. 2018;19(1):27–39.
5. Tudorica A, Oh KY, Chui SYC, Roy N, Troxell ML, Naik A, et al. Early prediction and evaluation of breast cancer response to neoadjuvant chemotherapy using quantitative DCE-MRI. Transl Oncol. 2016;9(1):8–17.
6. Harry VN, Semple SI, Parkin DE, Gilbert FJ. Use of new imaging techniques to predict tumour response to therapy. Lancet Oncol. 2010;11(1):92–102.
7. Padhani AR, Miles KA. Multiparametric Imaging of Tumor Response to Therapy. Radiology. 2010;256(2):348–64.
8. Cortazar P, Zhang L, Untch M, Mehta K, Costantino JP, Wolmark N, et al. Pathological complete response and long-term clinical benefit in breast cancer: The CTNeoBC pooled analysis. Lancet. 2014;384(9938):164–72.
9. Podo F. Tumour phospholipid metabolism. NMR Biomed. 1999;12(7):413–39.
10. Glunde K, Bhujwalla ZM, Ronen SM. Choline metabolism in malignant transformation. Nat Rev Cancer. 2011;11(12):835–48.
11. Sijens PE, Wijrdeman HK, Moerland MA, Bakker CJ, Vermeulen JW, Luyten PR. Human breast cancer in vivo: H-1 and P-31 MR spectroscopy at 1.5 T. Radiology. 1988;169(3):615–20.
12. van der Kemp WJM, Stehouwer BL, Runge JH, Wijnen JP, Nederveen AJ, Luijten PR, et al. Glycerophosphocholine and Glycerophosphoethanolamine Are Not the Main Sources of the In Vivo 31P MRS Phosphodiester Signals from Healthy Fibroglandular Breast Tissue at 7 T. Vol. 6, Frontiers in Oncology. 2016. p. 29.

13.   van der Kemp WJM, Wijnen JP, Luijten PR, Klomp DWJ. Saturation-transfer effects and longitudinal relaxation times of [31] P metabolites in fibroglandular breast tissue at 7T. Magn Reson Med [Internet]. 2016;76(2):402–7. Available from: http://doi.wiley.com/10.1002/mrm.25871

14.   Negendank W. Studies of human tumors by MRS: A review. NMR Biomed. 1992;5(5):303–24.

15.   Leach MO, Verrill M, Glaholm J, Smith T a, Collins DJ, Payne GS, et al. Measurements of human breast cancer using magnetic resonance spectroscopy: a review of clinical measurements and a report of localized 31P measurements of response to treatment. NMR Biomed. 1998;11(7):314–40.

16.   Moestue S, Borgan E, Huuse E. Distinct choline metabolic profiles are associated with differences in gene expression for basal-like and luminal-like breast cancer xenograft models. BMC Cancer. 2010;10(433):1–12.

17.   Esmaeili M, Moestue SA, Hamans BC, Veltien A, Kristian A, Engebråten O, et al. In vivo 31P Magnetic Resonance Spectroscopic Imaging (MRSI) for metabolic profiling of human breast cancer xenografts. J Magn Reson Imaging. 2015;41(3):601–9.

18.   Giskeødegård G, Grinde M. Multivariate modeling and prediction of breast cancer prognostic factors using MR metabolomics. J Proteome Res. 2010;9:972–9.

19.   Cao MD, Giskeodegard GF, Bathen TF, Sitter B, Bofin A, Lonning PE, et al. Prognostic value of metabolic response in breast cancer patients receiving neoadjuvant chemotherapy. BMC Cancer. 2012;12:39.

20.   Cao MD, Sitter B, Bathen TF, Bofin A, Lonning PE, Lundgren S, et al. Predicting long-term survival and treatment response in breast cancer patients receiving neoadjuvant chemotherapy by MR metabolic profiling. NMR Biomed. 2012;25(2):369–78.

21.   Klomp DWJ, Bank BL Van De, Raaijmakers A, Korteweg MA, Possanzini C, Boer VO, et al. 31P MRSI and 1H MRS at 7T : initial results in human breast cancer. NMR Biomed. 2011;24:1337–42.

22.   Wijnen JP, van der Kemp WJM, Luttje MP, Korteweg MA, Luijten PR, Klomp DWJ. Quantitative 31 P Magnetic Resonance Spectroscopy of the Human Breast at 7 T. 2012;348:339–48.

23.   van der Kemp WJM, Boer VO, Luijten PR, Stehouwer BL, Veldhuis WB, Klomp DWJ. Adiabatic multi-echo ^{31}P spectroscopic imaging (AMESING) at 7 T for the measurement of transverse relaxation times and regaining of sensitivity in tissues with short T2* values. NMR Biomed. 2013;26(April):1299–307.

24.   Kemp WJM Van Der, Stehouwer BL, Luijten PR, Bosch MAAJ Van Den, Klomp DWJ, Den MAAJ Van, et al. Detection of alterations in membrane metabolism during neoadjuvant chemotherapy in patients with breast cancer using phosphorus magnetic resonance spectroscopy at 7 Tesla. Springerplus. 2014;3(1):634.

25.   Ogston KN, Miller ID, Payne S, Hutcheon AW, Sarkar TK, Smith I, et al. A new histological grading system to assess response of breast cancers to primary chemotherapy : prognostic significance and survival. Breast. 2003;12:320–7.

26.   Pathmanathan N, Balleine RL. Ki67 and proliferation in breast cancer. J Clin Pathol. 2013;66(6):512–6.

27.   Bustreo S, Osella-Abate S, Cassoni P, Donadio M, Airoldi M, Pedani F, et al. Optimal Ki67 cut-off for luminal breast cancer prognostic evaluation: a large case series study with a long-term follow-up. Breast Cancer Res Treat. 2016;157(2):363–71.

28.   Dowsett M, Nielsen TO, A'Hern R, Bartlett J, Coombes RC, Cuzick J, et al. Assessment of Ki67 in Breast Cancer: Recommendations from the international Ki67 in breast cancer working group. J Natl Cancer Inst. 2011;103(22):1656–64.

29.   Molino A, Micciolo R, Turazza M, Bonetti F, Piubello Q, Bonetti A, et al. Ki-67 immunostaining in

322 primary breast cancers: Associations with clinical and pathological variables and prognosis. Int J Cancer. 1997;74(4):433–7.

30. Hancu I, Govenkar A, Lenkinski RE, Lee SK. On shimming approaches in 3T breast MRI. Magn Reson Med. 2013;69(3):862–7.

31. Vanhamme L, Van Den Boogaart A, Huffel S Van. Improved Method for Accurate and Efficient Quantification of MRS Data with Use of Prior Knowledge. J Magn Reson. 1997;129:35–43.

32. Stehouwer BL, Kemp WJM Van Der, Luijten PR, Veldhuis WB, Wijnen JP, Klomp DWJ. 31P magnetic resonance spectroscopy of the breast and the influence of the menstrual cycle. Breast Cancer Res Treat. 2014;144:583–9.

33. Smith SR, Martin PA, Davies JM, Edwards RHTT, Stevens AN. The assessment of treatment response in non-Hodgkin's lymphoma by image guided 31P magnetic resonance spectroscopy. Br J Cancer. 1990;61(3):485–90.

34. Naruse S, Hirakawa K, Horikawa Y, Tanaka C, Higuchi T, Ueda S, et al. Measurements of in vivo 31P nuclear magnetic resonance spectra in neuroectodermal tumors for the evaluation of the effects of chemotherapy. Cancer Res. 1985;45(6):2429–33.

35. Abdel Razek AAK, Poptani H. MR spectrsocopy of head and neck cancer. Eur J Radiol [Internet]. 2013;82(6):982–9. Available from: http://dx.doi.org/10.1016/j.ejrad.2013.01.025

36. Kettelhack C, Wickede M V., Vogl T, Schneider U, Hohenberger P. Phosphorus-magnetic resonance spectroscopy to assess histologic tumor response noninvasively after isolated limb perfusion for soft tissue tumors. Cancer. 2002;94(5):1557–64.

37. Iorio E, Caramujo MJ, Cecchetti S, Francesca S, Carpinelli G, Canese R, et al. Key Players in Choline Metabolic Reprograming in Triple-negative Breast Cancer. Front Oncol. 2016;6(September):1–8.

38. Gulani V, Calamante F, Shellock FG, Kanal E, Reeder SB. Gadolinium deposition in the brain: summary of evidence and recommendations. Lancet Neurol. 2017;16(7):564–70.

39. Sakurai H, Mitsuhashi N, Murata O, Kitamoto Y, Saito Y, Hasegawa M, et al. Early radiation effects in highly apoptotic murine lymphoma xenografts monitored by 31P magnetic resonance spectroscopy. Int J Radiat Oncol Biol Phys. 1998;41(5):1157–62.

40. Dixon RM. NMR studies of phospholipid metabolism in hepatic lymphoma. NMR Biomed. 1998;11:370–9.

41. Kemp WJM Van Der, Boer VO, Luijten PR, Wijnen JP, Klomp DWJ. Increase in SNR for 31P MR Spectroscopy by Combining Polarization Transfer with a Direct Detection Sequence. Magn Reson Med. 2012;68:353–7.

42. Valkovič L, Dragonu I, Almujayyaz S, Batzakis A, Young LAJ, Purvis LAB, et al. Using a whole-body 31P birdcage transmit coil and 16-element receive array for human cardiac metabolic imaging at 7T. PLoS One. 2017;12(10):e0187153.

43. Löring J, van der Kemp WJM, Almujayyaz S, van Oorschot JWM, Luijten PR, Klomp DWJ. Whole-body radiofrequency coil for 31P MRSI at 7T. NMR Biomed. 2016;29(6):709–20.

2

Amide chemical exchange saturation transfer at 7 T: A possible biomarker for detecting early response to neoadjuvant chemotherapy in breast cancer patients.

Erwin Krikken
Vitaliy Khlebnikov
Moritz Zaiss
Rajni A. Jibodh
Paul J. van Diest
Peter R. Luijten
Dennis W.J. Klomp
Hanneke W.M. van Laarhoven
Jannie P. Wijnen

3

Abstract

Purpose: The purpose of this work was to investigate non-invasive early detection of treatment response of breast cancer patients to neoadjuvant chemotherapy (NAC) using chemical exchange saturation transfer (CEST) measurements sensitive to amide proton transfer (APT) at 7 tesla.

Methods: CEST images were acquired in 10 tumors of nine breast cancer patients treated with NAC. APT signals in the tumor, before and after the first cycle of NAC, were quantified using a three-pool Lorentzian fit of the z-spectra in the region of interest. The changes in APT were subsequently related to pathological response after surgery defined by the Miller-Payne system.

Results: Significant differences ($P < 0.05$, unpaired Mann-Whitney test) were found in the APT signal before and after the first cycle of NAC in 6 out of 10 lesions, of which two showed a pathological complete response. Of the remaining 4 lesions, one showed a pathological complete response. No significant difference in changes of APT signal were found between the different pathological responses to NAC treatment ($P > 0.05$, Kruskal-Wallis test).

Conclusions: This preliminary study shows the feasibility of using APT CEST MRI as a non-invasive biomarker to assess the effect of neoadjuvant chemotherapy in an early stage of NAC treatment of breast cancer patients.

Keywords: 7T MRI; APT CEST; NAC treatment; breast cancer; response prediction

Introduction

Neoadjuvant chemotherapy (NAC) is a systemic therapy that downstages cancer, enabling breast conserving surgery and reducing axillary treatment (1–4). Unfortunately, patients undergoing NAC may experience severe side effects, and in ~20% of patients treatment does not result in tumor size reduction (5,6). To spare patients from ineffective treatment, it would be beneficial to predict the pathological response early on in the course of treatment, allowing adjustments for patient-specific therapy.

Currently, the effect of NAC is generally evaluated based on change in the size of the tumor. Since underlying tumor changes in response to treatment usually precede a relatively slow process of change in tumor size (7–9), we set out to investigate metabolic properties of breast cancers that are expected to reveal changes early in the course of treatment.

Image contrast in standard clinical MRI is based on the concentration of water protons and T_2- and T_1-weighted imaging reveal anatomical information of different tissues. A recently developed MRI method, chemical exchange saturation transfer (CEST), allows detection of interactions between metabolites and water in the body (10,11).

Amide proton transfer (APT) CEST MRI detects the transfer of magnetization of labelled amide protons (resonating at 3.5 ppm downfield from the water) (12) and is sensitive to cellular mobile protein content as well as tissue pH. NAC treatment may cause an effect on these properties, therefore we expect to observe changes in APT early in the course of treatment which can be predictive of the pathological response. Dula et al. also assessed the reproducibility of APT imaging in breast cancer patients at 3 tesla (3 T) and showed group changes in APT during NAC, suggesting it may predict treatment response. Going to higher field strength (7 tesla; 7 T) will improve the signal to noise ratio (SNR) and contrast to noise ratio (CNR), improving sensitivity of APT signals to therapeutic response (13). Furthermore, endogenous T_1 relaxation times become longer with increasing field strength, resulting in an increase in CEST signals (14–17).

A few studies have shown reproducible methods which maximize the SNR for APT CEST MRI in the breast at 7 T. They measured the APT effect with a standard deviation of 1% in healthy glandular tissue (13,18). Assuming approximately the same standard deviation in tumor tissue, in this preliminary study we set out to investigate the possibility of using personalized APT MRI at 7 T to evaluate the effect of NAC treatment in a cohort of nine breast cancer patients.

3

Methods

Subjects

This MRI study was performed in accordance with the guidelines of the UMC Utrecht ethics committee and was part of a larger study. Nine breast cancer patients with a total of 10 lesions gave informed consent to participate in this study. The patients were selected for being treated with NAC, and were examined with APT CEST MRI before (pre) and after (post) the first cycle of NAC (at ~3 week intervals). Table 1 summarizes the demographics and tumor characteristics.

Table 1 Patient demographics and tumor characteristics

Patient	Age (years)	Treatment regimes	ER	PR	HER2 neu	Diameter (mm)[1]	TNM stage
1	61	4xAC-12xpaclitaxel	+	-	+	24	T2N1M0
2	50	3xFEC-3xdocetaxel	+	+	-	30	T4N1M0
3R	57	3xFEC-3xdocetaxel	+	+	-	35	T2N0M0
3L	57	3xFEC-3xdocetaxel	+	+	-	15	T1N0M0
4	43	3xFEC-3xdocetaxel	+	-	-	24	T2N0M0
5	59	3xFEC-3xdocetaxel	+	+	-	32	T2N1M0
6	39	3xFEC-3xdocetaxel	+	-	-	110	T3N2M0
7	55	6xTaxotere-AC	-	-	-	32	T2N0Mx
8	63	6x Taxotere-AC	+	+	-	15	T2N1Mx
9	35	6x Taxotere-AC	-	-	-	30	T2N0M0

AC adriamycin and cyclophosphamide, *ER* estrogen receptor, *FEC* 5-fluorouracil, epirubicin, and cyclophosphamide, *HER2* human epidermal growth factor receptor 2, *L* left, *PR* progesterone receptor, *R* right, *TNM* tumor, nodes, metastasis (classification of malignant tumors)
[1]Measurement performed on 3 T MRI acquired for standard clinical practice.

Acquisition

All patients were scanned in a prone position on a 7 T MR system (Philips, Cleveland, OH, USA). Six patients were scanned with a 26-channel bilateral breast ^{1}H transceiver coil (MR Coils, Zaltbommel, The Netherlands) (19) and three patients were scanned with a 2-channel unilateral ^{1}H/^{31}P dual-tuned transceiver coil (MR Coils, Zaltbommel, The Netherlands) (20). Two setups were used due to the fact the study was multicentre

and the RF coil was different in the two facilities. Third order image based B_0 shimming was performed with least square error optimization using a 3D B_0 map followed by manual segmentation of the breasts (21).

CEST-MRI was performed using a series of 20 sinc-Gauss radiofrequency (RF) pulses (pulse duration: 100 msec; inter pulse delay: 100 msec; the peak amplitude $B_{1 \approx}$ 2 µT) resulting in a 4 s saturation train (50% duty cycle) followed by a gradient-echo readout (22). Image acquisition included fat suppression with a short 1-2-1 spectral-spatial RF pulse to allow for a short TE of 1.4 msec, a TR of 2.6 msec and a flip angle of 1.2°. A coronal field of view (FOV) of 150x320x100 mm^3 (FHxRLxAP) with a true resolution of 2.3x3.0x6.8 mm^3 was obtained in 2 shots with an interval of 4.48 sec and a 4-fold acceleration in right-left direction. 33 frequency offsets were acquired resulting in a scan time of 4 min 55 sec. These offsets were not equally distributed over the frequencies; more offsets were obtained around the amide peak (3.5 ppm) and the water peak (0.0 ppm) for better fitting of these resonances. The frequency offsets associated with the nuclear Overhauser effect (NOE) were not included due to signal distortions by unsuppressed lipid resonances.

In the same MRI session, the last acquired scan was a dynamic contrast enhanced (DCE) series. The first high-resolution scan after contrast administration was used to aid in delineating the tumor on the CEST images. The dynamic series consisted of 18 consecutive 3D T_1-weighted gradient echo sequences, starting with a fat suppressed high resolution scan prior to the contrast injection of 0.1 mmol/kg gadobutrol (Bayer Schering Pharma AG, Berlin, Germany), followed by 12 high temporal resolution scans (TE = 1.6 msec, TR = 4.8 msec, flip angle = 8 °, FOV = 160 x 350 x 160 mm^3, resolution = 2.86 x 2.86 x 2.86 mm^3) to finish with another 5 fat suppressed high resolution scans (TE = 2.5 msec, TR = 5.6 msec, flip angle = 8 °, FOV = 160 x 350 x 160 mm^3, resolution = 0.7 x 0.7 x 0.7 mm^3).

Data analysis

Image processing and data analysis were performed with MATLAB 2014b (MathWorks, Natick, MA, USA). CEST images were B_0 corrected using the WASSR method (23). A region of interest (ROI) was drawn in the whole tumor using the MR image of the last offset (33.6 ppm) of the CEST series before and after the first NAC. The procedure for selecting the ROI in the tumor can be seen in the upper part of Figure 1 for one single slice. Figure 1a shows the DCE images which were used to aid in selecting the tumor

region. The S_0 image acquired at 33.6 ppm presented in Figure 1b was used to draw the ROI in the tumor (green circle). To obtain a mean APT signal in the whole tumor this procedure is performed for all the slices containing the tumor. The mean APT signal in the ROI, as a function of the frequency (z-spectra) was fitted with a three-pool Lorentzian model (water, APT and magnetization transfer (MT)) using the Levenberg-Marquardt algorithm; see Table 2 for fit parameters (15,24).

$$\frac{M_z(\Delta\omega)}{M_z^0(\Delta\omega)} = Z(\Delta\omega) = Z_{base} - \sum_i L_i(\Delta\omega)$$

with

$$L_i(\Delta\omega) = A_i \frac{\Gamma_i^2/4}{\Gamma_i^2/4 + (\Delta\omega - \delta_i)^2}$$

Each Lorentzian function L_i of effect i is defined for the offset frequency $\Delta\omega$ by amplitude A_i, full width at half maximum Γ_i, and displacement from the frequency of free water protons δ_i. The parameter Z_{base} corrects for constant signal reduction. The calculated APT map was obtained using the amplitude of the fit of the APT signal. To facilitate the comparison of different lesions in terms of APT signal change following the first NAC cycle, the mean APT signal pre NAC was normalized to 1. The whole tumor analysis was compared to a single-slice approach containing the largest diameter of the tumor.

Table 2 Starting points and boundaries of all fit parameters of the three-pool Lorentzian fit

	Start	Lower	Upper
Z_{base}	0.5	0.5	1
A_{water}	0.8	0	1
Γ_{water}	1	0.1	2.5
δ_{water}	0	-1	1
A_{MT}	0.1	0	1
Γ_{MT}	5	3	100
δ_{MT}	0	-0.5	0.5
A_{amide}	0.1	0	1
Γ_{amide}	1	1	1.5
δ_{amide}	3.5	3.3	3.7

The chemical shift δ and FWHM Γ are given in ppm.
Γ FWHM, δ chemical shift, *MT* Magnetization Transfer

Pathology

The pathological responses to NAC are defined according to the Miller-Payne system (25); complete response is classified as grade 5 and non-response as grade 1. Pathological non-response indicates no change or some alteration to individual malignant cells, but no reduction in overall cellularity compared to pre-therapy core biopsy. Grades 1 and 2 we grouped together as non-responders, grades 3 and 4 as partial responders and grade 5 as complete responders.

Statistical analysis

Statistical analysis was performed using an unpaired Mann-Whitney test (GraphPad Prism, GraphPad Software, San Diego, CA, USA), with a two-tailed distribution to show statistical difference ($\alpha = 0.05$) between the APT signal pre NAC and after the first cycle of NAC.

A Kruskal Wallis test with a post-hoc Dunn's multiple comparison test was used to assess statistical difference in APT signal between the groups with different pathological responses (non-responders, partial responders and complete responders).
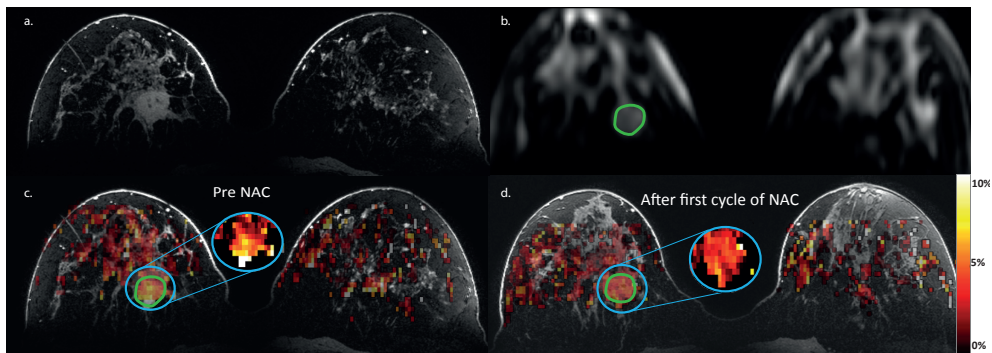
Figure 1 MR imaging data set from a patient 1 (Table 1). **A)** The last image of the DCE series was used to aid in drawing the region of interest (ROI) in the tumor. **B)** S_0 image (acquired at 33.6 ppm) was used to draw the tumor ROI (green circle) before applying this on the APT map. **C)** Calculated APT map on top of the DCE image from the dataset before the patient started with neoadjuvant chemotherapy treatment. **D)** Calculated APT map after the first cycle of neoadjuvant chemotherapy treatment. The blue circles indicate the insert of the tumor region for better viewing of the underlying APT map. Color bar = percentage of APT effect.

Results

Data analysis

Figure 1c and 1d present calculated color APT maps manually overlaid on the image of the DCE series before (Figure 1c) and after (Figure 1d) the first cycle of NAC treatment. Within this tumor a reduced amide signal of 21% in the APT map was observed after the first cycle of NAC.
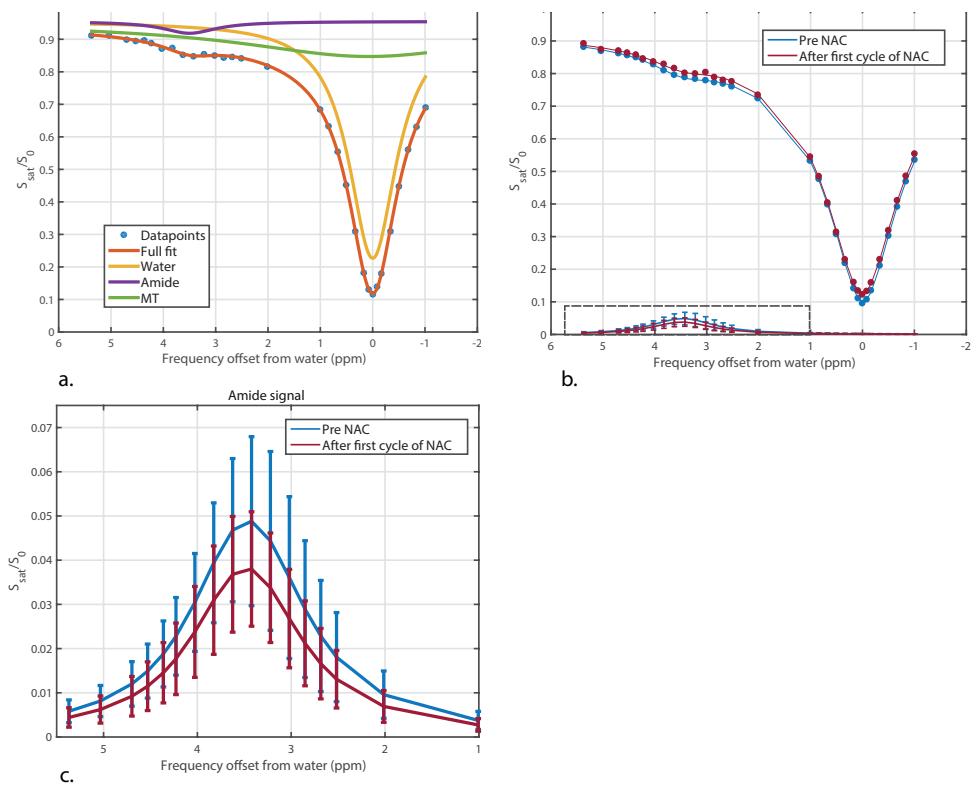
Figure 2 Results of the CEST analysis in the same patient as in Figure 1 in the tumor ROI (Table 1, patient 1). **A)** Results of the three pool Lorentzian fitting of the Z-spectrum of water (yellow line), magnetization transfer effect (MT; green line),amide proton transfer (APT; purple line) and the full fit consisting of the three fits (orange). **B)** Mean Z-spectrum in the tumor before (blue) and after (red) the first cycle of neoadjuvant chemotherapy treatment. The insert of the dashed box is shown in **(C)**, which shows the Lorentzian fit for the APT signal before (blue) and after (red) neoadjuvant chemotherapy treatment with the standard deviation of the APT signal of the voxels in the tumor ROIs, shown as the error bars.

An exemplary three pool Lorentzian fit is depicted in Figure 2a. The acquired data points from the tumor ROI (green circle in Figure 1c) are shown as blue dots representing the Z-spectrum magnitude at the 32 frequency offsets, the water fit as a yellow line, the MT fit as a green line, the APT fit as a purple line and the full fit consisting of the three fits in orange. Figure 2b shows the corresponding Z-spectrum within the tumor before (blue line) and after the first cycle of NAC treatment (red line) based on the 32 frequency offsets from the same case as in Figure 1. Figure 2c is the insert of the dashed box in Figure 2b, presenting the Lorentzian fit for the APT signal before (blue) and after (red) NAC treatment. The 21% decrease in APT signal after the first cycle of NAC treatment can be observed.

Table 3 Mean APT signal in the tumor before and after the first cycle of neoadjuvant chemotherapy

Patient	Patho-logical response	Mean (±SD) APT signal before NAC	Mean (±SD) APT signal after the first cycle of NAC	Delta mean APT signal	P value[a]
1	5	0.0494 (±0.0062)	0.0388 (±0.0046)	-0.0106	< 0.0001*
2	3	0.0319 (±0.0046)	0.0311 (±0.0056)	-0.0008	0.0458*
3R	4	0.0289 (±0.0055)	0.0231 (±0.0046)	-0.0058	0.0004*
3L	4	0.0189 (±0.0020)	0.0149 (±0.0034)	-0.0040	0.0003*
4	5	0.0420 (±0.0098)	0.0275 (±0.0043)	-0.0145	< 0.0001*
5	2	0.0132 (±0.0037)	0.0140 (±0.0040)	+0.0008	0.5749
6	4	0.0272 (±0.0049)	0.0229 (±0.0053)	-0.0043	0.4135
7	5	0.0254 (±0.0056)	0.0252 (±0.0043)	-0.0002	0.5259
8	3	0.0319 (±0.0068)	0.0326 (±0.0054)	+0.0007	0.4170
9	2	0.0381 (±0.0045)	0.0465 (±0.0072)	+0.0084	0.0001*

[a] Unpaired Mann-Whitney test with two-tailed distribution
* Significant difference

The mean and standard deviation of the APT signal inside the tumor before and after the first cycle of NAC for all the ten lesions together with the pathological response are shown in Table 3. The asterisk indicates a significant difference comparing the APT signal before and after the first cycle of NAC treatment of each patient. Table 3 is visualized in Figure 3 where the non-responders are shown in red, the partial responders in blue and the complete responders in green. The dashed lines indicate the absence of a change in APT signal before and after the first cycle of NAC treatment.

Normalized changes in APT signal after the first cycle of chemotherapy with pre-NAC APT signal normalized to 1 for all the tumors can be observed in Figure 4. The one slice approach (slice with largest tumor diameter; Figure 4a) was compared to the change in APT signal in the whole tumor (Figure 4b). A distinction between the mean of the non-responders (bright red line), the mean of the partial responders (bright blue line) and the mean of the complete responders (bright green line) is visible. Each blurred line in the backgrounds represents a different patient and the standard deviation in each group is shown as error bars. Note that the distinction between the partial responders and complete responders in the single-slice approach is clearer than in the change of APT signal in the whole tumor.
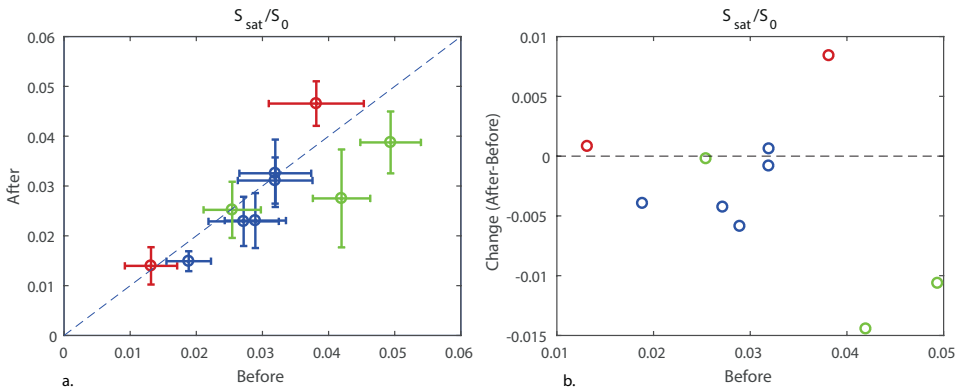

Figure 3 Mean APT signal and standard deviation within the ROI (tumor) for all ten lesions. **A)** The mean APT signal after the first cycle of NAC is plotted versus the mean APT signal before the start of NAC for the non-responders (red), partial responders (blue) and complete responders (green). **B)** The mean change in APT signal is plotted versus the mean APT signal before NAC. The dashed lines in both a and b indicate the absence of a change in APT signal before and after the first cycle of NAC treatment.

Statistical analysis

Based on the 3D whole tumor analysis, six out of the ten lesions showed a significant change in APT signal in the tumor, where two out of three complete responders (patients 1 and 4) showed a significant difference ($P < 0.0001$ for both patients; Table 3). The third complete responder, patient 7, showed no significant difference ($P = 0.5259$). Of the partial responders, three lesions (patient 2, 3R and 3L) also showed a significant difference in APT signal ($P = 0.0458$, $P = 0.0004$ and $P = 0.0003$), whereas the other partial responders (patient 6 and 8) showed no significant differences, with $P = 0.4135$ and $P = 0.4170$, respectively. One non-responder showed a significant difference

(patient 9, P < 0.0001) while the other non-responder showed no statistical difference between the APT signal before and after the first cycle of NAC (P = 0.5749). However, note that both non-responders showed an increase in APT signal while the other responders (patient 8 as an exception) showed a decrease in APT signal, suggesting that the non-responders can be differentiated quite well from the responders based on the direction of the change in APT signal.

The Kruskal-Wallis test with the post-hoc Dunn's multiple comparison test revealed no significant difference in the change of APT signal after the first cycle of NAC (P = 0.1057) between the three different pathological responses.
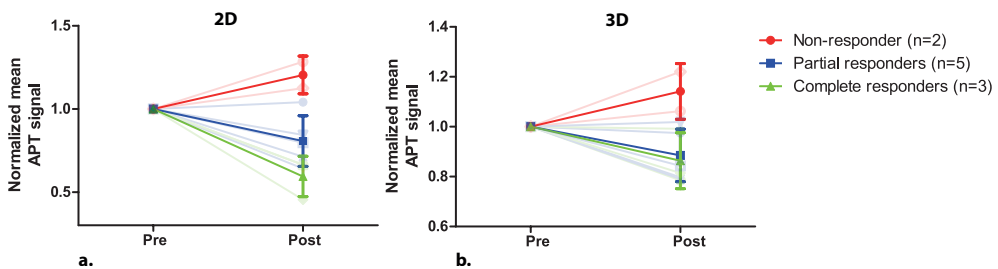

Figure 4 Normalized changes in APT signal after the first cycle of neoadjuvant chemotherapy in the slice with the largest tumor diameter **(a)** and in the whole tumor **(b)**. The mean of the non-responders (bright red line), partial responders (bright blue line) and complete responders (bright green line) on top of the change in APT signal of all the lesions (transparent lines in the background), where each line represents a different lesion. The standard deviation in each group is shown as error bars.

Discussion

In this preliminary study, the potential for using CEST at 7 T to monitor treatment effects in breast cancer was evaluated. We demonstrated that amide CEST signals can be measured in breast cancer before and after the first cycle of NAC. Significant differences in the APT CEST MRI signal were observed (P < 0.05) in six out of ten breast tumors. As to the direction of the change in APT signal, the non-responders (patients 5 and 9) showed an increase in APT signal whereas the other patients (except patient 8) showed a decrease in APT signal. A larger patient population is required for a more comprehensive analysis of change in APT signal in relation to pathological response.

Animal studies (26) demonstrated increased APT effects in tumor compared to healthy tissue, and Salhotra et al. attributed this effect to increased cellular proliferation and subsequent accumulation of defective proteins (27). In breast tumors, Dula et al. (28) observed changes in APT signal and attributed this to changes in the concentration

of proteins and peptides or in the amide proton exchange rates, influenced by a change in pH, and perhaps T_1 (12,29–33) due to therapy effects. Remarkably, the non-responders in this preliminary study showed an increase in APT signal after the first cycle of NAC, which possibly hints to a continuing increase in the concentrations of proteins and peptides because the tumor was not affected by the NAC treatment. However, the increase in APT signal in the tumor is likely related to a combination of all abovementioned effects. Assuming these processes occur at the core of the tumor, the largest expected change in APT signal would be at that location. This could explain the larger APT increase observed in the single-slice (with largest tumor diameter) analysis compared to the 3D whole tumor volume analysis. (Figure 4). As for the single-slice approach, the core contributes relatively more to the APT signal resulting in a larger mean change in APT signal compared to the mean change in APT signal of the whole tumor. It also seems that in the single-slice approach the distinction between the partial responders and the complete responders becomes more clear, hinting to a more linear distribution of change in APT signal for the three response groups. Further research needs to be performed to examine if the single-slice approach results in a better distinction between the different response groups. Although a single-slice approach could save scan time or allows for more frequency offsets in the same scan time, caution is needed as it may be prone to unwanted inter-institutional variations due to differences in slice selection.

Though patient 7 was a complete responder, the tumor APT signal change (Figure 3) was located in the middle of the partial responders (blue), suggesting the same change in APT signal as the partial responders. Interestingly, this was the only triple negative tumor from the three complete responders. Triple negative tumors feature a unique microenvironment distinct from that of other subtypes (34,35) possibly explaining the different APT signal in this type of tumor, however this observation remains to be confirmed.

Due to the small sample size (n=10) we did not correct for age and menstrual cycle effects, which are known to affect the breast density. Particularly the water content of the breast parenchyma changes during the menstrual cycle (36), possibly influencing the CEST effect (15,16). Additionally, all patients in this study received NAC treatment which is known to influence the menstrual cycle.

The overall calculated APT contrast can also be influenced by the degree of fat suppression. We used RF and gradient spoiling to reduce lipid artefacts. However,

insufficient fat suppression in the tumor may have resulted in an underestimation of the CEST amplitude (37) possibly affecting the change in APT signal.

CEST MRI is sensitive to the B_1^+ field, since different exchanging groups are affected by the B_1^+. Variation in B_1^+ may cause more contrast from slower (or faster) exchanging species. We were interested in APT CEST MRI signal generated by the slow exchanging amide protons and the optimal B_1^+ for detecting this exchange is approximately 1 µT (38). The peak B_1 amplitude in this study was set to 2 µT to account for B_1 loss due to the hardware setup. The unilateral setup consisted of a quadrature RF coil placed in front of the breast, while the bilateral setup was an exact copy of this coil, only for both breasts. This setup lead to a decrease in B_1 varying from 60% in the front of the breast to 50% towards the pectoralis major. The sequence was optimized to achieve an acquired B_1 of approximately 1 µT throughout the breast. Therefore, the location of the tumor can possibly influence the measured change in APT CEST signal. In this study we assumed that the location of the tumor was the same between the two measurements receiving the same amount of B_1 and therefore not influencing the measured change in APT CEST signal. Several B_1^+ inhomogeneity correction methods have been proposed (24,39,40) to improve the CEST images. These methods however require an accurate B_1 map or acquisition at multiple B_1 amplitudes. Due to limited scan time this was unfortunately not possible in this study. Another solution to deal with B_1 inhomogeneity would be a new design for the coil setup at 7 T where a homogeneous B_1 field can be achieved. For example, the use of dipole antennas have shown to be able to achieve this in body imaging (41). These methods for improving the B_1 field could be good options for future studies to further improve the quality of the APT maps of the breast.

It would be interesting to translate these findings to the clinical field strength of 3 T. Klomp et al. (13) however, compared APT CEST MRI at 3 T to 7 T and found that the variance of noise in measurements at 3 T was large (i.e. approximately 5% of CEST effects when compared to the water signal; larger than the alterations in CEST effects we have observed in our study), thereby limiting the ability to discern subtle changes during, for example, first-line therapy. At 7 T, however, the increased SNR and increased spectral resolution enabled a fourfold reduction in the noise in of the observed APT CEST compared to 3 T. Due to the inherently small CEST signal, changes within these CEST effects seem challenging to detect at 3 T at the moment. Fortunately, 7 T has been FDA approved and thereby will likely become available to more hospitals.

3

Predictive biomarkers are critical for evaluation of the neoadjuvant therapies, as well as the effect of novel targeted agents intended to be incorporated into neoadjuvant therapy (42). The potential for high-field-strength CEST MR imaging of the breast as a biomarker for evaluation of NAC response is promising, as is the capability to noninvasively detect changes in protein and peptide levels. These may play a key role in understanding breast tumor progression and response to treatment (18).

Conclusions

In a small group of breast cancer patients, this preliminary study shows the feasibility of using APT CEST MRI at 7 T as a non-invasive biomarker to predict the effect of neoadjuvant chemotherapy in an early stage of treatment. This can be useful in personalized breast cancer treatment planning.

References

1.   Loibl S, Minckwitz G Von, Blohmer J, Costa SD, Gerber B, Eidtmann H, et al. Surgical Procedures After Neoadjuvant Chemotherapy in Operable Breast Cancer : Results of the GEPARDUO Trial. Ann Surg Oncol. 2006;13(11):1434–42.

2.   Kaufmann M, Hortobagyi GN, Goldhirsch A, Scholl S, Makris A, Valagussa P, et al. Recommendations From an International Expert Panel on the Use of Neoadjuvant (Primary) Systemic Treatment of Operable Breast Cancer : An Update. J Clin Oncol. 2006;24(12):1940–9.

3.   Kaufmann M, Minckwitz G Von, Bear HD, Buzdar A, Mcgale P, Bonnefoi H, et al. Recommendations from an international expert panel on the use of neoadjuvant (primary) systemic treatment of operable breast cancer : new perspectives 2006. Ann Oncol. 2007;18(11):1927–34.

4.   Kaufmann M, Minckwitz G Von, Mamounas EP, Cameron D, Carey LA, Cristofanilli M, et al. Recommendations from an International Consensus Conference on the Current Status and Future of Neoadjuvant Systemic Therapy in Primary Breast Cancer. Ann Surg Oncol. 2011;19:1508–16.

5.   Fisher B, Brown A, Mamounas E, Wieand S, Robidoux A, Margolese RG, et al. Effect of preoperative chemotherapy on local-regional disease in women with operable breast cancer: findings from National Surgical Adjuvant Breast and Bowel Project B-18. J Clin Oncol. 1997;15(7):2483–93.

6.   Bonadonna G, Valagussa P, Zucali R, Salvadori B. Primary Chemotherapy in Surgically Resectable Breast Cancer. CA Cancer J Clin. 1995;45(4):227–43.

7.   Tudorica A, Oh KY, Chui SYC, Roy N, Troxell ML, Naik A, et al. Early prediction and evaluation of breast cancer response to neoadjuvant chemotherapy using quantitative DCE-MRI. Transl Oncol. 2016;9(1):8–17.

8.   Harry VN, Semple SI, Parkin DE, Gilbert FJ. Use of new imaging techniques to predict tumour response to therapy. Lancet Oncol. 2010;11(1):92–102.

9.   Padhani AR, Miles KA. Multiparametric Imaging of Tumor Response to Therapy. Radiology. 2010;256(2):348–64.

10.   Wolff SD, Balaban RS. NMR imaging of labile proton exchange. J Magn Reson. 1990;86(1):164–9.

11.   Van Zijl PCM, Zhou J, Mori N, Payen JF, Wilson D, Mori S. Mechanism of magnetization transfer

during on-resonance water saturation. A new approach to detect mobile proteins, peptides, and lipids. Magn Reson Med. 2003;49(3):440–9.

12. Zhou JY, Lal B, Wilson D a., Laterra J, Van Zijl PCM. Amide Proton Transfer (APT) Contrast for Imaging of Brain Tumors. Magn Reson Med. 2003;50(6):1120–6.

13. Klomp DWJ, Dula AN, Arlinghaus LR, Italiaander M, Dortch RD, Zu Z, et al. Amide proton transfer imaging of the human breast at 7T: development and reproducibility. NMR Biomed. 2013 Oct;26(10):1271–7.

14. Zaiss M, Windschuh J, Paech D, Meissner JE, Burth S, Schmitt B, et al. Relaxation-compensated CEST-MRI of the human brain at 7T: Unbiased insight into NOE and amide signal changes in human glioblastoma. Neuroimage. 2015;112:180–8.

15. Zaiss M, Xu J, Goerke S, Khan IS, Singer RJ, Gore JC, et al. Inverse Z -spectrum analysis for spillover-, MT-, and T 1 -corrected steady-state pulsed CEST-MRI - application to pH-weighted MRI of acute stroke. NMR Biomed. 2014;27(3):240–52.

16. Khlebnikov V, Polders D, Hendrikse J, Robe PA, Voormolen EH, Luijten PR, et al. Amide Proton Transfer (APT) Imaging of Brain Tumors at 7 T : The Role of Tissue Water T1 -Relaxation Properties. Magn Reson Imaging. 2017;77:1525–32.

17. Khlebnikov V, Siero JCW, Wijnen J, Visser F, Luijten PR, Klomp DWJ, et al. Is there any difference in Amide and NOE CEST effects between white and gray matter at 7 T? J Magn Reson. 2016;272:82–6.

18. Dula AN, Dewey BE, Arlinghaus LR, Williams JM, Klomp D, Yankeelov TE, et al. Optimization of 7-T Chemical Exchange Saturation Transfer Parameters for Validation of Glycosaminoglycan and Amide Proton Transfer of Fibroglandular Breast Tissue. Radiology. 2014;275(1):255–61.

19. Van Der Velden T a., Italiaander M, Van Der Kemp WJM, Raaijmakers AJE, Schmitz a. MMTT, Luijten PR, et al. Radiofrequency configuration to facilitate bilateral breast 31P MR spectroscopic imaging and high-resolution MRI at 7 Tesla. Magn Reson Med. 2015;74(6):1803–10.

20. Klomp DWJ, van der Kemp WJM, Korteweg M, Wijnen JP, Bosch M Van De, Luijten PR. 31P MRS at 7T can be more sensitive and specific than 1 H MRS in monitoring breast cancer treatment . Proc Intl Soc Mag Reson Med. 2011;19:343.

21. Hancu I, Govenkar A, Lenkinski RE, Lee SK. On shimming approaches in 3T breast MRI. Magn Reson Med. 2013;69(3):862–7.

22. Khlebnikov V, Geades N, Klomp DWJ, Hoogduin H, Gowland P, Mougin O. Comparison of Pulsed Three-Dimensional CEST Acquisition Schemes at 7 Tesla : Steady State Versus Pseudosteady State. Magn Reson Med. 2016;00:2280–7.

23. Kim M, Gillen J, Landman BA, Zhou J, Van Zijl PCM. Water saturation shift referencing (WASSR) for chemical exchange saturation transfer (CEST) experiments. Magn Reson Med. 2009;61(6):1441–50.

24. Windschuh J, Zaiss M, Meissner J, Paech D, Radbruch A, Ladd ME, et al. Correction of B 1-inhomogeneities for relaxation-compensated CEST imaging at 7T. NMR Biomed. 2015;28:529–37.

25. Ogston KN, Miller ID, Payne S, Hutcheon AW, Sarkar TK, Smith I, et al. A new histological grading system to assess response of breast cancers to primary chemotherapy : prognostic significance and survival. Breast. 2003;12:320–7.

26. Salhotra A, Lal B, Laterra J, Sun PZ, van Zijl PCM, Zhou J. Amide proton transfer imaging of 9L gliosarcoma and human glioblastoma xenografts. NMR Biomed. 2008;21:489–97.

27. Adams J. The proteasome: a suitable antineoplastic target. Nat Rev Cancer. 2004;4(5):349–60.

28. Dula AN, Arlinghaus LR, Dortch RD, Dewey BE, Whisenant JG, Ayers GD, et al. Amide proton

transfer imaging of the breast at 3 T: Establishing reproducibility and possible feasibility assessing chemotherapy response. Magn Reson Med. 2013;70:216–24.

29. Zhou J, Blakeley JO, Hua J, Kim M, Laterra J, Pomper MG, et al. Practical data acquisition method for human brain tumor amide proton transfer (APT) imaging. Magn Reson Med. 2008;60(4):842–9.

30. Zhou J, Tryggestad E, Wen Z, Lal B, Zhou T, Grossman R, et al. Differentiation between glioma and radiation necrosis using molecular magnetic resonance imaging of endogenous proteins and peptides. Nat Med. 2011;17(1):130–4.

31. Jones CK, Schlosser MJ, Van Zijl PCM, Pomper MG, Golay X, Zhou J. Amide proton transfer imaging of human brain tumors at 3T. Magn Reson Med. 2006;56(3):585–92.

32. Wen Z, Hu S, Huang F, Wang X, Guo L, Quan X, et al. NeuroImage MR imaging of high-grade brain tumors using endogenous protein and peptide-based contrast. Neuroimage. 2010;51(2):616–22.

33. Zhou J, Payen JF, Wilson DA, Traystman RJ, Van Zijl PCM. Using the amide proton signals of intracellular proteins and peptides to detect pH effects in MRI. Nat Med. 2003;9(8):1085–90.

34. Foulkes WD, Smith IE, Reis-Filho JS. Triple-Negative Breast Cancer. N Engl J Med. 2010;363:1938–48.

35. Yu T, Di G. Role of tumor microenvironment in triple-negative breast cancer and its prognostic significance. Chinese J Cancer Res. 2017;29(3):237–52.

36. Delille J, Slanetz PJ, Yeh ED, Kopans DB, Garrido L. Physiologic Changes in Breast Magnetic Resonance Imaging during the Menstrual Cycle : Perfusion Imaging , Signal Enhancement , and Influence of the T1 Relaxation Time of Breast Tissue. Breast J. 2005;11(4):236–41.

37. Zhang S, Keupp J, Wang X, Dimitrov I, Madhuranthakam AJ, Lenkinski RE, et al. Z-spectrum appearance and interpretation in the presence of fat: Influence of acquisition parameters. Magn Reson Med. 2017;00:1–7.

38. Zu Z, Li K, Janve VA, Does MD, Gochberg DF. Optimizing pulsed-chemical exchange saturation transfer imaging sequences. Magn Reson Med. 2011;66(4):1100–8.

39. Singh A, Cai K, Haris M, Hariharan H. On B1 Inhomogeneity Correction of In Vivo Human Brain Glutamate Chemical Exchange Saturation Transfer Contrast at 7T. Magn Reson Imaging. 2013;69:818–24.

40. Khlebnikov V, Windschuh J, Siero JCW, Zaiss M, Luijten PR, Klomp DWJ, et al. On the transmit field inhomogeneity correction of relaxation -compensated amide and NOE CEST effects at 7 T. NMR Biomed. 2017;30:e3687.

41. Raaijmakers AJE, Italiaander M, Voogt IJ, Luijten PR, Hoogduin JM, Klomp DWJ, et al. The fractionated dipole antenna: A new antenna for body imaging at 7 Tesla. Magn Reson Med. 2016;75(3):1366–74.

42. Rubovszky G, Horváth Z. Breast Cancer Recent Advances in the Neoadjuvant Treatment of Breast Cancer. J Breast Cancer. 2017;20(2):119–31.

3

Contradiction between amide-CEST signal and pH in breast cancer explained with metabolic MRI.

Erwin Krikken

Wybe J.M. van der Kemp

Vitaliy Khlebnikov

Thijs van Dalen

Maartje Los

Hanneke W.M. van Laarhoven

Peter R. Luijten

Maurice A.A.J. van den Bosch

Dennis W.J. Klomp

Jannie P. Wijnen

4

Abstract

Purpose: Metabolic MRI is a non-invasive technique which can give new insights in understanding cancer metabolism and finding biomarkers to evaluate or monitor treatment plans. Using this technique, a previous study has shown an increase in pH during neoadjuvant chemotherapy (NAC) treatment, while recent observation in a different study showed a reduced amide proton transfer (APT) signal during NAC treatment (negative relation). These findings are counterintuitive, given the known intrinsic positive relationship of APT signal to pH.

Methods: In this study we combined amide proton transfer (APT) MRI and ^{31}P-MRSI measurements, to unravel the relationship between the APT signal and pH in breast cancer. Twenty-two breast cancer patients were scanned with a 7 T MRI before and after the first cycle of NAC treatment. pH was determined by the chemical shift of inorganic phosphate (Pi).

Results: While APT signals have a positive relation to pH and amide content, we observed a direct negative linear correlation between APT signals and pH in breast tumors in vivo.

Conclusions: As differentiation of cancer stages was confirmed by observation of a linear correlation between cell proliferation marker PE/Pi (phosphoethanolamine over inorganic phosphate) and pH in the tumor, our data demonstrates that the concentration of mobile proteins likely supersedes the contribution of the exchange rate to the APT signal.

Keywords: 7 T MRI; APT CEST; 31P-MRSI; breast cancer

Introduction

Metabolism in cancer is widely investigated by the use of magnetic resonance imaging (MRI). Metabolic MRI is a non-invasive technique which can give new insights in understanding cancer metabolism and potentially provide biomarkers to evaluate or monitor treatment plans. Among the different techniques, a method based on chemical exchange saturation transfer (CEST) (1) has been of great interest lately (2–8). This MRI method is a powerful and sensitive technique in which low concentration solutes can be visualized through the water signal. The contrast depends on the exchange rate of saturated mobile protons to the bulk water resonance. This enables indirect imaging of endogenous molecules containing these mobile protons, such as amides (proteins and peptides) which is called amide proton transfer (APT). Several studies have explored the use of different CEST approaches for treatment monitoring in cancer patients such as chemotherapy (9–16), radiation therapy (17), oncolytic virus therapy (18), radiosurgery (19) and antibiotic treatment (20).

In theory (21), the measured amide signal is primarily related to the concentration of mobile amide protons, the exchange rate (dependent on pH), duration of saturation pulse, and T_1 relaxation of water. The chemical exchange rate of amide protons is base catalyzed (6). Therefore, an increase of pH results in an increase of the exchange rate and consequently causes an increase in APT signal.

All healthy cellular functioning highly depends on a strict acid-base balance (pH homeostasis). This delicate balance is influenced by many metabolic processes such as proton production, proton transportations, chemical buffering, and vascular removal of waste products. Malignant cells show a pronounced increase in metabolic processes resulting in excessive production of protons (22). To adapt to this intracellular acidity the number and function of proton-exporting mechanisms is increased (22). This adaptation keeps intracellular pH (pHi) at normal or slightly alkaline levels which favors protein synthesis and mitosis, while the extracellular pH (pHe) decreases due to the acidity from the exported protons (23). There are many potential pH regulators involved in this process including: Na+/HCO3 – co-transporters, Na+/H+ exchangers, monocarboxylate transporters, the vacuolar ATPase, carbonic anhydrase, anion exchangers, the Cl–/HCO3 – exchangers, and ATP synthase (24,25).

Phosphorous magnetic resonance spectroscopy (^{31}P-MRSI) provides a non-invasive technique to measure the pHi of tumor cells. The resonant frequency of inorganic

phosphate (Pi) is pH dependent (26) and in many tissues, the majority of the Pi resonance is intracellular (~85%) (27). As such, pHi can be measured by ^{31}P-MRSI by calculating the chemical shift difference between Pi and a pH-independent reference peak. Moreover, with ^{31}P-MRSI, cell proliferation biomarkers, the phoshomonoesters (PME) phosphoethanolamine (PE) and phosphocholine (PC) can be detected, providing a direct indication of cytotoxicity (28,29). Also, the phosphodiesters (PDE) glycerophosphocholine (GPC) and glycerophosphoethanolamine (GPE) can be measured. The PME/PDE ratio is related to mitotic count and therefore indirect to the tumor grade (30). This technique has been used in a previous study (31) to show the feasibility of monitoring membrane metabolism during NAC treatment. They also showed that the pH was increased with 0.19 units after the completion of NAC treatment. In another study (32), reduced APT signal during NAC treatment was observed. These findings are counterintuitive, if one interprets the data solely in terms of the pH dependence of the chemical exchange rate of amide protons, which is base catalysed. Therefore an increase in pH, results in an increased exchange rate, causing an increase in APT signal.

In this study, we have combined both APT-MRI and ^{31}P-MRSI in breast cancer patients, to better comprehend the relation between APT signal and pH. APT-MRI and ^{31}P-MRSI were acquired in breast cancer patients receiving NAC treatment before and after the first cycle of NAC using 7 T MRI.

Materials and methods

Subjects

This MRI study was performed in accordance with the guidelines of the UMC Utrecht ethics committee (trialregister.nl: NTR4980). Twenty-two breast cancer patients gave informed consent to participate in this study with a mean age of 49 years (range 36-64 years). The patients were selected for being treated with NAC, and were examined before and after the first cycle of NAC (at ~3 week intervals). Table 1 summarizes the demographics and tumor characteristics of these patients.

Acquisition

All patients were scanned in a prone position on a 7 T MR system (Philips, Best, The Netherlands). CEST was acquired using a 26-channel bilateral breast ^{1}H transceiver coil (MR Coils, Zaltbommel, The Netherlands) and the ^{31}P-MRSI with a home-built

2-channel unilateral ^{1}H/^{31}P dual-tuned transceiver coil. Therefore, the patient was repositioned between the two measurements. Third order image based B_0 shimming was performed with least square error optimization using a 3D B_0 map followed by manual segmentation of the breasts (33).

Table 1 Demographics, tumor characteristics and pathological response of breast cancer patients undergoing neoadjuvant chemotherapy.

Patient	Age (years)	Treatment regimes	ER	PR	HER2neu	TNM
1	58	4x AC – 4x docetaxel	+	-	+	T2N1M0
2	55	3x FEC – 3x docetaxel	+	+	-	T2N0M0
3	58	3x FEC – 3x docetaxel	+	+	-	T2N1M0
4	38	3x FEC – 3x docetaxel	+	-	-	T3N2M0
5	42	4x AC – 4x docetaxel	-	-	-	T2N0M0
6	38	4x AC – 12x paclitaxel	-	-	-	T2N3M0
7	36	4x AC – 4x docetaxel	+	+	-	T2N1M0
8	47	4x AC – 4x docetaxel	-	-	+	T2N0M0
9	42	4x AC – 4x docetaxel	-	-	+	T2N0M0
10	43	4x AC – 4x docetaxel	-	-	-	T2N0M0
11	40	4x AC – 12x paclitaxel	+	+	+	T1N0M0
12	41	4x AC – 12x paclitaxel	-	-	+	T2N1M0
13	55	4x AC – 12x paclitaxel	-	-	-	T2N0M0
14	53	4x AC – 12x paclitaxel	+	-	-	T2N1M0
15	45	4x AC – 12x paclitaxel	-	-	-	T2N1M0
16	48	4x AC – 12x paclitaxel	-	-	+	T2N0M0
17	53	6x Docetaxel - AC	-	-	-	T2N0M0
18	61	6x Docetaxel - AC	+	+	-	T2N1M0
19	34	6x Docetaxel - AC	-	-	-	T2N0M0
20	54	6x Docetaxel - AC	+	+	-	T2N1M0
21	33	6x Docetaxel - AC	-	-	-	T2N1M0
22	51	6x Docetaxel - AC	+	+	-	T2N0M0

ER Estrogen Receptor; *PR* Progesterone Receptor; *HER2* Human Epidermal growth factor Receptor 2 *TNM stage* Classification of malignant tumors (Tumor, Nodes, Metastasis); *AC* Adriamycin and Cyclophosphamide; *FEC* 5-Fluorouracil, Epirubicin and Cyclophosphamide

APT-MRI

For APT-MRI, 33 frequency offsets were acquired unevenly distributed over the frequencies from -1 ppm to 33 ppm relative to the water resonance; more offsets were obtained around the frequency of the amide peak (3.5 ppm) and the water peak (0.0 ppm) for better fitting of these resonances. The frequency offsets associated with the nuclear Overhauser effect (NOE) were not included due to signal distortions by unsuppressed lipid resonances. A 4 s saturation train (20 sinc-Gauss radiofrequency (RF) pulses, pulse duration = 100 ms, inter-pulse delay = 100 ms, peak amplitude $B_1 \approx$ 2 µT, duty cycle of 50%, average nominal $B_1 \approx 0.9$ µT) was followed by a gradient-echo readout (34), and a short 1-2-1 spectral-spatial RF pulse was used for fat-suppression (TE = 1.4 ms, TR = 2.6 ms, flip angle = 1.2°, FOV = 150x320x100 mm^3 (FHxRLxAP), nominal resolution = 2.3x3.0x6.8 mm^3, 29 slices). A total of 2 shots with an interval of 4.48 s (9 s per frequency offset) and a 4-fold acceleration in right-left direction resulted in a total scan time of 4 min 55 s.

^{31}P-MRSI

The scan session consisted of a fat suppressed T_1 weighted 3D MRI (TE = 2 ms; TR= 4 ms; flip angle = 10 °; FOV = 160 x 160 x 160 mm^3; isotropic resolution of 1.0 mm^3) for locating the tumor. ^{31}P-MRSI was obtained using the AMESING sequence (35) (ΔTE = 45 ms, TR = 6 s, FOV = 160 x 160 x 160 mm^3, nominal resolution = 2 x 2 x 2 cm^3, BW = 8200 Hz, sampling matrix size = 256) where one FID and five full echoes were acquired in a total scan time of 25 min 36 s.

Data analysis and pH measurement

Image processing and data analysis of the CEST data was performed with MATLAB 2014b (MathWorks, Natick, MA, USA). B_0 correction was applied using the WASSR method (36). Amide proton transfer (APT) maps were calculated using a three-pool Lorentzian model (37) (free water pool, APT and magnetization transfer (MT)) with the Levenberg-Marquardt algorithm (fitting parameters can be found in Table 2) using the amplitude of the fit. To determine the mean APT signal in the entire tumor volume, a region of interest (ROI) was drawn on a CEST image acquired at 5.4 ppm down-field from the water resonance.

The hypothesis, assuming the chemical exchange is dominantly base-catalyzed and that it is directly related to the APT signal, was calculated using: $k = k_0 + [k_b \times 10^{pH-pKw}]$, with $k_0 = 26.8$, $k_b = 3.4 \times 10^6$, and $pK_w = 11.2$ (6,21). This relationship was used to compare it to the measured data.

Table 2 Starting points and boundaries of all fit parameters of the three-pool Lorentzian fit

	Start	Lower	Upper
Z_{base}	0.5	0.5	1
A_{water}	0.8	0	1
Γ_{water}	1	0.1	2.5
δ_{water}	0	-1	1
A_{MT}	0.1	0	1
Γ_{MT}	5	3	100
δ_{MT}	0	-0.5	0.5
A_{amide}	0.1	0	1
Γ_{amide}	1	1	1.5
δ_{amide}	3.5	3.3	3.7

The chemical shift δ and FWHM Γ are given in ppm.
Γ FWHM, *δ* chemical shift, *MT* Magnetization Transfer

All MRSI data were analyzed using IDL 6.3 (Research Systems, Boulder, CO, USA), jMRUI 4.0 (38) and Matlab 2014b. Voxel selection of the breast tumor was performed in an in-house built program in Matlab on the fat suppressed T_1 weighted 3D MRI. All spectra were zero-filled to 8192 data points and apodized (15 Hz Lorentzian) in the time domain and spatially Hamming filtered. For the pH measurement, all spectra were aligned to α-ATP at 7.56 ppm as α-ATP is the most insensitive to pH of all peaks with high signal to noise ratio. pH values were calculated using the following form of the Henderson–Hasselbalch equation (39):

$$pH = pK_A + log_{10}\left(\frac{\delta - \delta_{HA}}{\delta_A - \delta}\right)$$

Where $pK_A = 6.75$ is the dissociation constant of Pi, $\delta_{HA} = 3.27$ is the chemical shift of the protonated form of Pi, $\delta_A = 5.69$ is the chemical shift of the non-protonated form of Pi, and δ is the difference in chemical shift frequency between the Pi peak and the reference α-ATP peak, measured in parts per million (ppm).

^{31}P-MRSI is known to be used to image metabolites involved in the disturbed anabolism and catabolism of the cell membrane in breast cancer. Metabolite ratios such as PME/PDE ratio and phosphoethanolamine/inorganic phosphate (PE/Pi) ratio were related to pH and APT signal. For calculating the metabolic signal ratios for PME/PDE and PE/Pi, all spectra were frequency aligned to PE at 6.83 ppm and quantified using a nonlinear least-squares algorithm (AMARES) (40).

Statistical Analysis

Statistical analysis was performed in GraphPad Prism (GraphPad Software, San Diego, CA, USA). A linear regression was used to determine the correlation between the measured APT signal, metabolic ratios and the pH before and after the first cycle of NAC treatment. The correlation was considered statistically significant if $p < 0.05$. Relative change of these parameter, as measured prior and after the first NAC cycle was quantified. Values less than the first quartile - 1.5 x interquartile range or greater than the third quartile + 1.5 interquartile range were determined as outliers (< Q1–1.5xIQR or > Q3+1.5xIQR).

Results

The mean age of the twenty-two patients was 47 years (range 33-61 years) and all patients completed all cycles of NAC treatment (four different regimes were used; Table 1). Assessment of hormone receptor status was performed on the pre-treatment core biopsy and six patients had human epidermal growth factor receptor 2 positive (HER2+) tumors and the others patients had HER2- tumors. Ten tumors were estrogen receptor positive (ER+) of which seven tumors were progesterone receptor positive (PR+). Eight tumors were triple negative.

An example of the analysis of the acquired data of a patient (patient 13 from Table 1 before the start of NAC treatment) is shown in Figure 1. For analysis of ^{31}P-MRSI, one voxel containing the tumor was selected (Figure 1A) and 9 metabolites were fitted (Figure 1B). The metabolic ratios of metabolites involved in membrane metabolism (PME/PDE and PE/Pi) and the pH (based on the chemical shift between Pi and α-ATP) were calculated. From the APT-MRI, the mean APT signal was determined inside the tumor volume (Figure 1C) based on the three pool Lorentzian fit.
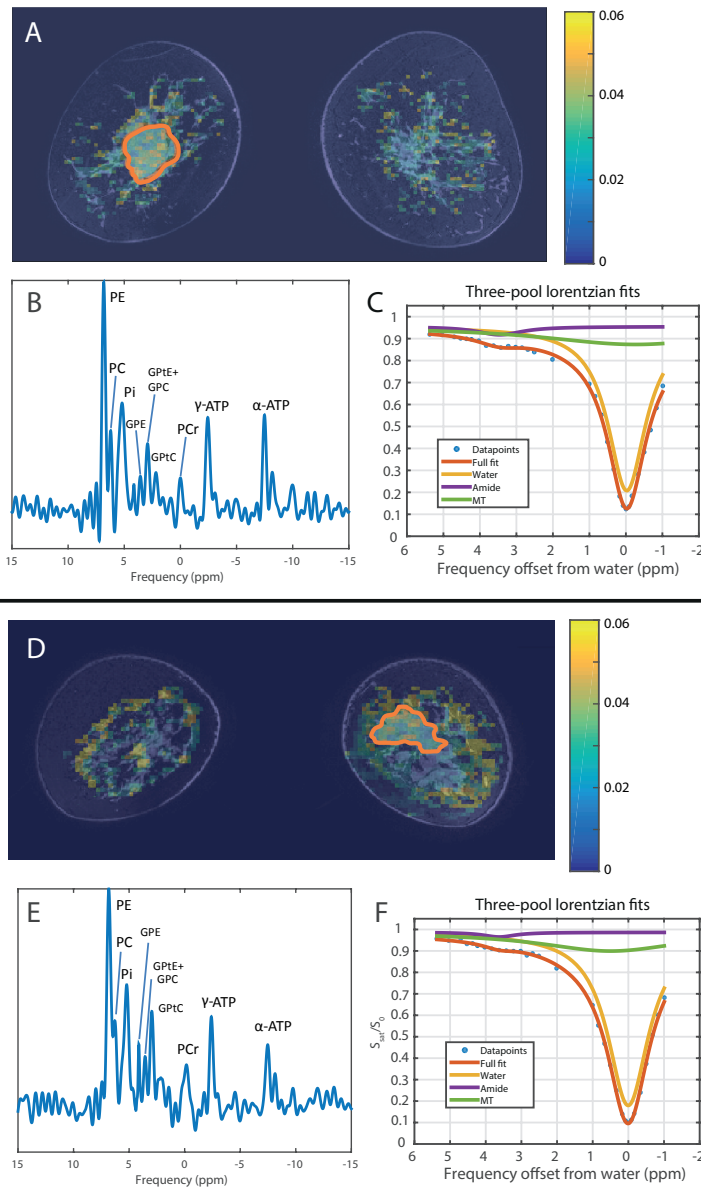
Figure 1 Example of acquired and calculated data (patients 13, upper half, and 14, lower half from Table 1 before the start of NAC treatment). **A&D)** Coronal slices of the calculated APT maps with the ROIs of the tumor (orange) overlaid on top of a fat suppressed T_1 weighted 3D FFE (TR=7.1ms; TE=3.2ms; flip angle=8°; resolution of 0.7 mm³; SENSE 4x2 (RLxFH), 1-4-6-4-1 spectral spatial RF pulse for fat suppression). Note that both ³¹P-MRS and CEST analysis were performed on the entire tumor volume; only one coronal slice is shown here. **B&E)** Corresponding ³¹P-MRSI spectra originating from the ROI where 9 metabolites are visible. **C&F)** Three-pool Lorentzian fit of the Z-spectra of water (yellow line), magnetization transfer effect (MT; green line), amide proton transfer (APT; purple line) and the full fit consisting of the three fits (orange).

We have found a statistically significant correlation between APT-CEST and pH when combining all data from all patients (Figure 2). This correlation was, however, in opposite direction as theory suggests (dashed gray line); an increase of pH showed a decrease in APT-CEST signal. When splitting the group into before and after the first cycle of NAC treatment, the linear regressions were still in opposite direction compared to the hypothesis yet no longer significant (Figure 3).

The PME/PDE ratio, known to be involved with membrane anabolism and catabolism, showed no significant correlation with pH (Figure 4). A significant negative correlation between PE/Pi ratio and pH was found prior to NAC treatment. After the first cycle of NAC treatment, the correlation was no longer significant.
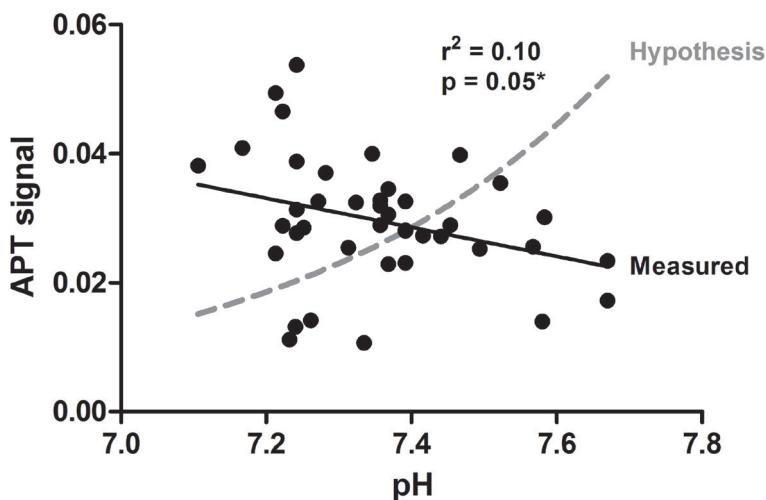

Figure 2 Relation between APT signal and pH measured by CEST and 31P-MRS (based on the chemical shift between Pi and α-ATP) for all patients before and after the first cycle of NAC treatment. The hypothesis (dashed gray line) was calculated based on Sun et al. (6) using $k = k_0 + [k_b \times 10^{pH-pKw}]$, with $k_0 = 26.8$, $k_b = 3.4 \times 10^6$, and $pK_w = 11.2$, and normalized to the measured data. The linear regression is shown by the solid black line which is already significant without correcting for known (Sun et al.) pH effects ($p < 0.05$). Note that the measured data is contradicting the hypothesis; a decreasing APT-CEST with increasing pH opposed to the hypothesis.

An absolute mean shift of 0.1 unit pH was observed after the first cycle of NAC treatment with a maximum of 0.3 unit pH in the individual patient. When averaging over all patients, the tumor tissue had a slightly alkaline pH of 7.4 before the start of NAC treatment and did not change after the first cycle of NAC treatment.
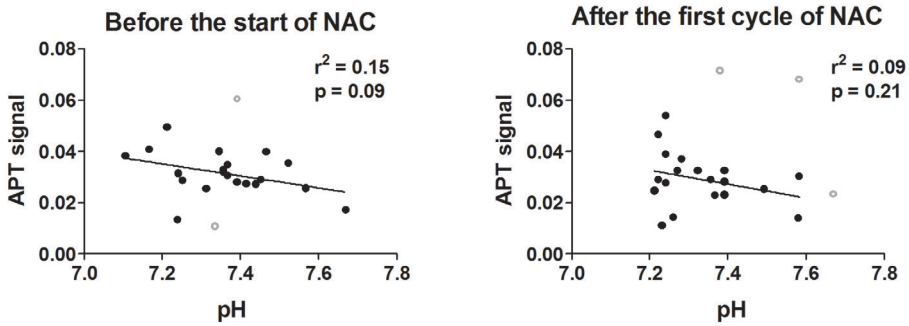
Figure 3 Relation of APT signal with pH before (left) and after the first cycle of NAC treatment (right). Separating the data in these two groups resulted in a linear regression which was no longer significant for both. The outliers are shown in gray.
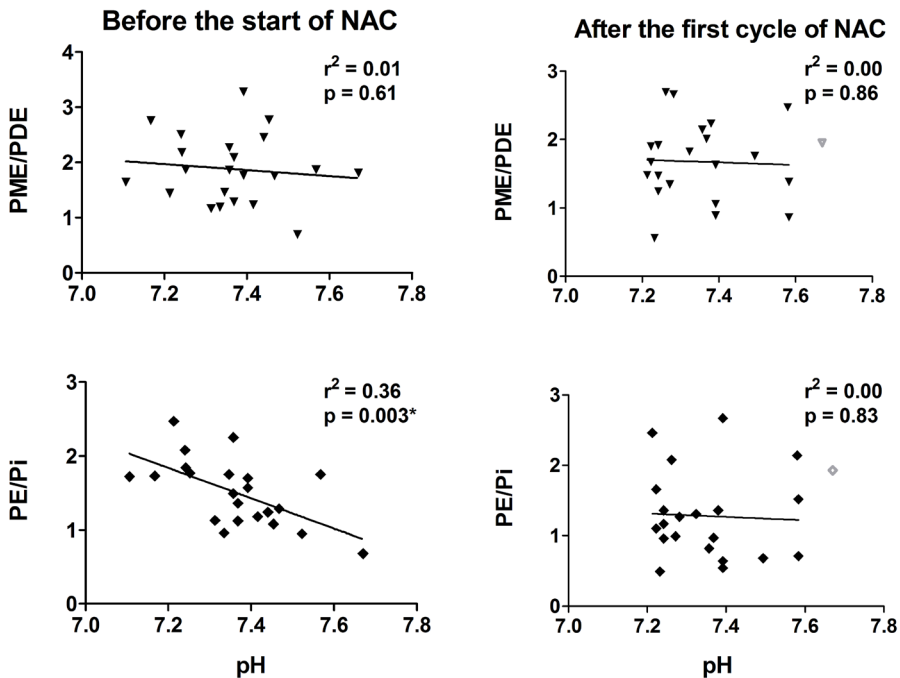

Figure 4 Relation of PME/PDE and PE/Pi with pH before (left column) and after the first cycle of NAC treatment (right column). The linear regressions are shown as black solid lines. The linear regression between PE/Pi and pH before the first the start of NAC treatment was significant. The outliers are shown in gray.

Discussion

In this study we acquired a unique dataset at 7 T; APT-MRI and ^{31}P-MRSI of breast cancer patients receiving NAC treatment. This data enabled the investigation of the relationship between APT and pH with a direct measure of pH through ^{31}P-MRSI, which has not been presented before. Based on the chemical shift between Pi and α-ATP from the ^{31}P-MRSI spectra, we calculated the pH of all patients before and after the first cycle of NAC treatment. We showed that there was a statistical significant correlation between the APT signal and pH and between PE/Pi and pHi before the start of NAC treatment. After the first cycle of NAC treatment, these correlations appeared to be no longer significant. The pHi (Pi signal mostly originates from the cytosolic compartment (41)) remains neutral to slightly alkaline, which tumors are known for.

We showed that proliferation measured with PE/Pi is higher with lower pHi, which suggests increased cellularity at lower pHi. This would also suggest that there will be an increased concentration of proteins, resulting in higher CEST effects at lower pH mainly due to the concentration of proteins and peptides. This was confirmed by the APT measurements during this study. However, this is in contradiction to the naïve interpretation that APT must be smaller at lower pH due to the lower base-catalyzed amide proton exchange rate, but hints to the finding that, for the APT signal, concentration effects outweigh direct pH effects. The measured APT signal depends on physiological parameters and sequence parameters. First, the physiological parameters are discussed.

As mentioned before, APT signal is primarily related to the concentration of mobile amide protons, the amide proton exchange rate and T_1 relaxation of water. A change in T_1 relaxation time due to therapy effects could influence the APT signal, as T_1 relaxation is positively related with APT signal (42,43). However, the APT signal varies a factor 2 between tumors, this cannot be assigned to only changes in T_1 relaxation time as this would mean differences in tumor T_1 of 50% (44) which is unrealistic. Therefore we assumed that the expected effect size of T_1 relaxation on the APT signal is much less in comparison to the concentration of mobile amide protons and the exchange rate.

In normal tissue, it is expected that the extracellular compartment contains low concentration of mobile amides. Therefore, APT signal in normal tissue most likely originates from proteins and peptides in the intracellular space. In tumor tissue however, the extracellular space could contain increased concentrations of mobile

proteins and peptides as a result of accumulation of blood-borne proteins, such as albumin, due to perforated blood vessels (45). Therefore, both intracellular and extracellular compartment are likely to contribute to APT signal originating from tumor tissue. Intracellular pH in tumor tissue did not change much (slightly alkaline, mean pH of 7.4) and so APT signal change, originating from intracellular compartment, assuming T_1 relaxation will have the least effect (see above), reflects a change in protein content. Extracellular pH in tumors is acidic and APT-MRI, originating from extracellular compartment, reflects a change in protein content and pH. Only a small part of the pH (~15%) that is determined by ^{31}P-MRS originates from the extracellular compartment and therefore it is difficult to rule out parameters affecting the APT signal originating from the extracellular compartment. However, this data does suggest that the concentration of the mobile amide protons is the main contributor to the observed APT signal.

Considering the main influence of the concentration of the mobile amide protons, the dependency of the APT signal on the mobile amide protons is much stronger than its contra related dependency to the exchange rate. A recent study in a rat model of brain metastasis determined that the proportion of APT signal originating from changes in protein concentration was approximately 66%, with the remaining 34% originating from changes in tumor pH (46).

It has been shown that NOE signals from aromatic protons, in a range of +1 to +5 ppm from water, affect the quantification of APT effects (47). These aromatic NOE signals also originate from proteins, yet are insensitive to pH. If these signals decrease due to therapy effects, they could surpass the effect of the actual amides, resulting in this inverse pH dependency. It could also be that overlapping CEST signals from different exchanging sites influence the APT signal. It has been shown that fast-exchanging amines can have an inverse pH dependency in animals (48) and homogenates (49). However, the nominal B_1 in this study was 2 µT (sinc-gaussian pulses) with a duty cycle of 50%. This means that the average nominal B_1 is less than 0.9 µT. Also, the relative B_1 in the tumor area is ca. 50-60% (see below) resulting in ca. 0.5 µT average effective B_1 in the tumor. Considering this B_1, the main contributor to the measured signal is APT (ca. 90%) (50) which makes the contribution of fast exchanging protons highly unlikely. A more likely explanation for the decrease of APT with increasing pH, would be the decreasing cellularity (PE/Pi) with pH. A low cellularity hints to a lowered concentration of proteins, which is a more probable explanation for the decreased APT signal.

A sequence dependent parameter affecting APT signals is B_1 inhomogeneity. In this study, the CEST was optimized for signal generated by the slow exchanging amide protons and the optimal B_1 for detecting this exchange is approximately 1 µT (51). The peak B_1 amplitude in this study was set to 2 µT to account for B_1 loss in the hardware setup. The bilateral breast coil setup consisted of two quadrature RF coils placed in front of the breasts, which led to a decrease in B_1 varying from 60% in the front of the breast to 50% towards the pectoral muscle. This means that the APT signal coming from tumors located near the nipple could be higher than the signal coming from tumors located near the pectoral muscle. Also here, the level of variance in B_1 and its effect on the APT signal cannot explain the level of observed APT signal changes. Particularly when considering that the tumor location with respect to the RF coil is not expected to change substantially over one cycle of chemotherapy.

The overall calculated APT contrast could also be influenced by the degree of fat suppression. We used RF and gradient spoiling to reduce lipid artefacts. However, insufficient fat suppression in the tumor may have resulted in an underestimation of the CEST amplitude (52), possibly affecting the change in APT signal.

We were able to perform ^{31}P-MRSI analysis for every individual patient. A linear correlation was found in this study between PE/Pi before NAC treatment and the pHi. PE is a key metabolite involved in the Kennedy pathway that produces phosphatidylserine in the major building block of cell membranes (29). Pi is involved in many metabolic pathways, including energy transfer, protein activation, and carbon and amino acid metabolic processes (53). Therefore, PE/Pi could be an indicator for cellularity. After the first cycle of NAC this correlation is not significant. NAC treatment has been shown to be most effective if a combination of anthracyclines and taxanes is used, causing damage to DNA and disrupting pathways necessary to facilitate mitosis (54). Therefore, it is most likely that PE, Pi and pH in the tumor are all affected by the chemotherapy. However, further research is required to understand this linear relationship between PE/Pi and pH.

In conclusion, in this study we have shown that APT-MRI and ^{31}P-MRSI provide complementary information about tumor metabolism in breast cancer patients. A linear correlation between APT signal and pH and a linear correlation between PE/Pi and the pH in the tumor was found in breast cancer patients before the start of NAC treatment. This correlation was opposite from the intrinsic relation between APT signal and pH, demonstrating that the concentration of mobile amide protons is the main contributor to the observed APT signal. In fact, when correcting for the known intrinsic relation of APT with pH, the observed concentration range of mobile amides will be even higher.

References

1.   van Zijl PCM, Yadav NN. Chemical exchange saturation transfer (CEST): What is in a name and what isn't? Magn Reson Med. 2011;65(November 2010):927–48.

2.   Zhou JY, Lal B, Wilson D, Laterra J, Van Zijl PCM. Amide Proton Transfer (APT) Contrast for Imaging of Brain Tumors. Magn Reson Med. 2003;50(6):1120–6.

3.   Heo HY, Jones CK, Hua J, Yadav N, Agarwal S, Zhou J, et al. Whole-brain amide proton transfer (APT) and nuclear overhauser enhancement (NOE) imaging in glioma patients using low-power steady-state pulsed chemical exchange saturation transfer (CEST) imaging at 7T. J Magn Reson Imaging. 2016;44(1):41–50.

4.   Khlebnikov V, Siero JCW, Bhogal AA, Luijten PR, Klomp DWJ, Hoogduin H. Establishing upper limits on neuronal activity–evoked pH changes with APT-CEST MRI at 7 T. Magn Reson Med. 2018;80(1):126–36.

5.   Jones CK, Schlosser MJ, Van Zijl PCM, Pomper MG, Golay X, Zhou J. Amide proton transfer imaging of human brain tumors at 3T. Magn Reson Med. 2006;56(3):585–92.

6.   Sun PZ, Gregory Sorensen A. Imaging pH using the chemical exchange saturation transfer (CEST) MRI: Correction of concomitant RF irradiation effects to quantify cest MRI for chemical exchange rate and pH. Magn Reson Med. 2008;60(2):390–7.

7.   Van Zijl PCM, Zhou J, Mori N, Payen JF, Wilson D, Mori S. Mechanism of magnetization transfer during on-resonance water saturation. A new approach to detect mobile proteins, peptides, and lipids. Magn Reson Med. 2003;49(3):440–9.

8.   Klomp DWJ, Dula AN, Arlinghaus LR, Italiaander M, Dortch RD, Zu Z, et al. APT imaging of the human breast at 7T: development and reproducibility. NMR Biomed. 2013 Oct;26(10):1271–7.

9.   Anemone A, Consolino L, Conti L, Reineri F, Cavallo F, Aime S, et al. In vivo evaluation of tumour acidosis for assessing the early metabolic response and onset of resistance to dichloroacetate by using magnetic resonance pH imaging. Int J Oncol. 2017;51(2):498–506.

10.   Dula AN, Arlinghaus LR, Dortch RD, Dewey BE, Whisenant JG, Ayers GD, et al. Amide proton transfer imaging of the breast at 3 T: Establishing reproducibility and possible feasibility assessing chemotherapy response. Magn Reson Med. 2013;70:216–24.

11.   Abramson RG, Arlinghaus LR, Weis JA, Li X, Chekmenev EY, Smith SA, et al. Current and emerging quantitative magnetic resonance imaging methods for assessing and predicting the response of breast cancer to neoadjuvant therapy. 2012;139–54.

12.   Chan KWY, Jiang L, Cheng M, Wijnen JP, Liu G, Huang P, et al. CEST-MRI detects metabolite levels altered by breast cancer cell aggressiveness and chemotherapy response. NMR Biomed. 2016;29(6):806–16.

13.   Mcvicar N, Li AX, Meakin SO, Bartha R. Imaging chemical exchange saturation transfer (CEST) effects following tumor-selective acidification using lonidamine. NMR Biomed. 2015;28:566–75.

14.   Mehrabian H, Myrehaug S, Soliman H, Sahgal A, Stanisz GJ. Evaluation of Glioblastoma Response to Therapy With Chemical Exchange Saturation Transfer. Int J Radiat Oncol Biol Phys. 2018;101(3):713–23.

15.   Sagiyama K, Mashimo T, Togao O, Vemireddy V, Hatanpaa KJ, Maher EA, et al. In vivo chemical exchange saturation transfer imaging allows early detection of a therapeutic response in glioblastoma. Proc Natl Acad Sci. 2014;111(12):4542–7.

16.   Regnery S, Adeberg S, Dreher C, Oberhollenzer J, Meissner J-E, Goerke S, et al. Chemical exchange saturation transfer MRI serves as predictor of early progression in glioblastoma patients. Oncotarget. 2018;9(47):28772–83.

4

17.   Jones KM, Michel KA, Bankson JA, Fuller CD, Klopp AH, Venkatesan AM. Emerging Magnetic Resonance Imaging Technologies for Radiation Therapy Planning and Response Assessment. Int J Radiat Oncol Biol Phys [Internet]. 2018;101(5):1046–56.

18.   Choyke PL. Science to Practice: Monitoring Oncolytic Virus Therapy with Chemical Exchange Saturation Transfer MR Imaging—Wishful Thinking? Radiology. 2015;275(3):625–6.

19.   Desmond KL, Mehrabian H, Chavez S, Sahgal A, Soliman H, Rola R, et al. Chemical exchange saturation transfer for predicting response to stereotactic radiosurgery in human brain metastasis. Magn Reson Med. 2017;78(3):1110–20.

20.   Liu J, Bai R, Li Y, Staedtke V, Zhang S, van Zijl PCM, et al. MRI detection of bacterial brain abscesses and monitoring of antibiotic treatment using bacCEST. Magn Reson Med. 2018;80(2):662–71.

21.   Zhou J, Payen JF, Wilson DA, Traystman RJ, Van Zijl PCM. Using the amide proton signals of intracellular proteins and peptides to detect pH effects in MRI. Nat Med. 2003;9(8):1085–90.

22.   Hanahan D, Weinberg RA. Hallmarks of Cancer: The Next Generation. Cell. 2011;144(1):646–74.

23.   Griffiths JR. Are cancer cells acidic? Br J Cancer. 1991;64(3):425–7.

24.   Huber V, Milito A De, Harguindey S, Reshkin SJ, Wahl ML, Rauch C, et al. Proton dynamics in cancer. J Transl Med. 2010;8(57):1–5.

25.   Neri D, Supuran CT. Interfering with pH regulation in tumours as a therapeutic strategy. Nat Rev Drug Discov. 2011;10(10):767–77.

26.   Moon RB, Richards JH. Determination of Intracellular pH by 31P Magnetic Resonance. J Biol Chem. 1973;248(25):7276–8.

27.   Vaupel P, Kallinowski F, Okunieff P. Blood Flow , Oxygen and Nutrient Supply , and Metabolic Microenvironment Human Tumors : A Review. Cancer Res. 1989;49(23):6449–65.

28.   Shah T, Krishnamachary B, Wildes F, Wijnen JP, Glunde K, Bhujwalla ZM. Molecular causes of elevated phosphoethanolamine in breast and pancreatic cancer cells. NMR Biomed. 2018;31:1–9.

29.   Podo F. Tumour phospholipid metabolism. NMR Biomed. 1999;12(7):413–39.

30.   Schmitz AMT, Veldhuis WB, Menke-Pluijmers MBE, Van Der Kemp WJM, Van Der Velden TA, Kock MCJM, et al. Multiparametric MRI with dynamic contrast enhancement, diffusion-weighted imaging, and 31-phosphorus spectroscopy at 7 T for characterization of breast cancer. Invest Radiol. 2015;50(11):766–71.

31.   Kemp WJM van der, Stehouwer BL, Luijten PR, Bosch MAAJ van den, Klomp DWJ. Detection of alterations in membrane metabolism during neoadjuvant chemotherapy in patients with breast cancer using phosphorus magnetic resonance spectroscopy at 7 Tesla. Springerplus. 2014;3(1):634.

32.   Krikken E, Khlebnikov V, Zaiss M, Jibodh RA, Diest PJ van, Luijten PR, et al. Amide chemical exchange saturation transfer at 7 T: A possible biomarker for detecting early response to neoadjuvant chemotherapy in breast cancer patients. Breast Cancer Res. 2018;20:51.

33.   Hancu I, Govenkar A, Lenkinski RE, Lee SK. On shimming approaches in 3T breast MRI. Magn Reson Med. 2013;69(3):862–7.

34.   Khlebnikov V, Geades N, Klomp DWJ, Hoogduin H, Gowland P, Mougin O. Comparison of Pulsed Three-Dimensional CEST Acquisition Schemes at 7 Tesla : Steady State Versus Pseudosteady State. Magn Reson Med. 2016;00:2280–7.

35.   van der Kemp WJM, Boer VO, Luijten PR, Stehouwer BL, Veldhuis WB, Klomp DWJ. Adiabatic multi-echo ^{31}P spectroscopic imaging (AMESING) at 7 T for the measurement of transverse relaxation times and regaining of sensitivity in tissues with short T2* values. NMR Biomed. 2013;26(April):1299–307.

36.   Kim M, Gillen J, Landman BA, Zhou J, Van Zijl PCM. Water saturation shift referencing for

chemical exchange saturation transfer (CEST) experiments. Magn Reson Med. 2009;61:1441–50.

37. Windschuh J, Zaiss M, Meissner J, Paech D, Radbruch A, et al. Correction of B 1-inhomogeneities for relaxation-compensated CEST imaging at 7T. NMR Biomed. 2015;28:529–37.

38. Naressi A, Couturier C, Devos JM, Janssen M, Mangeat C, et al. Java-based graphical user interface for the MRUI quantitation package. Magn Reson Mater Physics, Biol Med. 2001;12(2–3):141–52.

39. Lanza IR, Bhagra S, Nair KS, Port JD. Measurement of human skeletal muscle oxidative capacity by 31P-MR spectroscopy: A cross-validation with in vitro measurements. J Magn Reson Imaging. 2011;34(5):1143–50.

40. Vanhamme L, Van Den Boogaart A, Huffel S Van. Improved Method for Accurate and Efficient Quantification of MRS Data with Use of Prior Knowledge. J Magn Reson. 1997;129:35–43.

41. Soto GE, Zhu Z, Evelhoch JL, Ackerman JJH. Tumor 31P NMR pH Measurements in Vivo: A Comparison of Inorganic Phosphate and Intracellular 2-Deoxyglucose-6-Phosphate as pHnmr Indicators in Murine Radiation-Induced Fibrosarcoma-1. Magn Reson Med. 1996;36(5):698–704.

42. Zaiss M, Windschuh J, Paech D, Meissner JE, Burth S, Schmitt B, et al. Relaxation-compensated CEST-MRI of the human brain at 7T: Unbiased insight into NOE and amide signal changes in human glioblastoma. Neuroimage. 2015;112:180–8.

43. Khlebnikov V, Polders D, Hendrikse J, Robe PA, Voormolen EH, Luijten PR, et al. Amide Proton Transfer (APT) Imaging of Brain Tumors at 7 T : The Role of Tissue Water T1 -Relaxation Properties. Magn Reson Imaging. 2017;77:1525–32.

44. Khlebnikov V, Siero JCW, Wijnen J, Visser F, Luijten PR, Klomp DWJ, et al. Is there any difference in Amide and NOE CEST effects between white and gray matter at 7 T? J Magn Reson. 2016;272:82–6.

45. Matsumura Y, Maeda H. A new concept for macromolecular therapeutics in cancer chemotherapy: mechanism of tumoritropic accumulation of proteins and the antitumor agent smancs. Cancer Res. 1986;46(12 Pt 1):6387–92.

46. Ray KJ, Simard MA, Larkin JR, Coates J, Kinchesh P, Smart C, et al. Tumour pH and protein concentration contribute to the signal of amide proton transfer MRI. Cancer Res. 2019;44.

47. Jin T, Kim SG. In vivo saturation transfer imaging of nuclear Overhauser effect from aromatic and aliphatic protons: implication to APT quantification. Proc Intl Soc Mag Reson Med 21. 2013;2528.

48. Jin T, Wang P, Hitchens TK, Kim SG. Enhancing sensitivity of pH-weighted MRI with combination of amide and guanidyl CEST. Neuroimage. 2017;157:341–50.

49. Zaiss M, Windschuh J, Goerke S, Paech D, Meissner J, Burth S, et al. Downfield-NOE-Suppressed Amide-CEST-MRI at 7 Tesla Provides a Unique Contrast in Human Glioblastoma. Magn Reson Med. 2017;77:196–208.

50. Khlebnikov V, Kemp WJM Van Der, Hoogduin H, Klomp DWJ, Prompers JJ. Analysis of chemical exchange saturation transfer contributions from brain metabolites to the Z-spectra at various field strengths and pH. Sci Rep. 2019;9:1089.

51. Zu Z, Li K, Janve VA, Does MD, Gochberg DF. Optimizing pulsed-chemical exchange saturation transfer imaging sequences. Magn Reson Med. 2011;66(4):1100–8.

52. Zhang S, Keupp J, Wang X, Dimitrov I, Madhuranthakam AJ, Lenkinski RE, et al. Z-spectrum appearance and interpretation in the presence of fat: Influence of acquisition parameters. Magn Reson Med. 2017;00:1–7.

53. Wu P. Phosphate Starvation Triggers Distinct Alterations of Genome Expression in Arabidopsis Roots and Leaves. Plant Physiol. 2003;132(3):1260–71.

54. Cleator S, Parton M, Dowsett M. The biology of neoadjuvant chemotherapy for breast cancer. Endocr Relat Cancer. 2002;9(3):183–95.

4

Homogeneous B_1^+ for bilateral breast imaging at 7T using a 5 dipole transmit array merged with a high density receive loop array.

Erwin Krikken

Bart R. Steensma

Ingmar J Voogt

Peter R. Luijten

Dennis W.J. Klomp

Alexander J.E. Raaijmakers

Jannie P. Wijnen

5

Abstract

Purpose: To explore the use of five meandering dipole antennas in a multi-transmit setup, combined with a high density receive array for breast imaging at 7 tesla for improved penetration depth and more homogeneous B_1 field.

Methods: Five meandering dipole antennas and thirty receiver loops were positioned on two cups around the breasts. Finite difference time domain simulations were performed to evaluate RF safety limits of the transmit setup. Scattering parameters of the transmit setup and coupling between the antennas and the detuned loops were measured. In vivo parallel imaging performance was investigated for various acceleration factors. After RF shimming, a B_1 map, a T_1-weighted image and a T_2-weighted image were acquired to assess B_1 efficiency, uniformity in contrast weighting, and to demonstrate imaging performance in clinical applications.

Results: The maximum achievable local SAR_{10g} value was 7.0 W/kg for 5x1 W accepted power. The dipoles were tuned and matched to a maximum reflection of -11.8 dB, and a maximum inter-element coupling of -14.2 dB. The maximum coupling between the antennas and the receive loops was -18.2 dB and the mean noise correlation for the 30 receive loops 7.83 ± 8.69%. In vivo measurements show an increased field of view, which reached to the axilla, and a high transmit efficiency.

Conclusions: In vivo measurements show a field of view reaching to the axilla using the bilateral breast coil. This coil enabled the acquisition of T_1 weighted images with a high spatial resolution of 0.7 mm^3 isotropic and T_2 weighted spin echo images with uniformly weighted contrast.

Keywords: Dipole antenna; Breast imaging; High field; 7 tesla

Introduction

Imaging of the breast at 7 tesla (7T) is of interest due to the increased spectral and spatial resolution enabling characterization of breast cancer and monitoring of treatment. However, breast imaging at 7T is challenging mainly due to severe non-uniformities in radio-frequency (RF) transmit (B_1^+) fields[1–3] and limited penetration depth. An homogeneous B_1^+ field is particularly important for magnetic resonance (MR) sequences such as a turbo spin echo. (TSE), which can still not compete to the clinical standard at 3T[4]. One approach to overcome B_1 inhomogeneity is forced current excitation as demonstrated in previous studies[5–7]. Another approach is the use of a multi-transmit setup where RF-shimming can be used to improve transmit uniformity for every subject[1,8].

A wide variety of breast MRI studies at 7T have been presented with various RF coil setups[7,9–17]. Although imaging performance in the anterior part of the breast is generally good, clinical usability might be impeded by limited penetration depth towards the pectoral muscle which is an often occurring challenge. To our knowledge, previous work on 7T breast imaging did not show bilateral T_2 weighted imaging or a FOV reaching the axillary lymph nodes; two important measures which are essential for translation of the 3T clinical exam to 7T. Next to a uniform B_1^+, B_1^+ efficiency is important for dynamic contrast enhanced (DCE) MRI, where short but high flip angles are needed. Next to that, T_2 relaxation time in breast tissue is short, therefore shorter 180° pulses are needed. Also, the bandwidth, for example, of pulses in MR spectroscopy (MRS) will be affected by the B_1^+ efficiency causing chemical shift displacements.

It has been demonstrated that dipole antennas[18] have enhanced field uniformity and penetration depth compared to loop coils[19], which are often used in other breast coil designs. Since these are the main issues with breast imaging at 7T, we explored whether the use of five meandering dipole antennas[20,21] (based on fractionated dipole antennas) in combination with 30 receive loops help to improve the transmit efficiency, B_1^+ homogeneity and penetration depth. Specific absorption rate (SAR) and B_1^+ simulations are performed and compared to in vivo measurements to evaluate RF safety limits of this design.
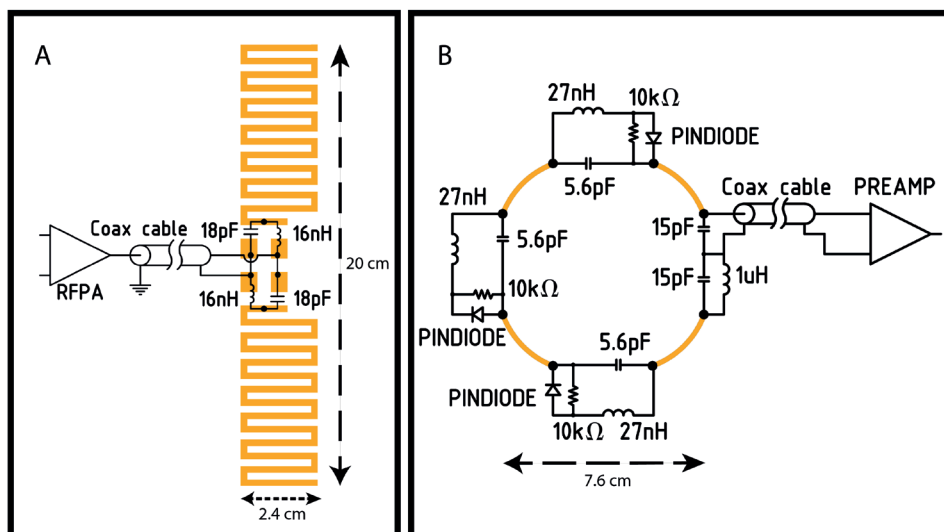
5

Figure 1 Electric circuitry of a meandering dipole antenna on the left **(A)** and the electric circuitry of the receive loops on the right **(B)**. The black dots indicate the points where the lumped elements are soldered onto the printed circuit boards (PCB).

Subjects and Methods

Hardware

Five meandering dipole antennas were connected to five transmit channels of an eight channel multi-transmit setup (8 x 2 kW peak power amplifiers, CPC, New York, USA) on a 7T MR system (Philips, Cleveland, OH, USA). The design of the meandering dipole antenna was modified to tune the dipole antennas to resonance at a length of 20 cm, in order to fit next to the cups around the breasts and to match the geometry of the previous in-house built coil[14] so associating pillows and pads could be reused. Figure 1 shows the electrical circuit of the meandering dipole antennas (Figure 1A), which was identical for all antennas and the receive loops (Figure 1B). The dipole legs have a meandering geometry (Figure 1A), in order to maintain resonance in a loaded situation for the given length, and to reduce SAR levels[20-22]. The antenna and the positioning of the antennas are schematically shown in Figure 2A and 2B. The dipole antennas were manufactured on printed circuit boards of the material FR-4 (Eurocircuits N.V., Mechelen, Belgium). Ideally, the position of the antennas should be parallel to the receive loops to minimize coupling, however due the geometry of breast this was not possible for all coils. The chosen solution is a tradeoff between practical geometric position and minimized coupling.
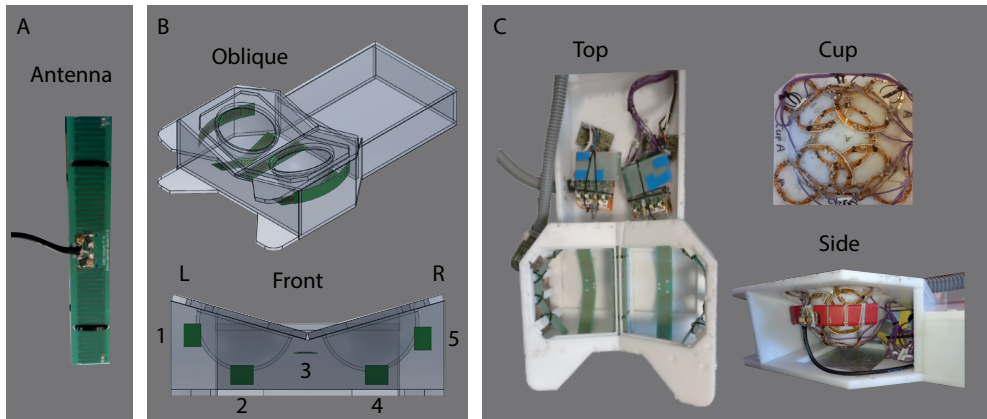
Figure 2 Setup of the breast coil. One of the five meandering dipole antennas used in the breast coil on the left **(A)**. Oblique and front view of the schematic design of the breast coil where the placement of the dipole antennas is shown in green **(B)**. Different views (top, cup and side view) of the hardware inside the coil on the right **(C)**.

Thirty receiver loops were tuned at 298 MHz and positioned on two cups around the breasts; fifteen receivers with a diameter of 7.6 cm, for each cup. To protect the volunteers from potential electric hazards, a 1 cm layer of electrically isolating material is placed between the receive circuitry and the volunteers. Each loop is individually shaped to match the geometry of the cups (Figure 2C). Decoupling of the loops was performed by overlapping of the adjacent loops and by preamplifier decoupling. Each receiver loop was actively detuned during the transmit phase using a parallel trap circuit with a PIN diode. The scattering parameters of the dipole antennas were measured with directional couplers during scanning[23]. Coupling between the antennas in the presence of the detuned receiver loops as well as coupling between the antennas and 30 receive loops was measured on the bench. Proper functioning and isolation of the receive loops was determined from the noise correlation matrix.

Simulation

Finite difference time domain simulations (Sim4Life, Zurich Med Tech, Zurich) were performed to evaluate transmit efficiency and RF safety limits of the setup assuming full decoupling to the receiver coils (see Supplementary file CoilModel.smash). These simulations were also performed on three adjusted human models of Ella of the virtual family[24] where the breasts were replaced by breast models, to better correspond to the breast shape in prone position[14,25]. The breast models were segmented from T_1-weighted scans performed at 7 T with and without fat suppression from three volunteers with

different breast sizes (small/medium/large) to account for differences in coil loading. Scan parameters were: FFE, TR = 4.4 ms, TE = 1.91 ms, flip angle = 8^0, sensitivity encoding (SENSE[26]) 4x2 (RLxFH), field of view (FOV) = 160x350x160 mm^3, voxel size = 0.7x0.7x0.7 mm^3. For the fat suppressed image the same parameters were used including a 1-3-3-1 binomial spectral spatial RF pulse for fat suppression. Glandular tissue and fat tissue were segmented using iSeg (Medical Image Segmentation Tool Set, Zurich Med Tech, Zurich) and the corresponding dielectric permittivity and conductivity were assigned. The worst-case SAR was calculated as the maximum sum of the modulus of all quality matrix (Q-matrix) entries[27], yielding the worst-case SAR for an equal input power of 1 W on every channel. This value was used to derive average power limits per transmit channel for imaging applications, based on a 10g-averaged SAR limit of 20 W/kg in the trunk for the first level controlled mode[28]. Safety simulations that were performed for this coil are validated by means of comparing measured and simulated B_1^+ maps. Worst-case SAR values are used to determine safe power limits resulting in conservative SAR estimates.

Measurements

Safe average power limits were derived from simulations. Several safety measures are implemented on the scanner system in order to assure a duty cycle in which the defined average power is never exceeded. A safety check is executed before every scan, checking the TR and the necessary peak power and comparing the resulting average power against the power limit that is set in the software. Additionally, continuous power measurements are conducted during the scan with the directional couplers to ensure that average power limits are not exceeded. RF pulse width and duty cycle differ per sequence, but are forced to never exceed the average power limit.

After informed consent, two healthy female volunteers were scanned. For both volunteers, the phases and amplitudes of the individual transmit channels were optimized to obtain a uniform signal in the breast (RF-shimming)[1,29]. For this purpose, spoiled gradient echo images were acquired at a low flip angle for every single transmit channel. Magnitude and phase results were exported to a post processing tool (Matlab, Mathworks, Natick USA). This tool is used to combine the single transmit channel images into a 'shimmed' combined image using different amplitudes and phases for every transmit channel. A region of interest (ROI) was drawn in the breast, after which a constrained minimization was used to optimize the channel weights. The goal of this procedure was to minimize the coefficient of variation in the ROI, while maintaining

a minimum threshold of 40% and a maximum threshold of 100% for the drive amplitude. To assess the B_1^+ performance of the coil, a B_1^+ map was acquired using the dual refocusing echo acquisition mode method (DREAM[30]) with a nominal B_1 of 12 µT. For the B_1^+ map acquisition, RF-shimming resulted in a peak input power of 710 W per channel except for channel 3 (middle antenna), which was driven at 126 W. Additional scan parameters were: TR = 7.0 ms, TE = 1.97 ms and 2.4 ms, flip angle = 10^0 and 60^0, slice spacing = 21 mm, FOV = 320x520x60 mm³ with a resolution of 3.0x5.0x6.0 mm³. This acquired B_1 map was compared to a simulated B_1 map with the identical excitation phase and amplitude per channel to validate the EM simulations. The mean B_1^+ and coefficient of variation (= standard deviation/mean) has been calculated in two ROIs: the first (ROI1) includes both breasts to the pectoralis muscle boundary, and the second (ROI2) has been set for the entire field of view measured, including the pectoral muscle and reaching into the axilla.

Parallel imaging performance was investigated for the SENSE algorithm[26] and represented by geometry factor (g-factor) maps. ReconFrame (Gyrotools Ltd., Zürich, Switzerland) was used to calculate g-factor maps for different acceleration factors from R=1 to R=4 in the right-left (RL) direction and R=1 to R=3 in anterior-posterior (AP) direction by reconstructing the image undersampling in k-space. SNR maps were calculated in SNR units[31,32].

To show the clinical feasibility, a 3D T_1-weighted image was acquired (FFE, TR = 7.14 ms, TE = 3.23 ms, flip angle = 8^0, nominal B_1 = 9 µT, SENSE 4 x 2 (RL x FH), FOV = 160x351x160 mm³, resolution = 0.7x0.7x0.7 mm³) using a water selective 1-4-6-4-1 spectral spatial RF pulse for fat suppression in 111 seconds. Also, a single slice T_2-weighted turbo spin-echo (TSE) image (TR = 10000 ms; TE = 90 ms; echo-spacing = 10 ms; flip angle = 90^0; refocusing flip angle = 180^0; nominal B_1 = 12 µT; FOV = 250 x 421; resolution = 0.7x0.7x3 mm³; TSE factor = 17) was acquired in 2 min and 30 s.

Results

Hardware

Inter-element coupling between the dipole antennas is generally low. The maximum coupling of the transmit dipole array was -14.2 dB between element 4 and 5 while maximum reflection was -11.6 dB in element 3 (Figure 3A) for a representative subject. The maximum coupling of the transmit dipole with the receive loops without preamp

decoupling occurred between element 2 and receive loop 1 from the left cup and was -18.2 dB (Figure 3B). Noise correlation matrix of the 30 receive loops has a mean of 7.8 ± 8.7% with a maximum correlation of 52.9 % (Figure 3C).
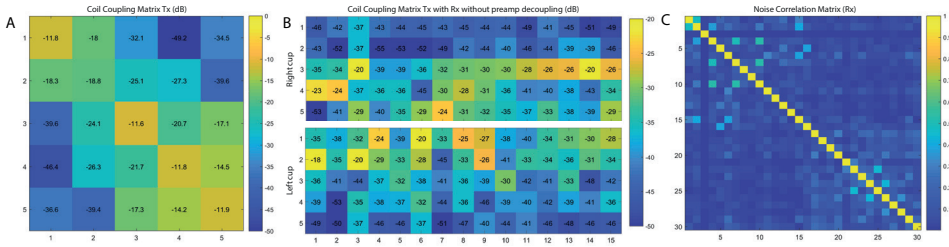

Figure 3 Inter-element coupling of the transmit dipole array with a maximum inter-element coupling of -14.2 dB in the top image **(A)**. Coil coupling matrix of the five dipole antennas with the receive loops of both cups with a maximum coupling of -18.2 dB in the middle image **(B)**. Noise correlation matrix of the 30 receive loops with a mean of 7.83 ± 8.69% with a maximum correlation of 52.9 % in the bottom image **(C)**.

Simulation

The maximum achievable local SAR value is 7.0 W/kg for 5x1 W accepted power (Figure 4) in the adjusted models Ella of the Virtual Family in prone position. Considering the local SAR limit of 20 W/kg in the trunk in first level controlled mode, an average power of 2.9 W/channel can be used at maximum.
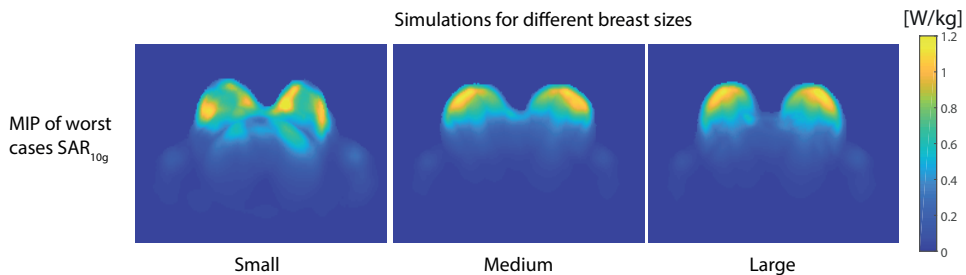

Figure 4 Simulation of maximum possible SAR distribution on Ella (virtual family) of the transmit elements with adapted breast models with different sizes (small/medium/large). The breast models were segmented from T1-weighted scans performed at 7 T with and without fat suppression with a previously build bilateral breast coil. Colorbar indicates the local 10g averaged SAR (W/kg).

Measurements

The acquired DREAM B_1^+ map (Figure 5) shows that with successful RF-shimming, the transmit fields of the antennas penetrate through the breasts completely. The magnitude of the transmit field also remains relatively homogeneous throughout the breast, within ROI1 a mean B_1^+ of 0.12 μT/√W, coefficient of variation of 20% and in ROI2 a mean B_1^+ of 0.11 μT/√W, coefficient of variation 27% (Figure 5). Good correspondence between the measured B_1^+ and the simulated B_1^+ was found with a mean root mean square (RMS) of 14.2% (Figure 5).
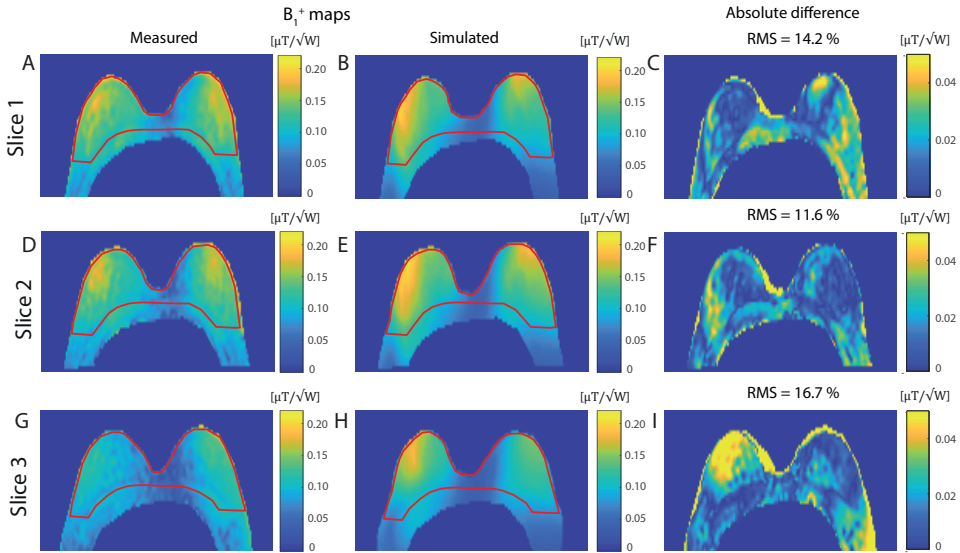

Figure 5 Three transversal slices of the measured B_1^+ map (same volunteer as 'small' in Figure 4) compared to the simulated B_1^+ map with the same shim settings resulting in the absolute difference map with a mean root mean square (RMS) of 14.2%. The measured B_1^+ map was acquired with the DREAM method (TR = 7.0 ms; TE = 1.97 ms and 2.4 ms; flip angle = 10° and 60°, FOV = 320x520x60 mm³ with a resolution of 3.0x5.0x6.0 mm³ with a nominal B_1 of 12 μT). The mean B_1^+ has been measured in two ROIs in the measured B_1 map, where ROI1 includes both breasts to the pectoralis muscle boundary (shown in red) and ROI2 has been set for the entire field of view shown (including the pectoral muscle and reaching into the axilla). Within ROI1 a mean B_1^+ of 0.12 μT/√W, coefficient of variation of 20% was measured and in ROI2 a mean B_1^+ of 0.11 μT/√W , coefficient of variation 27%.
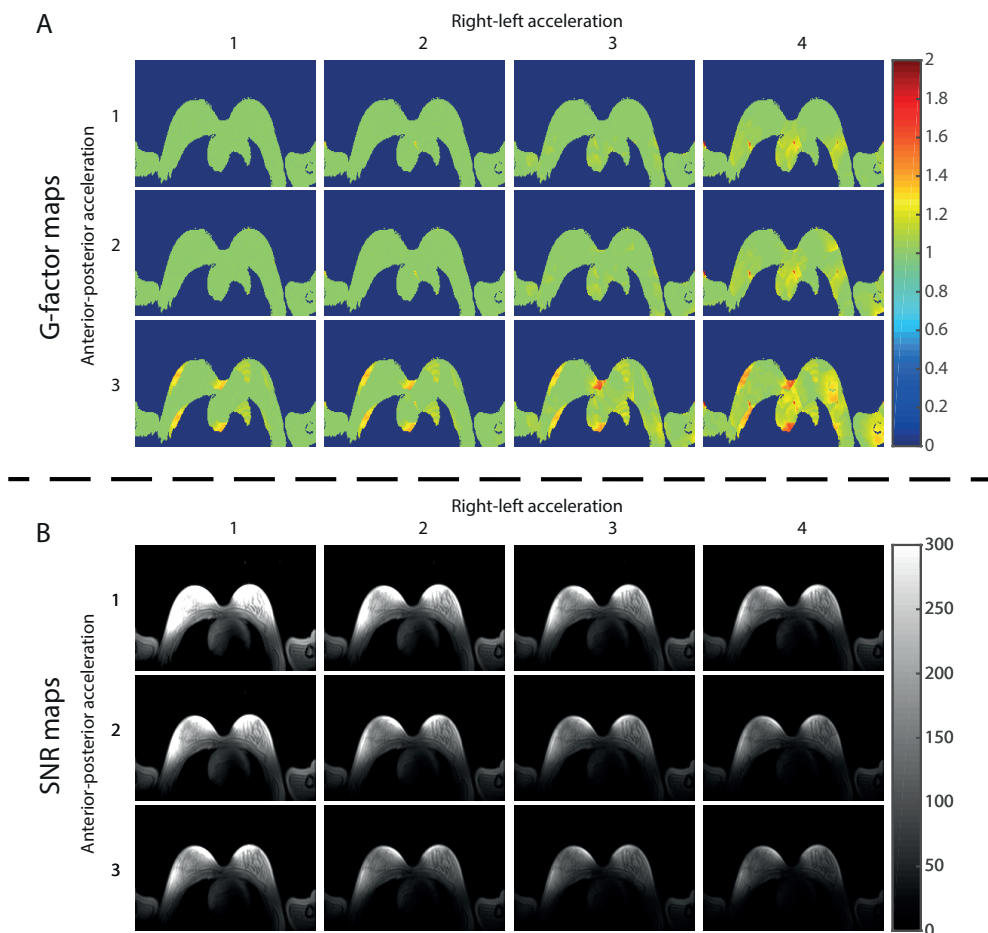
Figure 6 A transversal slice of g-factor maps with different acceleration factors in right-left direction and anterior-posterior direction for the receive chain (above the dotted line; A) and the corresponding SNR maps in SNR units below the dotted line (B).

The g-factor maps for different acceleration factors for the receive loops are displayed in Figure 6A. High g-factors (g-factor ≥ 2.0) start to appear for acceleration factors higher than R=4 in RL direction and R=3 in AP direction. However, the average g-factor is only 1.11 when moving to an acceleration factor of R=4x3, with a maximum g-factor of 1.87 near the heart. SNR decreases accordingly with increasing acceleration factors (Figure 6B).

We were able to acquire ultra-high resolution 3D fat suppressed T_{1w} images in 111 seconds (Figure 7A). Good fat suppression is achieved throughout the whole breast. A very high acceleration factor of R=8 was used, compromising the SNR achieved in the axilla, yet

high details can be observed in the glandular tissue. Also a T_{2w} TSE image (Figure 7B) was acquired with clear contrast between fat tissue and glandular tissue. Note that the lymph nodes in the axilla can be observed as hypo-intense spots.

Figure 7 Examples of clinical scans acquired with the coil. The top image (A) shows a transversal slice of a fat suppressed T1 weighted image (TR=7.1ms; TE=3.2ms; flip angle=8°; resolution of 0.7 mm3; SENSE 4x2 (RLxFH), 1-4-6-4-1 spectral spatial RF pulse for fat suppression). Total acceleration of R=8 was used, compromising the SNR achieved in the axilla, yet high details can be observed in the glandular tissue. The bottom image (B) shows a transverse T2 weighted TSE image (TR=10000ms; TE=90ms; flip angle=90°; resolution=0.7x0.7x3mm3; TSE factor=17). Note the lymph nodes in the axilla depicted as hypo-intense spots indicated by the white arrows.

Discussion

We demonstrated a new breast coil design using a multi-transmit system and five meandering dipole antennas around the breasts in combination with 30 receive loops. With this setup we were able to achieve a relatively homogeneous B_1^+ throughout the breast. However, the assessment of homogeneity in superior-inferior direction can be improved as only three slices were obtained around the center of the breasts. Previously presented coils[7,9-14] show that penetration depth is often limited to the pectoral muscle. However, it is important for clinical breast imaging that lymph nodes inside the axilla are visible on the images as well. With the use of meandering dipole antennas in this setup, we were able to acquire images at a large FOV due to the high penetration depth of the antennas. The achieved B_1^+ and homogeneity allowed us to acquire bilateral T_2w images of the breasts which was impossible with other bilateral designs at 7T so far, yet crucial for clinical practice. Only a single slice for the T_2w image could be acquired within the SAR limits in this study. Future work will include an optimization of the T_2w sequence in terms of TR and RF pulses in order to acquire more slices in the same time which has already been shown in the prostate[33].

Simulation of the breast coil ensured patient safety, however worst-case SAR values were used to determine safe power limits resulting in a conservative SAR estimate. Future work will focus on the application of more realistic SAR levels which will require a study of the inter-subject variability and further validation efforts using deep learning[34].

In this study, the worst case SAR assessment assumes equal and unitary input power on every transmit channel. In our current safety procedure, power limits are defined on a per channel basis. In the case that amplitude shimming is applied, the drive amplitude of a single channel will be scaled down except the power limit will stay the same. This ensures conservative setting for the power limits, in which SAR can never exceed the SAR as calculated in our models.

After impedance matching of the antenna array, worst case inter-element coupling of -14.2 dB and a worst case reflection coefficient of -11.7 dB are demonstrated. Although it is possible to improve the worst case reflection coefficient for a single subject, a tradeoff between robustness to load and an excellent reflection coefficient had to be chosen, leading to the current performance. The measured noise matrix showed good isolations between the receiver array channels and the measured g-factor maps showed the feasibility of parallel imaging with the developed RF array system. High

acceleration factors, up till an acceleration of R=4x3 (RLxAP direction) were achieved while preserving image quality as no unfolding artefacts within the breast were observed (Figure 5). The g-factor maps do show higher g-factors appearing in the axilla and in the arms of the volunteer. This is due to the fact that the receive loops are located around the breasts and do not receive signal originating from beyond the breast while the meandering dipole antennas have a much larger penetration depth. The optimal way to avoid signal loss is to combine the signals from loops and antennas in reception, resulting in a total of 35 receive elements. Unfortunately, the MR system architecture currently does not allow more than 32 element receive at the moment.

The currently proposed transmit setup places 5 dipole antennas at the anterior side of the subject. Commonly used 7T body transmit setups use 8 elements placed concentrically around the subjects. It would be possible to place additional transmit elements at the posterior side of the subject. However, it is demonstrated in this work that the current setup has sufficient penetration depth to cover the entire breasts. Adding more antennas at the posterior side of the subject can result in SAR peaks in the back muscles, and would add to the overall complexity of the setup, therefore it was not considered for this coil array.

The decoupling value between the transmit antennas and the receive loops of -18 dB is measured without the presence of pre-amplifier decoupling. Therefore, the actual decoupling is estimated to be below -25 dB which is sufficient to protect the preamps during transmit. All scattering parameters remain well below -10 dB, indicating that more than 90% of the emitted power is accepted and therefore 95% of the potential B_1^+ is reached. Additional reduction in reflection may be obtained but would provide at maximum only a few percent additional B_1^+ and was therefore left for some future improvement cycle.

An often occurring challenge with breast imaging at 7T is dealing with the inhomogeneity of B_1^+; decreasing from the nipple towards the pectoral muscle. In our bilateral coil setup, the position and the penetration depth of the antennas creates a homogenous B_1^+ in anterior to posterior direction throughout the breasts (coefficient of variation of 20% within the breasts; ROI1 in Figure 5). Though hard to compare with other work, Kim et al.[10] reported a coefficient of variation of 22% for one transversal slice and 31% in the entire volume, where Brown et al.[15] reported a coefficient of variation of 24% in one transversal slice. The observed inhomogeneity in right-left direction is probably due to interference of the B_1^+ fields of the different antenna elements. We have observed this

5

asymmetry in all the volunteers and therefore we think this is independent of the breast size. To achieve a more homogeneous B_1^+ throughout both breasts, more advanced calibration of the transmit fields is necessary, yet RF shimming only cannot solve this problem. Adding more antennas to the coil array may help to increase uniformity in right-left direction. Next to that, tailored RF pulses may be able to compensate for the B_1^+ inhomogeneity such as tilt optimized flip uniformity pulses[35] or tailored excitation in 3D with spiral nonselective (SPINS) RF pulses[36]. A next step in breast imaging at 7T would be to incorporate tailored RF pulse designs into the clinical protocol.

Conclusion

We constructed a new breast coil with five meandering dipole antennas and 30 receive loops for 7T. The coil can generate sufficient B_1^+ over a larger FOV in the breasts, which makes it possible to acquire T_2 weighted images and to image the axillary lymph nodes. This is an important step towards translating routinely used breast imaging protocols from 3T to 7T, whilst benefitting from the increased spectral and spatial resolution at 7T.

References

1. Metzger GJ, Snyder C, Akgun C, Vaughan T, Ugurbil K, Van De Moortele PF. Local B1+ shimming for prostate imaging with transceiver arrays at 7T based on subject-dependent transmit phase measurements. *Magn Reson Med*. 2008;59(2):396-409. doi:10.1002/mrm.21476.

2. Van Den Bergen B, Van Den Berg CAT, Klomp DWJ, Lagendijk JJW. SAR and power implications of different RF shimming strategies in the pelvis for 7T MRI. *J Magn Reson Imaging*. 2009;30(1):194-202. doi:10.1002/jmri.21806.

3. Niendorf T, Paul K, Oezerdem C, Graessl A, Klix S, Huelnhagen T, Hezel F, Rieger J, Waiczies H, Frahm J, Nagel AM, Oberacker E. W(h)ither human cardiac and body magnetic resonance at ultrahigh fields?technical advances , practical considerations , applications , and clinical opportunities. *NMR Biomed*. 2016;29(9):1173-1197. doi:10.1002/nbm.3268.

4. Laader A, Beiderwellen K, Kraff O, Maderwald S, Wrede K, Ladd ME, Lauenstein TC, Forsting M, Quick H, Nassenstein K, Umutlu L. 1 . 5 versus 3 versus 7 Tesla in abdominal MRI : A comparative study. 2017:1-18.

5. Cui J, Bosshard JC, Rispoli J V., Dimitrov IE, Cheshkov S, McDougall MP, Malloy C, Wright SM. A Switched-Mode Breast Coil for 7 T MRI Using Forced-Current Excitation. *IEEE Trans Biomed Eng*. 2015;62(7):1777-1783. doi:10.1109/TBME.2015.2403850.

6. By S, Rispoli J V., Cheshkov S, Dimitrov I, Cui J, Seiler S, Goudreau S, Malloy C, Wright SM, McDougall MP. A 16-channel receive, forced current excitation dual-transmit coil for breast imaging at 7T. *PLoS One*. 2014;9(11):1-16. doi:10.1371/journal.pone.0113969.

7. McDougall MP, Cheshkov S, Rispoli J, Malloy C, Dimitrov I, Wright SM. Quadrature transmit coil for breast imaging at 7 tesla using forced current excitation for improved homogeneity. *J Magn*

Reson Imaging. 2014;1173:1165-1173. doi:10.1002/jmri.24473.

8. Adriany G, Van De Moortele PF, Wiesinger F, Moeller S, Strupp JP, Andersen P, Snyder C, Zhang X, Chen W, Pruessmann KP, Boesiger P, Vaughan T, Ugurbil K. Transmit and receive transmission line arrays for 7 tesla parallel imaging. *Magn Reson Med*. 2005;53(2):434-445.

9. Klomp DWJ, Bank BL Van De, Raaijmakers A, Korteweg MA, Possanzini C, Boer VO, Cornelius AT, Berg V De, Bosch MAAJ Van De, Luijten PR. 31P MRSI and 1 H MRS at 7 T : initial results in human breast cancer. 2011;(January):1337-1342. doi:10.1002/nbm.1696.

10. Kim J, Santini T, Bae KT, Krishnamurthy N, Zhao Y, Zhao T, Ibrahim TS. Development of a 7 T RF coil system for breast imaging. *NMR Biomed*. 2017;30(1):1-10. doi:10.1002/nbm.3664.

11. Van de Bank BL, Voogt IJ, Italiaander M, Stehouwer BL, Boer VO, Luijten PR, Klomp DWJ. Ultra high spatial and temporal resolution breast imaging at 7T. *NMR Biomed*. 2013;26(4):367-375. doi:10.1002/nbm.2868.

12. Umutlu L, Maderwald S, Kraff O, Theysohn JM, Kuemmel S, Hauth EA, Forsting M, Antoch G, Ladd ME, Quick HH, Lauenstein TC. Dynamic Contrast-Enhanced Breast MRI at 7 Tesla Utilizing a Single-loop Coil. A Feasibility Trial. *Acad Radiol*. 2010;17(8):1050-1056. doi:10.1016/j.acra.2010.03.017.

13. Italiaander M, Nijholt PJ, Kraff O, Raaijmakers A, Stehouwer BL, Luijten PR, Klomp DWJ. High B1 dutycycle in bilateral breast imaging at 7T. *Proc Intl Soc Mag Reson Med 20*. 2012;20:2012.

14. Van Der Velden TA, Italiaander M, Van Der Kemp WJM, Raaijmakers AJE, Schmitz AMT, Luijten PR, Boer VO, Klomp DWJ. Radiofrequency configuration to facilitate bilateral breast 31P MR spectroscopic imaging and high-resolution MRI at 7 Tesla. *Magn Reson Med*. 2015;74(6):1803-1810. doi:10.1002/mrm.25573.

15. Brown R, Storey P, Geppert C, McGorty K, Klautau Leite AP, Babb J, Sodickson DK, Wiggins GC, Moy L. Breast MRI at 7 Tesla with a bilateral coil and robust fat suppression. *J Magn Reson Imaging*. 2014;39(3):540-549. doi:10.1002/jmri.24205.

16. Brown R, Storey P, Geppert C, McGorty K, Leite APK, Babb J, Sodickson DK, Wiggins GC, Moy L. Breast MRI at 7 Tesla with a bilateral coil and T1-weighted acquisition with robust fat suppression: Image evaluation and comparison with 3 Tesla. *Eur Radiol*. 2013;23:2969-2978. doi:10.1007/s00330-013-2972-1.

17. Vaughan JT, Snyder CJ, DelaBarre LJ, Bolan PJ, Tian J, Bolinger L, Adriany G, Andersen P, Strupp J, Ugurbil K. Whole-body imaging at 7T: Preliminary results. *Magn Reson Med*. 2009;61(1):244-248.

18. Raaijmakers AJE, Ipek O, Klomp DWJ, Possanzini C, Harvey PR, Lagendijk JJW, Van Den Berg CAT. Design of a radiative surface coil array element at 7 T: The single-side adapted dipole antenna. *Magn Reson Med*. 2011;66(5):1488-1497. doi:10.1002/mrm.22886.

19. Raaijmakers AJE, Luijten PR, van den Berg CAT. Dipole antennas for ultrahigh-field body imaging: a comparison with loop coils. *NMR Biomed*. 2016;29(9):1122-1130. doi:10.1002/nbm.3356.

20. Raaijmakers AJE, Italiaander M, Voogt IJ, Luijten PR, Hoogduin JM, Klomp DWJ, Van Den Berg CAT. The fractionated dipole antenna: A new antenna for body imaging at 7 Tesla. *Magn Reson Med*. 2016;75(3):1366-1374. doi:10.1002/mrm.25596.

21. Wiggins GC, Lakshmanan K, Chen G. The Distributed Inductance Electric Dipole Antenna. *Proc 23rd Annu Meet Int Soc Magn Reson Med*. 2015;23:3100.

22. Steensma BR, Obando AV, Klomp DWJ, van den Berg CAT, Raaijmakers AJE. Body imaging at 7 tesla with much lower SAR levels: an introduction of the Snake Antenna Array. In: *Proc. Intl. Soc. Mag. Reson. Singapore*. ; 2016.

23. Zhu Y, Alon L, Deniz CM, Brown R, Sodickson DK. System and SAR characterization in parallel RF

5

transmission. *Magn Reson Med*. 2012;67(5):1367-1378. doi:10.1002/mrm.23126.

24.   Christ A, Kainz W, Hahn EG, Honegger K, Zefferer M, Neufeld E, Rascher W, Janka R, Bautz W, Chen J, Kiefer B, Schmitt P, Hollenbach H-P, Shen J, Oberle M, Szczerba D, Kam A, Guag JW, Kuster N. The Virtual Family-development of surface-based anatomical models of two adults and two children for dosimetric simulations. *Phys Med Biol*. 2010;55(2):N23-N38. doi:10.1088/0031-9155/55/2/N01.

25.   Rispoli J V., Wright SM, Mallow CR, McDougall MP. Automated modification and fusion of voxel models to construct body phantoms with heterogeneous breast tissue: Application to MRI simulations. *J Biomed Graph Comput*. 2017;7(1):86-168.

26.   Pruessmann KP, Weiger M, Scheidegger MB, Boesiger P. SENSE: Sensitivity encoding for fast MRI. *Magn Reson Med*. 1999;42(5):952-962.

27.   Meliado E, Raaijmakers A, Luijten P, van den Berg C. Fast method to get an upper bound of the maximum SAR10 g for body coil arrays. In: *Proceedings International Society for Magnetic Resonance Imaging in Medicine, Benelux Chapter, Tilburg*. ; 2017:70.

28.   International Electrochemical Commission. Medical electrical equipment: part 2-33. Particular requirements for the safety of magnetic resonance equipment for medical diagnosis. *IEC 60601-2-33*. 2010:ed 3.0. (Geneva: IEC) Consolidated with amendments. doi:10.5594/J09750.

29.   Van De Moortele P-F, Snyder C, Delabarre L, Adriany G, Vaughan T, Ugurbil K. Calibration Tools for RF Shim at Very High Field with Multiple Element RF Coils: From Ultra Fast Local Relative Phase to Absolute Magnitude B1+ Mapping. In: *Proc. Intl. Soc. Mag. Reson. Med.* Vol 15. ; 2007:1676.

30.   Nehrke K, Börnert P. DREAM-a novel approach for robust, ultrafast, multislice B1 mapping. *Magn Reson Med*. 2012;68(5):1517-1526. doi:10.1002/mrm.24158.

31.   Kellman P, Mcveigh ER. Image reconstruction in SNR units: A general method for SNR measurement. *Magn Reson Med*. 2005;54(6):1439-1447. doi:10.1002/mrm.20713.Image.

32.   Kellman P. Erratum to Kellman P, McVeigh ER. Image reconstruction in SNR units: a general method for SNR measurement. *Magn Reson Med*. 2007;58:211-212. doi:10.1002/mrm.21261.

33.   Maas MC, Vos EK, Lagemaat MW, Bitz AK, Orzada S, Kobus T, Kraff O, Maderwald S, Ladd ME, Scheenen TWJ. Feasibility of T2-weighted turbo spin echo imaging of the human prostate at 7 tesla. *Magn Reson Med*. 2014;71(5):1711-1719. doi:10.1002/mrm.24818.

34.   Meliado EF, Raaijmakers AJE, Savenaije MHF, Luijten PR, van den Berg CAT. On-line subject specific local SAR assessment by deep learning. In: *Proc. Int. Soc. Mag. Reson. Med. 26*. ; 2018.

35.   Van Kalleveen IML, Boer VO, Luijten PR, Klomp DWJ. Tilt optimized flip uniformity (TOFU) RF pulse for uniform image contrast at low specific absorption rate levels in combination with a surface breast coil at 7 Tesla. *Magn Reson Med*. 2015;74(2):482-488. doi:10.1002/mrm.25415.

36.   Malik SJ, Keihaninejad S, Hammers A, Hajnal J V. Tailored excitation in 3D with spiral nonselective (SPINS) RF pulses. *Magn Reson Med*. 2012;67(5):1303-1315. doi:10.1002/mrm.23118.

5

Summary and general discussion

6

Summary

Over the past decades, women with breast cancer are increasingly treated with systemic therapy, in particular with neoadjuvant chemotherapy (NAC). Unfortunately, patients undergoing NAC treatment experience side effects, due to the fact that chemotherapy drugs target all cells in the body that grow and divide rapidly. On top of that, in ~30% of the patients, NAC treatment does not result in tumor size reduction. At the moment there is no non-invasive method to evaluate the early effects of systemic treatment. We hypothesized that metabolic changes will take place prior to morphological changes of the tumor, especially early on in the course of NAC treatment. Therefore, the overall aim of this thesis was to evaluate early effects of NAC treatment in breast cancer patients using metabolic MRI.

The first part of this thesis shows that we are able to measure metabolic changes after the first cycle of NAC treatment. In **Chapter 2,** metabolic ratios measured with ^{31}P-MRSI were correlated to the pathological response. The PMEs and PDEs are known to be important in anabolism and catabolism of the cell membrane. In tumor tissue, the amount of PMEs exceeds the amount of PDEs (1), and therefore it was hypothesized that in case of successful treatment the PME/PDE ratio decreases. In a small group of patients, it indeed appeared that the PME/PDE ratio in partial and complete responders decreased after the first cycle of NAC treatment and the non-responders showed an increase in the PME/PDE ratio. This shows the potential of using PME/PDE ratio as a biomarker for early prediction of non-response to NAC treatment in breast cancer patients.

In **Chapter 3**, a different contrast mechanism was used to acquire metabolic information about the tumor after the first cycle of NAC treatment. Changes in amide signals originating from amide protons attached to the backbone of proteins and peptides, were measured with CEST-MRI. These are of interest as tumors show increased amide signals compared to healthy tissue due to increased cellular proliferation and subsequent accumulation of defective proteins in tumors (2). Partial and complete responders showed a decrease in amide signal while non-responders showed an increase in amide signal. The latter observation possibly hints at a continuing increase in the concentrations of proteins and peptides since the tumor was not affected by NAC treatment.

The measured amide signal in **Chapter 3** is primarily related to the concentration of mobile amide protons, the exchange rate (influenced by tissue pH) with the bulk water and its T_1 relaxation time. The hypothesis is that the measured amide signal has a positive relation with exchange rate and amide content. From the ^{31}P-MRSI measurements described in **Chapter 2**, it is possible to determine intracellular pH based on the chemical shift of Pi (3). In **Chapter 4**, we correlated the amide signal measured with CEST-MRI to the pH measured with ^{31}P-MRSI. A correlation between amide signal and pH in the tumor was found in breast cancer patients. This correlation was opposite from the intrinsic relation between amide signal and pH (we found a negative relation rather than a positive relation). This demonstrates that the contribution of the concentration of mobile amide protons likely supersedes the influence of the exchange rate in the measured amide signal, assuming that the T_1 relaxation rate is not expected to differ significantly between different tumors. In fact, when correcting for the known intrinsic relation of amide signal with pH, the observed concentration range of mobile amides will be even higher. This also shows that ^{31}P-MRSI and CEST-MRI provide complementary information about the tumor emphasizing the importance of both techniques.

In the last part of this thesis in **Chapter 5**, first steps were taken to merge metabolic imaging with ultra-high resolution MRI of the breasts. A new bilateral breast coil setup was developed. Improved image quality for breast imaging at 7 T was achieved using five meandering dipole antennas in a multi-transmit setup, combined with a high density receive array. The coil generates sufficient B_1^+ over a larger FOV in the breasts. This makes it possible to acquire T_2-weighted images and to image the axillary lymph nodes, which has not been shown in previous studies at high field. The possibility of T_2-weighted imaging is a crucial step towards translating routinely used breast imaging protocols from 3 T to 7 T.

General discussion

Clinical usability

In the first part of this thesis (**Chapter 2 and 3**), ^{31}P-MRSI and CEST-MRI have shown great potential in measuring changes of tumor metabolism after the first cycle of NAC treatment in breast cancer patients. ^{31}P-MRSI provides information about anabolism and catabolism of the cell membrane, while CEST-MRI provides information about the concentration of mobile amide protons. It could be beneficial for the patients to

6

implement these techniques in standard clinical care. Because predicting the outcome of the NAC treatment could enable physicians to adjust systemic therapy regime, or expedite surgery and as such reduce toxicity and related costs of ineffective treatment. In our work, we demonstrated that the PME/PDE ratio from ^{31}P-MRS and amide signal from CEST-MRI are potential biomarkers to predict the response to NAC treatment after the first cycle of NAC. Remaining caveats in the techniques can be tackled to improve their predictive performance. For instance, CEST-MRI is sensitive to the B_1^+ field, since different exchanging groups are affected by the B_1^+. Variation in B_1^+ may cause more contrast from slower (or faster) exchanging species. The coil setup used in **Chapter 3** and **Chapter 4** consists of two quadrature coils placed in front of the breasts. A disadvantage of this design is the inhomogeneous transmit field towards the chest wall. Therefore, the first steps in resolving this issue were taken in **Chapter 5**, where the use of five dipole antennas have shown to be able to achieve a homogeneous transmit field reaching until the chest wall. CEST-MRI has not yet been implemented with this new breast coil, however an homogeneous transmit field will improve the quality of the APT maps of the breast.

This thesis showed the potential of the different biomarkers and potential of clinical breast MR examinations at 7 T. Future research has to focus on validating these biomarkers and implementing these techniques for standard clinical care after dealing with several practical considerations.

Practical considerations

First of all, the severe non-uniformities in the transmit field and limited penetration depth are the main reason why clinical breast imaging at 7 T is challenging. In a clinical MR examination, it is essential to have a homogenous transmit field and to image the axillary lymph nodes. The breast coil developed in **Chapter 5** addresses these challenges and makes it feasible to translate clinical protocols from 3 T to 7 T. This is mainly due to the fact that we were able to acquire bilateral T_2-weighted images, which has not been shown previously, yet essential for breast MR examinations in routine patient care. While in our studies, the RF and B_0-shimming was time-consuming (~10 minutes), fast automated RF and B_0 shim procedures are expected in the near future (4) when fusing the shim tools into the MRI console.

The next time-consuming part that may hinder adoption into clinical practice is the ^{31}P-MRSI scan at 7 T, which has a total scan time of 25:36 min. To gain more SNR, which can be exchanged into shorter scan time, the use of a ^{31}P body coil at 7 T combined with multiple receive elements for ^{31}P (5) could be highly beneficial (6). A body coil will generate a more homogeneous transmit field, making adiabatic pulses unnecessary, enabling shorter TR and via Ernst angle excitations an improved SNR in the same scan time. The use of local receive array coils could even speed up the acquisition by using parallel imaging techniques. Considering the quadratic relation between SNR and scan time, it is expected to bring down scan time within clinically acceptable scan times.

Availability of the technology to all patients may be considered when translating the protocol to clinically standard available 3 T MRI. However, the SNR will reduce substantially (3-5 fold, (7)) at 3 T compared to 7 T, which will unacceptably increase the scan time up to 3-10 hours to obtain the same SNR. Next to that, the increased spectral resolution obtained with 7 T is needed for ^{31}P-MRSI at this point to be able to detect the separate metabolites in the breast. Fortunately, due to FDA clearance on 7 T MRI it is expected that 7 T MRI with ^{31}P-MRSI will become more widely available in the near future.

Future perspective

Important acquisitions during a clinical breast MR examination, i.e. dynamic contrast-enhanced (DCE) series, and diffusion weighted imaging (DWI), have been implemented at 7 T (8,9) and were also acquired in the patients participating in our study. These were included to gain as much information as possible about the metabolic processes that take place in malignant transformation of cells which are also called "the hallmarks of cancer" (10). DCE-MRI can be used to perform pharmacokinetic modeling based on the contrast agent in the breast tissue. This gives detailed insights into underlying tumor angiogenesis by way of parameters relating to tumor perfusion and permeability. For example, the Tofts model (11) calculates pharmacokinetic measures of contrast agent extravasation, such as the transfer constant (K^{trans}) and the rate constant (k_{ep}). This is of interest in cancer because the vessels of fast growing tumor tissue become 'leaky'. K^{trans} and k_{ep} have the potential in aiding in predicting overall survival, disease-free survival, clinical and pathological response to therapy (12). It would be interesting to investigate the added value of K^{trans} and k_{ep} over ^{31}P-MRS and CEST-MRI in characterizing the tumors and the effect of treatment.

6

DWI relies on the diffusion properties of water in the tissue. The apparent diffusion coefficient (ADC) can be calculated which is interpreted as an indirect measure for cell density (13). Tumor ADC has a negative correlation with cellularity (14) and it can characterize (15) and grade primary breast tumors (16). It also has shown its potential to assess tumor response to therapy (17). While the ^{31}P-MRS exams give direct information on cell proliferation, the higher resolution of DWI may provide added value particularly for heterogeneous tumors where spatial resolution of ^{31}P-MRS is insufficient. Therefore, combining these biomarkers, with the biomarkers from **Chapter 2** and **Chapter 3** into a multi-parametric model may further improve prediction of the response to NAC treatment for the individual patient. Future research has to rule out whether this model has to be a combination of biomarkers from ^{31}P-MRSI and/or CEST-MRI and/or DCE-MRI and/or DWI.

The biomarkers in **Chapter 2** and **Chapter 3**, retrieved from ^{31}P-MRSI and CEST-MRI, were correlated to the pathological response defined according to the Miller-Payne system (18); complete response is classified as grade 5 and non-response as grade 1. To validate these biomarkers, more patients need to be included to obtain sufficient statistical power. Another way to achieve more statistical power, would be a linear outcome measure for the pathological response rather than 5 different grades. Recent technical developments regarding digital pathology allows to perform image analysis on pathology such as automatic segmentation, tumor cells count, characterization of lesions, etc. This way, a linear scale for evaluating pathological response to therapy could be developed which will increase understanding the relation between in vivo biomarkers with pathology markers. However, it needs to be considered that the in vivo biomarkers are obtained from the entire tumor and pathology often from a fraction of the tumor; particularly if only pre-therapy biopsies are taken from the tumor. As tumors are known to be heterogeneous, representation of the tumor by only one biopsy specimen is often discussed, so alternative end-points should be considered.

Technology advanced rapidly the last decades, including technical developments of MRI, both the software and the hardware side of the MR system. The coming years, research will continue to explore the full potential of 7 T MRI. This thesis is one of the pioneering works performed which resulted in the development of a new generation 7 T scanners, the so-called 'META-scan'. The goal is to develop a non-invasive metabolic imaging tool to observe physiology and metabolism of tissue in vivo. This will provide a more direct and faster measure to characterize diseases and responses to treatments in comparison to conventional morphologic imaging. The system will incorporate a

quintuple tuned body coil integrated in a whole body 7 tesla MRI system that facilitates imaging of the nuclei ^{1}H, ^{13}C, ^{19}F, ^{23}Na, and ^{31}P. As mentioned before, a body coil tuned to ^{31}P will result in higher SNR and faster scan times for ^{31}P-MRSI in breast cancer. Another issue not mentioned before, is the fact that with the current setup, during a breast MR examination at 7 T, a different coil setup (tuned the resonance of ^{31}P) has to be used for ^{31}P-MRSI. This leads to getting the patient in and out of the MR scanner during one examination which is very inconvenient for both the patient and the workflow. The META-scan in combination with a dual tuned breast receive coil (tuned to the resonance of ^{1}H and ^{31}P) will allow the combination of these techniques in one scan session without the need to switch coils and getting the patient in and out of the scanner. This will also speed up the process of integrating 7 T MRI in clinical practice in the future for breast cancer.

To conclude, this thesis presents the possibility of detecting altered tumor metabolism in breast cancer after the first cycle of NAC treatment and identified these biomarkers as promising predictors of pathological response. Also, technological advances in the form of a bilateral breast coil were presented, which makes it feasible to perform a routinely used clinical MR protocol at 7 T MRI. 7 T MRI has proven to be a powerful tool for assessment of tumor metabolism in breast cancer patients. Combining these techniques with morphological and physiological information, also obtained with MRI, a multiparametric assessment of breast tumors is feasible. Overall, this thesis presents the first steps towards routinely performed clinical breast MR examinations at 7 T and non-invasive early response prediction of NAC treatment in breast cancer patients.

References

1. Podo F. Tumour phospholipid metabolism. NMR Biomed. 1999;12(7):413–439.
2. Adams J. The proteasome: a suitable antineoplastic target. Nat Rev Cancer. 2004;4(5):349–360.
3. Moon RB, Richards JH. Determination of Intracellular pH by 31P Magnetic Resonance. J Biol Chem. 1973;248(25):7276–7278.
4. Ianni JD, Cao Z, Grissom WA. Machine learning RF shimming: Prediction by iteratively projected ridge regression. Magn Reson Med. 2018;(February):1–11.
5. Valkovič L, Dragonu I, Almujayyaz S, et al. Using a whole-body 31P birdcage transmit coil and 16-element receive array for human cardiac metabolic imaging at 7T. PLoS One. 2017;12(10):e0187153.
6. Löring J, van der Kemp WJM, Almujayyaz S, van Oorschot JWM, Luijten PR, Klomp DWJ. Whole-body radiofrequency coil for 31P MRSI at 7T. NMR Biomed. 2016;29(6):709–720.
7. Korteweg MA, Veldhuis WB, Visser F, et al. Feasibility of 7 Tesla Breast Magnetic Resonance Imaging Determination of Intrinsic Sensitivity and High-Resolution Magnetic Resonance

6

Imaging, Diffusion-Weighted Imaging, and 1H-Magnetic Spectroscopy of Breast Cancer Patients Receiving Neoadjuvant Therap. Invest Radiol. 2011;46(6):370–376.

8. Stehouwer BL, Klomp DWJ, van den Bosch M a a J, et al. Dynamic contrast-enhanced and ultra-high-resolution breast MRI at 7.0 Tesla. Eur Radiol. 2013;23(11):2961–2968.

9. Van Der Velden T a., Italiaander M, Van Der Kemp WJM, et al. Radiofrequency configuration to facilitate bilateral breast 31P MR spectroscopic imaging and high-resolution MRI at 7 Tesla. Magn Reson Med. 2015;74(6):1803–1810.

10. Hanahan D, Weinberg RA. Hallmarks of Cancer: The Next Generation. Cell. 2011;144(1):646–674.

11. Tofts PS, Brix G, Buckley DL, et al. Estimating Kinetic Parameters From Dynamic Contrast-Enhanced T1-Weighted MRI of a Diffusable Tracer: Standardized Quantities and Symbols. J Magn Reson Imag. 1999;10:223–232.

12. Li SP, Makris A, Beresford MJ, et al. Use of Dynamic Contrast- enhanced MR Imaging to Predict Survival in Patients with Primary Breast Cancer Undergoing Neoadjuvant Chemotherapy. Radiology. 2011;260(1):68–78.

13. Merboldt KD, Hanicke W, Frahm J. Self-diffusion NMR imaging using stimulated echoes. J Magn Reson. 1985;64(3):479–486.

14. Woodhams R, Matsunaga K, Iwabuchi K, et al. Diffusion-Weighted Imaging of Malignant Breast Tumors. J Comput Assist Tomogr. 2005;29(5):644–649.

15. Kul S, Eyuboglu I, Cansu A, Alhan E. Diagnostic efficacy of the Diffusion weighted imaging in the characterization of different types of breast lesions. J Magn Reson Imaging. 2014;40(5):1158–1164.

16. Costantini M, Belli P, Rinaldi P, et al. Diffusion-weighted imaging in breast cancer: Relationship between apparent diffusion coefficient and tumour aggressiveness. Clin Radiol. 2010;65(12):1005–1012.

17. Sharma U, Danishad KKA, Seenu V, Jagannathan NR. Longitudinal study of the assessment by MRI and diffusion-weighted imaging of tumor response in patients with locally advanced breast cancer undergoing neoadjuvant chemotherapy. NMR Biomed. 2009;22(1):104–113.

18. Ogston KN, Miller ID, Payne S, et al. A new histological grading system to assess response of breast cancers to primary chemotherapy : prognostic significance and survival. Breast. 2003;12:320–327.

6

Appendices

A

Nederlandse samenvatting

Borstkanker

Borstkanker (mammacarcinoom) is de meest voorkomende kanker in vrouwen wereldwijd en staat op nummer twee als de meest voorkomende doodsoorzaak voor vrouwen. In Nederland is zelfs de kans om borstkanker te krijgen 1 op 7. De meeste borsttumoren beginnen in de melkgang (ductaal carcinoom) en sommige beginnen in het klierweefsel (lobulair carcinoom). Daarnaast zijn er nog een aantal minder voorkomende mammacarcinomen.
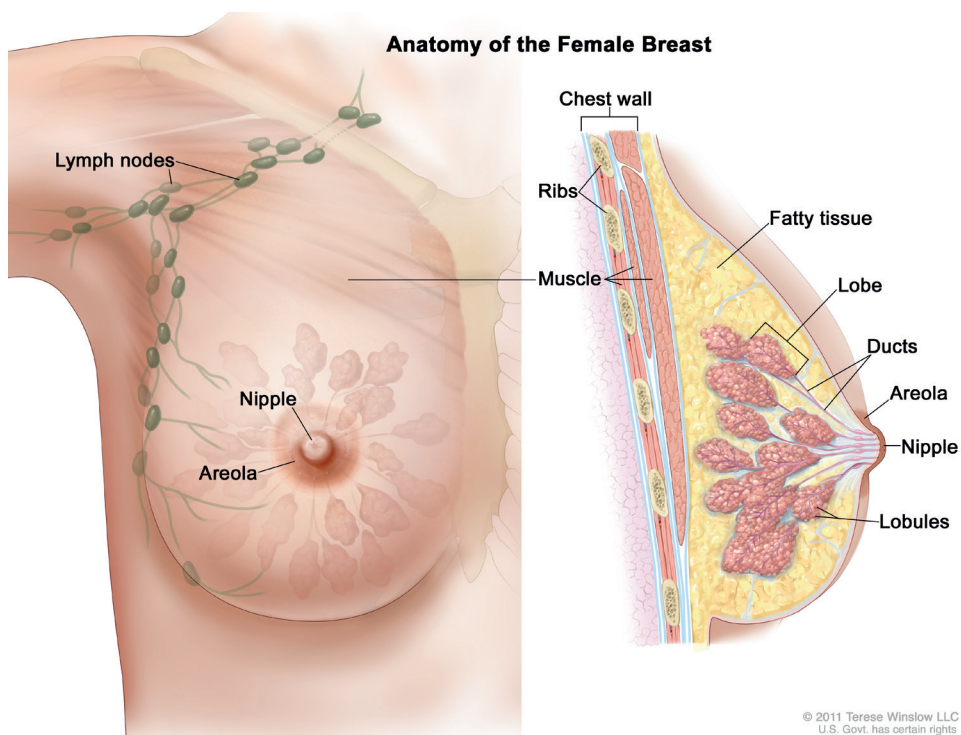
Figuur 1 De anatomie van de vrouwenborst. De tepel (nipple), tepelhof (areola) en lymfeklieren (lymph nodes) zijn links weergegeven en de binnenkant van de borst aan de rechterkant. Hierin zijn het klierweefsel (lobe), de melkgangen (duct) en het vetweefsel (fatty tissue) zichtbaar.

Borstkanker kan zich verspreiden/uitzaaien via de lymfeklieren of via de bloedsomloop naar de rest van het lichaam, wat een metastase genoemd wordt. De primaire uitzaaiingsorganen zijn bot, longen, lever en het brein. Wanneer iemand gediagnostiseerd wordt met borstkanker, zal het stadium van de borstkanker worden

bepaald. Stadiering van de borstkanker helpt bij het bepalen van de optimale behandeling voor de patiënt. Hierbij wordt het zogenaamde TNM (tumor, node, metastase) systeem gehanteerd:

- Tumor: grootte van de tumor en/of hoever de tumor is doorgegroeid in het weefsel eromheen.
- Nodes (lymfeklier): of en hoeveel uitzaaiingen er zijn in de lymfeklieren.
- Metastase: of er uitzaaiingen zijn in organen ergens anders in het lichaam.

Sinds 2018 zijn de deze criteria uitgebreid met de volgende karakteristieken van de tumor:

- Hormoongevoeligheid voor oestrogeen (ER) en progesteron (PR): of deze hormoonreceptoren aanwezig zijn in de tumor.
- Her2 status (human epidermal growth factor receptor 2): of de tumor te veel van het eiwit Her2 produceert.
- Tumor graad: mate waarin de tumorcellen afwijken van normale cellen.

Stadiering van de borstkanker kan variëren van stadium 0 (carcinoma in situ) tot stadium IV. Hoe hoger het stadium, hoe verder de tumor zich heeft uitgezaaid in het lichaam. Het stadium van de borstkanker wordt gebruikt om de prognose te voorspellen en de meest passende behandeling te bepalen.

Behandeling van borstkanker

In de afgelopen jaren zijn de ontwikkelingen snel gegaan op het gebied van levensreddende behandelingen voor borstkanker patiënten. Het primaire doel van therapie, is het zoveel mogelijk verwijderen van tumorcellen uit het lichaam en het tegengaan van terugkeren van de tumor. Het optimale behandelingsplan wordt bepaald in een multidisciplinair team van verschillende specialisten die een beslissing maken op basis van het stadium van de tumor, leeftijd, algehele gezondheid, status menopauze en de aanwezigheid van bekende erfelijke afwijkingen in de genen. De meest voorkomende behandelingen zijn (borstsparende) operatie, chemotherapie, hormoontherapie, radiotherapie en doelgerichte therapie, maar veel vaker bevat een behandeling een combinatie van deze verschillende therapieën. Het onderzoek dat beschreven staat in dit proefschrift richt zich op de behandelingseffecten van chemotherapie en dan met name neo-adjuvante chemotherapie (chemotherapie die een patiënt toegediend krijgt voorafgaand aan chirurgie).

A

Neoadjuvante chemotherapie

Neoadjuvante chemotherapie (NAC) wordt steeds meer gebruikt als preoperatieve behandeling, met het voornaamste doel om lokaal gevorderde (locally advanced) tumoren (beter) geschikt te maken voor chirurgische resectie. Lokaal gevorderde tumoren hebben één of meer van de volgende kenmerken:

- Grote afmeting (> 5 cm).
- Uitgezaaid in meerdere lymfeklieren in de oksel.
- Uitgezaaid naar andere soorten weefsels zoals de huid, spier of ribben.

Daarnaast staat er in de recente St. Gallen consensus beschreven er een voorkeur is om NAC te gebruiken in de HER2+ en triple negatieve borsttumoren (stadium II en III) en dat deze voorkeur is uitgebreid naar vrouwen die in aanmerking komen voor een borstsparende operatie.

Chemotherapie zijn medicijnen (cytostatica) die gericht zijn tegen cellen die snel groeien en delen, zoals tumorcellen. Chemotherapie werkt door je hele lichaam (systemische therapie) en heeft daarom ook effect op de celdeling van gezonde cellen die bijvoorbeeld te vinden zijn in haarzakjes, nagels, mond, verteringssysteem en beenmerg. Hierdoor zijn er vele (onaangename) bijwerkingen van chemotherapie. De meest gebruikte cytostatica zijn anthracyclines en taxanen. Anthracyclines beschadigen het DNA van kankercellen en verhinderen de reproductie. Taxanen stabiliseren en binden zich aan microtubuli (buisvormige eiwitstructuren) en verstoren de celstructuur waardoor de celdeling niet meer goed plaatsvindt.

Over het algemeen bestaat een chemotherapie behandeling uit meerdere kuren die voor een bepaalde tijd herhaald worden. Hierbij wordt vaak een mix van cytostatica gebruikt. De totale lengte van de behandeling hangt af van het type tumor, de omvang van de tumor en het soort cytostatica dat gegeven wordt, maar meestal duurt een gemiddelde behandeling tussen de drie en zes maanden (kan korter maar ook langer duren).

Een nadeel van NAC is dat in 31% van de patiënten niet het gewenste effect wordt behaald waardoor deze patiënten een stabiele of progressieve ziekte zullen behouden. Het probleem is echter het identificeren van deze patiënten voorafgaand aan de behandeling. Deze patiënten zullen namelijk alle nadelen (bijwerkingen) bevinden zonder enige voordeel van de behandeling te hebben. Het is daarom belangrijk om

zogenaamde biomarkers te vinden die dit vroegtijdig kunnen voorspellen. Hierdoor zou bijvoorbeeld het soort cytostatica aangepast kunnen worden gedurende de behandeling waardoor onnodige toxiciteit en gerelateerde kosten van een niet effectieve behandeling vermeden kunnen worden.

In de huidige klinische praktijk wordt tijdens de chemotherapie behandeling het effect bepaald op basis van veranderingen van de omvang van de tumor, gemeten met echo of MRI (magnetic resonance imaging). Echter verwachten we dat onderliggende veranderingen in het metabolisme veel eerder plaatsvinden dan veranderingen in de omvang van de tumor, waardoor het effect van de behandeling eerder en beter bepaald zou kunnen worden als we het metabolisme van de tumor in kaart brengen.

Pathologische respons

De pathologische respons op NAC wordt in dit proefschrift gedefinieerd volgens de Miller-Payne schaal. Dit wordt bepaald door de patholoog op het weefsel dat chirurgisch verwijderd wordt. Hierbij is geen respons op therapie geclassificeerd als graad 1 en een complete respons als graad 5. Geen pathologische respons betekent geen of enige wijziging van de tumorcellen, maar geen vermindering van de algehele cellulariteit vergeleken met het diagnostisch biopt (genomen voor de start van de therapie).

Metabole MRI van borstkanker

MRI is een beeldvormende techniek die niet meer weg te denken is uit de klinische praktijk. MRI maakt het mogelijk om non-invasief de anatomie en fysiologie in beeld te brengen met behulp van een grote sterke magneet rondom de patiënt. MRI wordt vaak gebruikt, naast mammografie en echo, als aanvullend onderzoek gedurende diagnostische work-up van borstkanker patiënten. De magneten van klinische scanners hebben typisch een veldsterkte van 1.5 T of 3 T. Het voordeel van een hogere veldsterkte is de verhoogde signaal-ruisverhouding (SNR) en hogere spatiële en temporele resolutie. Om informatie te vergaren over het metabolisme, is het gewenst om een zo hoog mogelijke SNR en contrast-ruisverhouding (CNR) te hebben. Daarom is het onderzoek in dit proefschrift uitgevoerd met een hoge veldsterkte van 7 T. Dit heeft voornamelijk voordelen bij de zogenaamde magnetic resonance spectroscopy (MRS).

MRS exploiteert het feit dat, dankzij afscherming van elektronen, een atoomkern resoneert op een iets andere frequentie afhankelijk van zijn positie binnen een molecuul. Hierdoor heeft elke molecuul met een nucleaire magnetische resonantie een specifieke

A

105

'fingerprint'. Op deze manier kunnen signalen afkomstig van verschillende moleculen gemeten en herkend worden met MRS. Een sterk magneetveld als 7 T zorgt voor een verhoogde spectrale resolutie, wat het mogelijk maakt om individuele metabolieten te onderscheiden van elkaar en te detecteren in de borst.

Metabole MRI is een verzamelnaam voor non-invasieve MRI technieken die nieuwe inzichten kunnen geven in het begrijpen van weefselmetabolisme in vivo. Onder deze technieken zijn fosfor spectroscopie (^{31}P-MRS) en chemical exchange saturation transfer (CEST) MRI. Deze technieken worden hieronder beschreven.

^{31}P-MRS

^{31}P-MRS maakt het mogelijk om metabolieten te meten die betrokken zijn bij het cel metabolisme. Voorbeelden hiervan zijn de phosphomonoesters (PME) en phosphodiesters (PDE) die een belangrijke rol spelen bij de aanmaak en afbraak van celmembranen. Verhoogde aanwezigheid van PME over PDE (PME/PDE ratio) is geassocieerd met de aanwezigheid van tumorcellen en met de mitotische telling (mate van deelsnelheid). Er is in een eerdere studie aangetoond dat veranderingen in deze ratio zichtbaar zijn na de derde chemokuur gedurende NAC (na ~ 3 maanden). Dit is nog steeds redelijk vergevorderd in de cycli van de NAC en daarom hebben we in dit proefschrift onderzocht of we met ^{31}P-MRS deze veranderingen ook al kunnen meten na de eerste chemokuur (na 2 weken).

CEST-MRI

Chemical exchange saturation transfer (CEST) MRI is potentieel een nog sensitievere techniek dan MRS en is veel onderzocht de afgelopen jaren. Het beeldcontrast in CEST-MRI is afhankelijk van de concentratie mobiele protonen, de uitwisselingssnelheid daarvan met het bulk water en de T_1 relaxatie tijd van water. Hierdoor kunnen endogene moleculen, die deze mobiele protonen hebben, indirect gemeten worden. Het meest gerapporteerde CEST effect is die van de uitwisseling van amide protonen (APT) die aanwezig zijn in eiwitten en peptiden. Het is aangetoond dat APT-CEST verschillen kan aantonen tussen tumoren en gezond weefsel. De laatste tijd wordt APT-CEST vaak gesuggereerd om als biomarker te gebruiken om de respons van therapie te monitoren in borstkanker patiënten. Daarnaast is het CEST effect afhankelijk van de zuurgraad van het weefsel en kan dus gebruikt worden als indirecte maat voor pH. APT-CEST is minder specifiek dan ^{31}P-MRS, maar een groot voordeel is dat deze techniek breder

ingezet kan worden, bijvoorbeeld ook op lagere veldsterktes die in de kliniek worden gebruikt. Voor ^{31}P-MRS daarentegen is het lastiger omdat er specifieke hardware (spoelen) voor nodig is die niet overal beschikbaar zijn.

Borstspoel

Bij een 7 T MRI scanner moet er gebruik gemaakt worden van lokale transmit spoelen omdat er geen bodycoil aanwezig is. Eén van de uitdagingen die bij een lokale transmit spoel komt kijken, is het aflopende transmit veld (B_1^+) verder verwijderd van de spoel (inhomogeen veld). Daarnaast wordt het field of view (FOV) beperkt. Voornamelijk om deze twee redenen wordt beeldvorming van de borsten op 7 T nog niet routinematig gebruikt in de kliniek. Eén van de klinische scans is namelijk een T_2-gewogen turbo spin echo (TSE) MRI die alleen goed werkt als er een homogeen veld is over de gehele borsten. Daarnaast is het nodig om de lymfeklieren in de oksel af te beelden voor de diagnose.

In dit proefschrift is daarom een nieuwe bilaterale borstspoel ontwikkelt voor 7 T MRI, waarbij gebruik is gemaakt van zogenaamde dipool antennes. Hierbij was het doel om een homogeen veld over de borsten te creëren en waarmee het afbeelden van de lymfeklieren in de oksel mogelijk was.

Doel proefschrift

Het doel van dit proefschrift is het evalueren van vroegtijdige effecten (na de eerste kuur) van neoadjuvante chemotherapie in borstkanker patiënten met metabole MRI.

In het eerste gedeelte van dit proefschrift hebben we laten zien dat het mogelijk is om veranderingen in het metabolisme te meten na de eerste cyclus van NAC. In **Hoofdstuk 2** hebben we metabole ratios gemeten met ^{31}P-MRS en gecorreleerd aan de pathologische respons. De PMEs en PDEs spelen een belangrijke rol bij de aanmaak en afbraak van celmembranen. In tumorweefsel is de concentratie PMEs hoger dan die van de PDEs. Daarom was de hypothese dat bij een succesvolle behandeling de PME/PDE naar beneden zou gaan. In een kleine groep patiënten hebben we laten zien dat het mogelijk is om veranderingen in deze ratio te meten en dat, net als de hypothese, PME/PDE in partiële en complete responders afnam. Dit werk laat de grote potentie zien om PME/PDE te gebruiken als biomarker om vroegtijdig het effect van NAC te voorspellen.

A

In **Hoofdstuk 3**, hebben we aangetoond dat het mogelijk is om verschillen te meten in het amide signaal met CEST-MRI na de eerste chemokuur. Dit signaal is afkomstig van de amide protonen die gebonden zijn aan eiwitten en peptiden. Dit is met name interessant omdat het is aangetoond dat in tumor weefsel een verhoogd amide signaal te meten is vergeleken met gezond weefsel. Dit komt door de verhoogde celdeling en de daaropvolgende opeenhoping van defecte eiwitten in tumoren. Partiële en complete responders lieten een afname zien van het amide signaal terwijl de non-responders een toename van het signaal lieten zien. Dit laatste hint naar een continue toename van eiwitten en peptiden aangezien de tumor niet werd beïnvloedt door de NAC behandeling.

Het gemeten amide signaal in **Hoofdstuk 3** is primair gerelateerd aan de concentratie van mobiele amide protonen, de uitwisselingssnelheid (beïnvloed door pH van het weefsel) met het bulk water en de T_1 relaxatie tijd van water. De uitwisselingssnelheid is positief gecorreleerd met pH en daardoor gaan we er van uit dat het gemeten amide signaal ook positief gerelateerd is aan de pH. Met de ^{31}P-MRS metingen uit **Hoofdstuk 2**, is het ook mogelijk om intracellulair pH te meten op basis van de chemische verschuiving (chemical shift) van anorganisch fosfaat (Pi). Hiermee hebben we in **Hoofdstuk 4** een lineaire correlatie gevonden tussen het amide signaal en de pH. Deze correlatie was echter in tegengestelde richting als de hypothese, namelijk een negatieve relatie tussen de twee. Er van uitgaande dat de T_1 tussen verschillende tumoren niet veel afwijkt en daardoor het minste effect heeft op het amide signaal, laat deze data zien dat hoogstwaarschijnlijk de grootste bijdrage aan het amide signaal afkomstig is van de concentratie mobiele amide protonen. Dit suggereert dat we de gemeten concentratie van de amide protonen onderschatten met CEST-MRI.

In het laatste gedeelte van dit proefschrift in **Hoofdstuk 5**, hebben we de eerste stappen gezet om metabole beeldvorming met ultrahoog resolute MRI van de borsten samen te voegen. Hiervoor hebben we een bilaterale borstpoel ontwikkeld. Met deze setup was het mogelijk om verbeterde beelden te verkrijgen. Er is gebruik gemaakt van vijf dipool antennes rondom de borsten in combinatie met een hoge densiteit van ontvangstloops die aangesloten waren op een multi-transmit systeem. De spoel genereert voldoende B_1^+ over een groter FOV waardoor het mogelijk is om nog niet eerder vertoonde bilaterale T_2-gewogen TSE op te nemen en de lymfeklieren in de oksel af te beelden. De mogelijkheid om deze beelden te maken met deze spoel zijn een cruciale stap richting het overzetten van een klinisch protocol van 3 T naar 7 T.

Dit proefschrift laat zien dat het mogelijk is om veranderingen in tumor metabolisme te meten in borstkanker patiënten na de eerste cyclus van NAC. De biomarkers die beschreven zijn, zijn veelbelovend om te gebruiken voor het voorspellen van de pathologische respons. Daarnaast hebben we technologische ontwikkelingen laten zien in de vorm van een bilaterale borstspoel waarmee het mogelijk is om een klinisch borstprotocol te draaien voor 7 T MRI. Een combinatie van deze technieken met morfologische en fysiologische informatie kan leiden tot een multiparametrisch model die mogelijk de respons op NAC kan voorspellen voor de individuele patiënt.

A

Publication list

Scientific publication

Krikken E, van der Kemp WJM, van Diest PJ, van Dalen T, van Laarhoven HWM, Luijten PR, Klomp DWJ, Wijnen JP, Early detection of changes in phospholipid metabolism during neoadjuvant chemotherapy (NAC) in breast cancer patients using phosphorus magnetic resonance spectroscopy at 7 tesla, NMR in Biomed. 2019;e4086. https://doi.org/10.1002/nbm.4086.

Krikken E, Khlebnikov V, Zaiss M, Jibodh RA, van Diest PJ, Luijten PR, Klomp DWJ, van Laarhoven HWM, Wijnen JP, Amide chemical exchange saturation transfer at 7 T: A possible biomarker for detecting early response to neoadjuvant chemotherapy in breast cancer patients, Breast Cancer Research (2018);20:51.

Krikken E, van der Kemp WJM, Khlebnikov V, van Dalen T, Los M, van Laarhoven HWM, Luijten PR, van den Bosch MAAJ, Klomp DWJ, Wijnen JP, Contradiction between amide-CEST signal and pH in breast cancer explained with metabolic MRI, NMR in Biomed. 2019; *in press.*

Krikken E, Steensma BR, Voogt IJ, Luijten PR, Klomp DWJ, Raaijmakers AJE, Wijnen JP, Homogeneous B1+ for bilateral breast imaging at 7 T using a five dipole transmit array merged with a high density receive loop array. NMR Biomed. 2018;(October):e4039. http://doi.wiley.com/10.1002/nbm.4039.

Conference proceedings

Krikken E, Khlebnikov V, Zaiss M, Jibodh RA, van Diest PJ, Luijten PR, Klomp DWJ, van Laarhoven HWM, Wijnen JP, Amide chemical exchange saturation transfer at 7 T: A possible biomarker for detecting early response to neoadjuvant chemotherapy in breast cancer patients, ISMRM 26th Annual Meeting, Paris, France, June 16-21, 2018 (oral presentation)

Krikken E, Steensma BR, Voogt IJ, Huijing ER, Klomp DWJ, Wijnen JP, Raaijmakers AJE, Higher and more homogeneous B_1^+ for bilateral breast imaging at 7T using a multi-transmit setup with 5 dipole antennas and a 30-loop element receive array, ISMRM 26th Annual Meeting, Paris, France, June 16-21, 2018 (oral presentation)

Krikken E, van der Kemp WJM, Luijten PR, Gilhuijs KGA, Klomp DWJ, van Laarhoven HWM, Wijnen JP, In vivo ^{31}P-MRS of triple negative breast cancer patients, ISMRM 26th Annual Meeting, Paris, France, June 16-21, 2018 (multimedia electronic poster presentation)

van der Velden TA, **Krikken E**, Arteaga CS, Visser F, Klomp DWJ, Feasibility of high throughput scanning at 7T: 13 subjects per hour, ISMRM 26th Annual Meeting, Paris, France, June 16-21, 2018 (traditional poster presentation)

Krikken E, Khlebnikov V, Zaiss M, van der Kemp WJM, van der Velden TA, van Laarhoven HWM, Klomp DWJ, Wijnen JP, Monitoring neoadjuvante chemotherapy in breast cancer patients using CEST and ^{31}P-MRS at 7 tesla, ISMRM 25th Annual Meeting, Honolulu, Hawaii, USA, April 22-27, 2017 (multimedia electronic poster presentation)

Krikken E, van der Kemp WJM, van Laarhoven HWM, Klomp DWJ, Wijnen JP, Early detection of changes in phospholipid metabolism during neoadjuvant chemotherapy using phosphorus magnetic resonance spectroscopy at 7 tesla, ISMRM 24th Annual Meeting, Singapore, Republic of Singapore, May 7-13, 2016 (multimedia electronic poster presentation)

Krikken E, Zaiss M, Khlebnikov V, van Laarhoven HWM, Klomp DWJ, Wijnen JP, Amide CEST at 7T: A possible biomarker for response to neoadjuvant chemotherapy in breast cancer, ISMRM 24th Annual Meeting, Singapore, Republic of Singapore, May 7-13, 2016 (traditional poster presentation)

Krikken E, Zaiss M, Khlebnikov V, van der Kemp WJM, van Laarhoven HWM, Klomp DWJ, Wijnen JP, Early detection of changes in amide CEST & 31P-MRS at 7T during neoadjuvant chemotherapy in breast cancer, ISMRM Workshop on Ultra High Field MRI: Technological Advances & Clinical Applications, Heidelberg, Germany, March 6-9, 2016 (oral presentation)

Krikken E, van der Velden TA, Hayawi H, Italiaander M, van Laarhoven HWM, Raaijmakers A, Klomp DWJ, Wijnen JP, Bilateral breast coil for 7T MRI with radiative antennas, ESMRMB, Edinburgh, United Kingdom, October 1-3, 2015 (multimedia electronic poster presentation with lightning talk)

Krikken, E, Zwanenburg JM, Luijten PR, Klomp DWJ, Wijnen JP, Retrospective T_1-calculation based on DCE-MRI series with in homogeneous B1 at 7T in the breast, ISMRM Workshop on MRI in the Management of Breast Disease: Past, Present & Future, San Francisco, CA, USA, February 12-15, 2015 (traditional poster presentation)

A

Dankwoord

Na al dat schrijven ben ik dan toch eindelijk toegekomen aan het belangrijkste, namelijk het dankwoord. Want zonder vele van jullie was dit proefschrift nooit tot stand gekomen. Ik heb de afgelopen jaren mogen genieten van de expertise en het enthousiasme van de mensen waarmee ik samen mocht werken. Maar uiteraard naast het werk heb ik een fantastische groep mensen die me de nodige ontspanning bieden. Hieronder wil een paar mensen in het bijzonder bedanken.

Om te beginnen, **Jannie**, mijn co-promotor. Zonder jou was het absoluut niet gelukt. Je oneindige enthousiasme en steun hebben me telkens weer gemotiveerd. Je stond ten alle tijden klaar als ik het even niet meer wist. Je deed me elke keer weer verwonderen over de kennis en expertise die je hebt en ik heb ontzettend veel geleerd van je, heel veel dank daarvoor! Daarnaast was je ook altijd te porren voor een drankje buiten het werk of andere activiteiten. Wie kan er nu zeggen dat hij samen met z'n co-promotor heeft gesurft? Bedankt dat ik de eer mocht hebben om je eerste PhD'er te zijn en dat er maar vele mogen volgen!

Dennis, er zijn maar weinig mensen die met zoveel positivisme in het leven staan als jij, hou dat alsjeblieft vast. Jij bent degene die me van de gang heeft geplukt om me vervolgens aan een in jouw woorden 'ongelooflijk gaaf project' te koppelen. Dat was het inderdaad dus dank daarvoor. Je hebt me altijd weten uit te dagen in het verder ontwikkelen van mijn kwaliteiten waardoor ik ontzettend veel heb geleerd. Heel veel succes met het META-scan project en hopelijk worden er binnenkort ook klinische borstkanker patiënten op de 7 T gescand.

Uiteraard ook bijzonder veel dank aan mijn promotoren, **Peter** en **Maurice**. Vanaf de achtergrond heb ik van jullie altijd veel steun gehad. Bovendien zijn jullie beide verantwoordelijk voor een fantastische onderzoeksomgeving waarvan ik heb mogen genieten de afgelopen jaren.

Graag wil ik de leden van de beoordelingscommissie, **prof. dr. P.J. van Diest**, **prof. dr. E. van der Wall**, **prof. dr. H.M. Verkooijen**, **prof. dr. C.T.W. Moonen** en **prof. dr. A. Heerschap**, bedanken voor de tijd en moeite die u allen heeft genomen voor het beoordelen van mijn proefschrift.

Verder gaat er heel veel dank uit naar alle patiënten die in de afgelopen jaren onbaatzuchtig hebben deelgenomen aan onze studie. Dat deze vrouwen ondanks de

heftige tijd waarin ze zich bevonden toch bereid waren om mee te doen aan onze studie vind ik meer dan bewonderingswaardig.

Maar het includeren van al deze patiënten gaat niet vanzelf. De **mammaverpleegkundigen** en **verpleegkundig specialisten**, ontzettend bedankt voor jullie inzet voor de studie. De research poli: **Tristan**, **Floor**, **Ramona**, **Ietje**, **Selena**, **Petra**, **Eveline**, **Jeanine**, **Janine**, **Josanne**, **Maureen**, **Paula**, bedankt voor de fijne samenwerking.

Saskia, ontzettend bedankt voor alle hulp rondom de SPACE studie. Dankzij jou kwamen we altijd vlekkeloos door de monitor visites heen. Ik vind dat elke klinische studie een Saskia zou moeten hebben!

Hanneke, heel erg bedankt met het helpen van het opzetten van de studie in het AMC en je kritische blik. **Aarti**, zonder jou waren er nooit patiënten in het AMC geïncludeerd, ontzettend bedankt dat je altijd klaar stond. **Irene**, bedankt voor het helpen met scannen van patiënten in het Spinoza, het ging altijd erg soepel!

Iedereen van het **mammateam in het Diakonessenhuis**, ontzettend bedankt voor het mee doen aan onze studie. Ik heb me er altijd erg welkom gevoeld. In het bijzonder wil ik **Thijs** en **Marianne** bedanken voor jullie inzet voor de studie. En natuurlijk **Anne** en **Julia** voor het opletten tijdens de MDO's als ik niet aanwezig kon zijn. Daarnaast gaat mijn dank uit naar het **mammateam van het St. Antonius**. Dankzij jullie inzet hebben we nog een eindsprint kunnen maken met de inclusies.

Paul, bedankt voor het uitvoeren van de centrale revisies samen met mij. Het was zeer interessant en leerzaam om naast je te zitten.

Dan alle laboranten die telkens weer klaar stonden om te helpen bij het scannen, in het bijzonder **Gerrit**, **Guus**, **Niels**, **Johan**, **Erik**, **Rens**, **Nikki** en **Myrthe.**

De promovendiraad/ImagO-club: **Wieke**, **Annemarie**, **Bas**, **Ellis**, **Remco**, **Bianca** en **Boris**. Bedankt voor het samen organiseren van de ImagO-(mid)dagen en de gezellige vergaderingen!

De drijvende kracht achter het werkend houden van de 7 T, **Hans** en **Fredy**. Talloze keren hebben jullie me uit de brand geholpen, dank! Ook alle coilboys bedankt! **Mark, Ingmar**, **Dimitri**, **Aidin**, **Luca** en **Erik**. Jullie stonden altijd meteen klaar om te helpen als ik weer eens langs kwam met een kapotte spoel.

A

De mannen van Q02.4.309! **Tijl,** grote ouwehoer, aanstichter van gezelligheid, voortrekker van de bierkar richting de Basket, eentje om het af te leren, nog eentje met de jas aan, en zo kan ik nog wel even doorgaan. Dank voor je wijze uitspraken en het was een eer om een kamer met je te delen. **Bart,** rapper Steen, bedankt voor je ontzettend droge humor en de fijne samenwerking. Veel succes met de volgende triatlon, respect! **Carel,** dank voor het oneindig aanvullen van de pepernotenvaas. Ik heb het afgelopen jaar denk ik genoeg pepernoten gehad voor de komende 10 jaar. En als ik iemand de trap op of af zie rennen, zal ik altijd aan je denken.

Dan vaste prik dat ik minimaal tweemaal per dag was te vinden in het eerste kantoor van de gang om koffie te halen, samen te tafelvoetballen of na het werk bordspellen te spelen. **Tim**, coffee jesus, dankzij jou zaten we nooit zonder koffie. Fijn dat ik m'n enthousiasme voor superhelden films met je kon delen. **Arrie,** vanaf student tot en met PhD, jij hebt het allemaal samen met mij meegemaakt. Jij hebt de titel al, nu ik nog. Ik ben blij dat je nog even bent blijven hangen om dat ook nog mee te maken! **Oscar**, de rustheid zelve, wat heb ik genoten van je droge humor. **Janot**, in mijn hoofd zit je nog steeds op dat kantoor. Op een gegeven moment zag ik je vaker dan Mariëlle in een week, dat zegt genoeg denk ik. Naast het koffie drinken, tafelvoetballen en spelletjes spelen, sporten we ook nog eens veel samen. En als het niet sporten is, dan zijn het wel andere dingen zoals een weekendje weg, bier drinken of pubquizen, ontzettend veel dank daarvoor.

Over pubquizen gesproken, de Superweirdos, **Alex, Cata, Lisa, Lindenholz, Janot** en **Deji.** Bedankt voor de ontzettend gezellige avonden die we samen hebben gehad. **Alex**, Bhogtron the original, thanks for being a bro, BINTANG! **Cata,** dankzij jou weet iedereen van de 7 T wat barbecueën echt is. **Deji,** love your big smile and your dance moves! **Lindenholz**, ik ken niemand die zo fanatiek in alles is als jij en fijn dat we zo af en toe onze noordelijke roots konden delen. En dan **Lisa**, wat had ik gemoeten zonder jou. Samen met Mariëlle een gedeelde eerste plek als vrijwilligster. Altijd bereid om me te helpen, met wat dan ook. Dank voor onze vele fijne gesprekken, de lieve dierenfilmpjes, het samen sporten en de woordgraptogrammen!

Wybe, jij stond altijd klaar om me te helpen met scannen. Dank voor het delen van je kennis en je humor. **Lieke**, van student tot collega. Ik heb je mogen begeleiden tijdens je afstuderen, waarbij je een belangrijke bijdrage hebt geleverd aan het project. Het was een fijne samenwerking!

De rest van de gang, bedankt voor de leuke werkomgeving in het UMC! **Wouter**, **Martijn, Jeroen, Cyril, Peter, Anneloes, Vitaliy, Carlo, Tine, Mario, Jolanda, Seb, Ria, Edwin, Quincy, Kees, Anna, Niek, Stefano, Flavio, Jacob-Jan, Jeanine, Alexander, Alessandro, Jaco, Natalia, Mike, Kathi, Carrie, Tommy, Myrthe en Rosina**. Ook iedereen die al weg is: **Joep**, **Frank**, **Ronald**, **Wouter**, **Vincent**, **Lennart**, **Hanke**, **Anita**, **Alexandra**, **Mariska's**, **Nikki, Anja, Matthew en Jill.** En dan natuurlijk **Sylvia**, zonder jou is er geen 7 T groep!

Marten en **Thomas**, jullie kennen me het langst van iedereen en ondanks dat we elkaar niet meer zo vaak zien, voelt het altijd als thuis komen bij jullie. Dank voor jullie vriendschap.

Dan mijn lieve vrienden uit Utrecht die altijd voor me klaar staan, **Brian, Bart, Raz, Ali, Lex en Sander**. Het maakt niet uit waar we zijn, samen met jullie is het altijd lachen, gieren, brullen. Dank! En wie daar natuurlijk ook bij horen zijn mijn ontzettend knappe paranimfen **Nick** en **Thijs**. Jullie kennen me als geen ander en wat hebben we veel mee gemaakt. Wat was ik ongelooflijk trots op je Nick toen ik achter je stond als paranimf. En wat ben ik blij dat jullie straks achter mij staan, letterlijk en figuurlijk. Want dat is het, jullie staan altijd voor me klaar, voor wat dan ook en ik zal altijd klaar staan voor jullie!

En natuurlijk mijn familie, jullie betekenen veel voor mij. **Papa** en **mama**, bedankt voor het warme thuis dat jullie me bieden in het mooie Drenthe. Jullie staan altijd voor me klaar. Dank voor jullie onvoorwaardelijke liefde. **Frank,** mijn kleinere grote broer, je avontuurlijke en sportieve spirit zijn zeer aanstekelijk. Ik had geen betere broer kunnen wensen. En **Liset**, mijn kleine zusje die altijd lief voor me is, bedankt voor je nuchterheid waarmee je altijd alles kunt relativeren. Met z'n drieën kunnen we de wereld aan!

Lieve **Mariëlle**, jij maakt het leven een stukje mooier. Jij hebt er altijd voor gezorgd dat ik in een warm huis thuis kan komen. Wat ik ongelooflijk bewonderingswaardig aan je vind, is dat ik niemand anders ken die zo gedreven en gedisciplineerd in alles wat je doet. Bedankt voor al je vertrouwen, liefde en steun.

A

Curriculum vitae

Erwin Krikken was born on the 4th of July 1989 in Hardenberg, the Netherlands. He grew up in Dalerpeel with his parents John and Joke, his older brother Frank and his younger sister Liset. He completed his secondary education at the Nieuwe Veste in Coevorden. After graduation, he moved to Enschede to study Technical Medicine at the University of Twente, with a passion for the master track 'Robotics and Imaging'. During this master he fulfilled four internships at the Medisch Spectrum Twente (Cardiothoracic surgery), Radboudumc (Oral and Maxillofacial surgery), Philips Healthworks (Start-up) and UMC Utrecht (Radiology and Neurosurgery). All these internships were focused on implementing imaging techniques to optimize workflow and patient care. He completed his master's thesis at the department of Neurosurgery with close collaboration with the department of Radiology at the UMC Utrecht, where he aimed to quantify pulsations of aneurysms in the brain with 7 T MRI. After graduating in 2014, he started his PhD research at the department of Radiology at the UMC Utrecht which is presented in this thesis. In this work he showed that 7 T MRI can be used to non-invasively monitor early effects of neoadjuvant chemotherapy in breast cancer patients.

In April 2019, he started working at Sectra as a Medical Application Engineer.

A